Evaluating the mineral maturation pathways of carbonated hydroxyapatite based on pH

Universiteit Utrecht

Lucie Fiala
Utrecht University
Faculty of Geosciences
MSc Earth, Structure & Dynamics

1st Supervisor: Dr. Helen King
2nd Supervisor: Dr. Peter Kraal

September 17, 2019

1. Abstract

Bones are composed of an organic framework (70%) and calcium phosphate (30%). The calcium phosphate phase providing bone strength is hydroxyapatite. Bone growth is a complex process as many factors can encourage or inhibit this process. For instance, pyrophosphate is known to block hydroxyapatite binding sites. The aim is to study the effect of pH on hydroxyapatite formation and its precursor phases, and to see what factors inhibit or encourage the growth of this phase. Four sets of experiments were prepared using the double decomposition method with 0.1 M calcium chloride and 0.12 M sodium phosphate, one set with no additives, carbonate, pyrophosphate and citrate were made. Buffered experiments were conducted at pH 7 to 9 as pH 5 and 6 produced limited precipitate in the unbuffered preliminary run. Samples were analyzed using the Fourier-transform infrared spectroscopy and Raman spectroscopy. Overall, crystallinity increased over time. With increasing pH, the rate of hydroxyapatite growth increased, as phosphate becomes the dominant species which is needed for formation. Pyrophosphate and citrate showed no inhibition, unless in excess concentration. Carbonate was present in all samples suggesting atmospheric carbon dioxide interaction, therefore, trends observed may also be due to changing carbonate content. With increasing pH, more bands were produced with greater changes in band parameters demonstrating higher reactivity. This was seen as the unbuffered spectra produced initially more crystalline material. In a buffered setting, like the body, the body will maintain a less crystalline material by slowing recrystallization to keep this reactivity for bone remodeling

2. Acknowledgements

I would like to express my gratitude to my first supervisor, Helen King for her guidance throughout this master thesis, providing me with immense knowledge, her enthusiastic encouragement and never-ending support. I have learnt so much throughout this research and this thesis would have not been possible without her help. My sincere thanks also goes to my second supervisor, Peter Kraal for all the extremely helpful feedback and insightful comments and his positive energy during the presentation.

Finally, I would also like to thank my family and friends who have supported me throughout my entire studies.

3. Table of Contents

Introduction 5
Research Objectives 5
Background Information 6
Bone Formation 6
Nucleation and growth 7

Methodology 10
Experimental set up 10
Unbuffered experiments conducted without pH control 10
Buffered experiments conducted with titrator 10
Sample preparation 11
Unbuffered experiments conducted without pH control 12
Buffered experiments conducted with titrator 12
Experimental run 13
Unbuffered experiments conducted without pH control 13
Buffered experiments conducted with titrator 13
Spectroscopy 13
FTIR spectroscopy 13
Raman spectroscopy 14
Error margin 14

Results 15
No additive experiments 15
No pH control 15
pH-controlled experiments with a titrator 16
Carbonate experiments 19
No pH control 19
pH-controlled experiments with a titrator 19
Pyrophosphate experiments 21
No pH control 21
pH-controlled experiments with a titrator 21
Citrate experiments 23
No pH control 23
pH-controlled experiments with a titrator 23
Peak area ratios 25
Crystallinity index 28

Discussion 29
Solution conditions before precipitation at different pH levels 29
Precipitated phases 32
Chemical feedbacks and maturation pathways with no additives 34
Additive influence on the reaction pathway 37
Citrate 39
Pyrophosphate 41
Carbonate 42

Conclusions 44

References 46

Appendix A
Appendix B
Appendix C
Appendix D
Appendix E
Appendix F
Appendix G
Appendix H
Appendix I

4. Introduction

4.1 Research Objectives

Formation of a new crystal is a two-step process involving nucleation which is then subsequently followed by crystal growth. The nucleation process may be affected in three ways, (1) by the complexation of dissolved phases in solution which changes supersaturation of the solution, (2) by additional particles attaching to the surface of a newly formed crystal, allowing it to grow, (3) other particles may be incorporated into the material which also influence the solutions supersaturation and its physical properties, which affect nucleation. Critically, each of these different steps is directly controlled by the solution chemistry. Therefore, changes in ion speciation, through changes in pH, for example, will play a significant role in the mineral growth after nucleation.

Bone is one system where the chemical environment is tightly regulated to facilitate the nucleation and growth of carbonated hydroxyapatite (further referred to as CHA). One of the chemical controls is the presence of specific inorganic and organic ions. For example, Klop (2018) demonstrated that varying carbonate (CO_3^{2-}) content alters CHA nucleation and growth. However, if pH levels vary uncontrollably as they did in the Klop experiments, phases other than apatite may form. Hydroxyapatite (HA) is more stable in alkaline conditions of pH 7.4 and higher, while phases such as octacalcium phosphate (OCP), dicalcium phosphate dihydrate also known as brushite (DCPD) and dicalcium phosphate anhydrous also known as monetite (DCPA) are more stable in acidic conditions below pH 6 (Drouet, 2013). Although the Klop (2018) nucleation experiments began at pH 8.9, the precipitation of a phosphate phase quickly lowered the pH, suggesting that there is a chemical feedback between precipitation and the final phase produced. A complex chemical feedback during the experiments explains the lack of apatite synthesized and the formation of OCP in Klops' (2018) solution sample without added CO_3^{2-}, as the final solution was of pH 5.2, which is favorable for OCP precipitation (Pompe, 2015).

The main aim of this research is to study the effect of different pH levels on the formation of CHA to understand what factors inhibit and encourage the growth of this phase. For example, Brecevic and Furedi-Milhofer (1972) and Kazanci et al. (2006) showed that in the presence of high concentrations of calcium (Ca) and phosphate (PO_4), CHA formation occurred first via the growth of amorphous calcium phosphate (ACP) which transformed into OCP and finally matured into HA. Therefore, the findings of Klop (2018) may indicate that maturation at lower pH levels is prevented. Understanding the maturation pathway for the formation of apatitic phases is essential as it gives us insight into how bones acquire their biomechanical properties such as their strength and provide information on the possible changes on such properties due to external factors. For instance, the effect of bone diseases like osteoporosis on bone structure. By studying bone maturation under different pH levels, we will observe if the phases present form from different precursors or if sequences of precursor phases depend on the pH level. External factors may inhibit or encourage bone growth. Previous studies such as those by Addison et al., (2007) and Jung et al., (1972), concluded that the molecules, pyrophosphate, and citrate are known as potent inhibitors of bone growth. Both pyrophosphate and citrate were analyzed to see whether their presence in solution changes the calcium phosphate phase being produced during precipitation. A carbonated calcium phosphate solution was also tested to see what the stable phase is at different pH levels.

Four sets of samples were prepared using the double decomposition method with a 0.1 M calcium chloride ($CaCl_2$) and a 0.12 M sodium phosphate (NaH_3PO_4) solution. The first set of samples did not have any additives in solution apart from the 0.1 M $CaCl_2$ and 0.12 M NaH_3PO_4 solution. The second, third, and fourth set of samples had carbonate, pyrophosphate, and citrate added into the solution, respectively. Every set of experiments was tested at pH levels 5 through 9. The pH was kept constant

using a titrator over the duration of the experiment. A sample of 10 mL was taken each day, for three days. These samples were then analyzed using the Fourier-transform infrared spectroscopy (FTIR) to study changes in spectra as the sample matures and Raman spectroscopy for mineralogical phase identification.

4.2 Background Information

4.2.1 Bone formation

Examining bone mineralization is essential as there are many diseases, including osteogenesis imperfecta, osteoporosis, and renal osteodystrophy, that can inhibit or remarkably enhance this process (Moe et al., 2006). This impedes the role of bones as structural support, protection for vital organs, and to store critical chemical components (Viguet-Carrin et al., 2006). Also, changes in bone properties alter their ability to withstand mechanical stress and fractures. The density and strength of bones are controlled by bone shape, bone tissue type and their quality, their re-modeling rate, any microdamage, collagen structure, crystal size and mineralization (Tzaphlidou, 2008; Wopenka and Pasteris., 2005). Changes associated with disease are typically linked to changes in the local chemistry at the mineral growth site. For instance, an abnormality in the bone collagen cross-linkage and even a reduced collagen synthesis rate, results in osteogenesis imperfecta in which the bone matrix becomes weak and can fractures easily, as collagen is a critical protein in bone important for its strength (Bone health and osteoporosis; Office of the Surgeon General, 2004).

There are two types of bone: cortical and trabecular (cancellous). Cortical bone makes up 80% of the skeleton and is very dense and compact as it is mainly calcified. It makes up the hard outer layer of our bones, providing structure and strength (Hadjidakis & Androulakis, 2006). Trabecular bone makes up 20% of the skeleton and has a spongy, honeycomb-like structure, resulting in a lower density and lighter bone with a higher turn-over rate. This bone makes up the inner layer of our bones and has a metabolic function (Hadjidakis & Androulakis, 2006). Although the structure of the two types of bone is different, both are complex tissues that are primarily made of a mixture between an organic framework (70%) and inorganic mineral crystals (30%) (Sobczak et al., 2009). In particular, the most mineralized bone being cortical bone is composed of an organic structural protein, collagen (90%) and inorganic calcium phosphate crystals.

The collagen framework plays many vital roles in bone functionality and makes up 30% of bone weight (Paterson., 1988). A study by Tzaphlidou (2008) investigated how bone quality is affected if abnormal collagen is present. According to their results and from previous work by Bailey et al. (1992), the quality of collagen is significantly affected in abnormal bone. Chains of collagen twist into triple helices which then combine and bond with other helices forming ropes, also known as collagen fibrils. These fibrils are found as layers allowing to deposit crystals in between. Fibril properties such as over-hydroxylation, disorganized collagen packing and a loss of intermolecular cross-links will result in more fragile bones as the mechanical properties are reduced due to a decrease in biomechanical strength of the collagen and therefore, lowered fibril stabilization. Such collagen fibril abnormalities may be influenced by a change in protein content or their molecular orientation in the bone matrix. Research on osteoporosis showed that the structure and diameter of collagen fibrils in both cortical and trabecular bones had been primarily affected (Rosenberg et al., 2012). According to Porfírio and Fanaro (2016), the supplementation of collagen hydrolysate proved as an effective method to stimulate bone matrix collagen synthesis and increase bone density, reducing the effect of osteoporosis and osteoarthritis. This increased stability and regeneration of the tissue is due to the essential amino acids of glycine and proline in the collagen hydrolysate.

Similarly, the chemistry of bone minerals can change in response to disease. Typical bone mineral is comparable to the minerals from the apatite group in its chemistry and structure. Apatites are minerals with a hexagonal framework, a tightly packed PO_4 network with the general formula of $M_{10}(PO_4)_6X_2$ in which M is a metal (most commonly Ca) and the channel site X is generally occupied by OH^- or a halogen such as F^- or Cl^- producing HA, fluorapatite and chlorapatite respectively (Naray-Szabo S., 1930; Beevers, C. A., & McIntyre, D. B.,1946; Wopenka and Pasteris., 2005; Haldar and Tišljar, 2014). Lattice parameters such as solubility, dissolution properties, thermal stability, and brittleness in an apatite can be affected significantly with different substitutions into its crystal structure (Ben-Nissan, B., 2014). The mineral phase components of bone providing stiffness is HA (Sobczak et al., 2009). In the body CHA can be found as a type-A CHA in which CO_3^{2-} substitutes for OH^- and as a type-B CHA, where the CO_3^{2-} substitutes for PO_4^{3-} (Ślósarczyk, Paszkiewicz and Paluszkiewicz, 2005; Janssen, 2018). Type-B CHA is more common in biological systems, as it has a relatively low activation compared to type-A CHA (Peroos et al., 2006). However, bone mineral crystals formed under conditions of restricted P uptake, e.g., during hypophosphatemia, show an increase in the CO_3^{2-} content which can alter biomechanical properties of the bone by causing the apatite to be more soluble as CO_3^{2-} substitutes into the B-site and increases disorder in the crystal lattice (Macica et al., 2016). Overall, the nucleation and growth mechanisms of bone mineral crystals are related to chemistry and the collagen structure.

4.2.2 Nucleation and growth

Watt (1923) had studied three known and present theories on how bone minerals could precipitate using calcium phosphate and calcium carbonate. The first theory investigated the inorganic salts depositing within the bone matrix via in-situ precipitation from the soluble salts present in the blood and tissue. The second theory suggested that calcium phosphate and calcium carbonate are released by bone cells into or within the matrix. The final theory looks at how calcium carbono-phosphate is incorporated into the matrix from the blood due to carbon dioxide tissue content changes. Subsequently, precipitation takes place and transforms into the two individual inorganic salts; calcium phosphate and calcium carbonate in the correct ratios found in bone.

Classical precipitation theory describes the process of crystal growth and nucleation in which ions, atoms or molecules present in solution, also known as growth units, bond and re-arrange themselves in a characteristic pattern of a crystalline solid to form a nucleus (Bahrig et al.,2014). To form bone apatite, all elements (Ca, P, O, and all appropriate ions) are required in the correct amounts (Wopenka and Pasteris, 2005).

For nucleation to take place, the activation energy barrier must be overcome, and therefore a high initial supersaturation (C_{max}) is required. The thermodynamic driving force of nucleation is supersaturation (Bahrig et al.,2014), which is the difference in the chemical potential between a molecule in the solution (μs) and chemical potential in the bulk crystal (μc).

$$\Delta\mu = \mu s - \mu c$$

$\Delta\mu > 0$ means that the solution is supersaturated and thus nucleation and growth are possible. When $\Delta\mu < 0$, the solution is undersaturated and therefore, dissolution of the mineral takes place. (Cuballis and Anderson, 2010).

If the concentration of the growth species (C_s) goes below a minimum concentration for nucleation (C_{min}), the supersaturation of the solution is reduced (Fig. 1B). This results in a decreased nucleation rate as the local concentration of ions is depleted, nucleation stops and growth of the crystal takes

place by diffusion as shown in Figure 1B (Bahrig et al.,2014). Additives may incorporate into crystal growth sites, and block the possibility of growth units attaching, inhibiting the nucleation process (Dalmolen, 2005).

Once a nucleus has formed, growth units need to be incorporated and arranged into the crystal surface for the crystal to grow. The most common crystal growth theory model was created by Kossel and Stranski (1927) in which the model represents a pure ionic crystal and suggests that there are three possible attachment sites for the growth units. These three attachment sites are kinks, steps, and terraces (Fig. 1A) (Cuballis and Anderson, 2010). Depending on the site, the growth unit attaches to, the number of bonds with the crystal surface will differ. Attachment to the terrace forms one bond, to the step forms two bonds and with a kink forms three bonds producing the most stable configuration (De Yoreo and Velikov, 2003; Cuballis and Anderson, 2010; Bahrig et al., 2014).

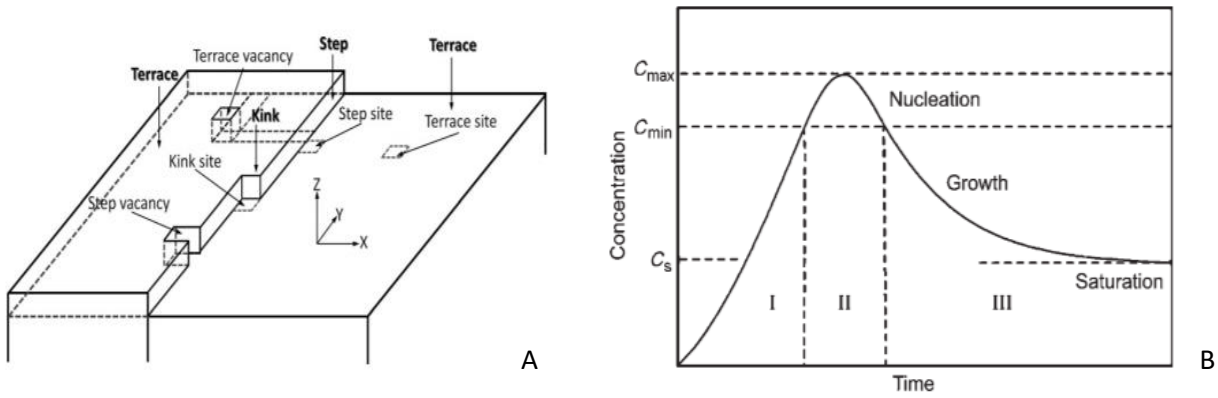

Figure 1A. Schematic diagram crystal growth theory model by Kossel and Stranski (1927) of a crystal surface and its possible attachment sites for growth unit sites taken from the paper by Cuballis and Anderson, 2010.

Figure 1B. The LaMer and Dinegar (1950) model describing nucleation and subsequent nucleus growth. Where I: generation of atoms and ions, II: nucleation period, III: crystal growth, Cs: solubility, C_{min}: minimum concentration for nucleation and C_{max}: maximum concentration for nucleation. The figure is taken from the paper by Bahrig et al., 2014.

Titov et al. (2016) conducted a research in which the mineralization process of HA synthesis in blood plasma was studied through crystallizing HA via in-vitro simulations in the blood plasma of healthy adults at pH 7.4 and 37°C. Acidic phosphates such as OCP and DCPD are often assumed to be precursor phases which then transform into the more stable HA (Titov, 2004), however the study by Titov et al. (2016) suggested that no precursor phases were present during HA synthesis in blood plasma with low concentrations of Ca and P. Instead, acidic phases precipitated during secondary transformations. HA crystals of 10-70 nm were found in the blood plasma residue using Transmission electron microscopy (TEM) data, consisting of thin plates elongated along the c-axis in a well-ordered structure often in a hexagonal habit common to the structure and morphology of bone apatite. These crystals were calcified via calcium phosphate deposition (Titov, Larionov & Shchukin, 2000; New & Aikawa, 2013).

The mineralization process may also be affected by various compounds and proteins. For instance, in order for HA crystals to precipitate in blood, serum albumin, a major blood component, must be present as it plays a significant role in biomineralization, regulating the nucleation of HA by promoting or delaying calcification under different conditions, for instance, under varying protein concentrations (Mavropoulos et al. 2011). According to Thompson and Towler (2012), 45% of circulating calcium in our bodies is free, 45% is attached to serum protein, specifically to albumin, and the final 10% of

calcium complexes with minor molecules such as phosphate and citrate. The albumin decreases the interfacial energy of the nuclei and can adsorb onto the HA crystal surface-active growth sites, preventing additional particles from attaching, therefore impeding the growth of the crystal (Titov, Larionov & Shchukin, 2000). The presence of various ions and other serum proteins, such as Fetuin-A, may inhibit the formation of apatite nuclei and instead, stabilize the formation of ACP nuclei. Fetuin-A is considered a potent mineralization inhibitor as it can preferentially bind with calcium and newly forming apatite crystals (Titov, Larionov & Shchukin, 2000; Price and Lim., 2003). A study was conducted by Price and Lim (2003) on the inhibitory effect of Fetuin-A on HA precipitation in *in-vitro* supersaturated calcium and phosphate experiments using rat blood serum. With Fetuin-A absent, a cloudy white precipitate was produced immediately when the calcium and phosphate solutions were mixed at pH 7.4. However, in the presence of the protein, the precipitation of the initial calcium phosphate mineral phase was delayed due to Fetuin-A complexing with the initial nuclei. It is resulting in inhibiting the precipitation and transformation into the stable mineral phase produced in the absence of the protein up to 20 hours. Another inhibitor of HA formation is the presence of inorganic pyrophosphate. An increase in inorganic pyrophosphate may inhibit the production of HA but not the other mineralogical phases, while a decrease will result in excess precipitation throughout the entire body (Jung et al., 1972).

The presence of different ions and their concentrations affect nucleation, type of crystals formed, crystal growth, and the crystal properties. Nucleation may be either homogeneous or heterogeneous, in which foreign particles are absent or present in the solution, respectively (Cuballis and Anderson, 2010). In bone, nucleation is thought to be dominated by heterogeneous mechanisms. Experiments have shown that mineralization of the collagen matrix takes place along the collagen fibrils (Rosenberg et al., 2012; Tzaphlidou, 2008; Kazanci et al., 2006). However, the collagen and chemical environment are also clearly regulated by the presence of specific cells; different cells are found in our bones with the function to form or resorb bone material, maintaining bone homeostasis (Rosenberg et al., 2012). Osteoblasts have the primary role in the synthesis and mineralization of the new bone matrix called the osteoid, while osteoclasts are cells found on the bone surface which digest the bone matrix by secreting enzymes that resorb the mineralized tissue (Matsuoka et al., 2014).

Despite almost 100 years of studying bone nucleation, it remains a much-disputed process. Bone formation and the nucleation of its mineralogical phases, including CHA, are not entirely understood, as this complex process is affected by many factors which can inhibit or encourage bone growth. According to a study by Addison et al., (2007) the presence of inorganic pyrophosphate inhibited the mineralization of ''soft'' tissues forming as it blocked the binding sites on the crystal surface. However, its degradation into phosphate within bones and teeth would stimulate crystal growth.

The experiments used osteoblast cultures to gain insight into pyrophosphate effect on osteoblasts during bone formation and concluded that with high concentrations of extracellular inorganic pyrophosphate present, direct synthesis and mineralization of HA is repressed by adsorbing to the attachment sites of the growing crystals. In the presence of citrate, HAP precipitates with a decrease in crystal size, more structural imperfections, and a higher content of carbonate (van der Houwen et al., 2003). Carbonate present could also influence the process as the buffering capacity is taken out of the system when it is incorporated. Therefore, extreme local changes in pH can occur in our bodies which are otherwise pH buffered.

5. Methodology

5.1 Experimental setup

Samples were prepared using the double decomposition method between a 0.1 M calcium chloride ($CaCl_2$) solution and a 0.12 M sodium phosphate (Na_3PO_4) solution which has previously been done by Klop (2018) and De Groot (2017). Four different sets of experiments were conducted at room temperature. The first set of solutions had no additives in solution. The second, third, and fourth set of experiment samples had carbonate (CO_3^{2-}), pyrophosphate ($P_2O_7^{4-}$) and citrate ($C_6H_8O_7$) added into the solution, respectively. These additives were used to see whether the phases precipitated and crystallization sequence would be affected in their presence in solution. Two sets of experiments were conducted: unbuffered without pH control and buffered with pH control (Table 1).

5.1.1 Unbuffered experiments conducted without pH control

For the unbuffered experimental run, in which pH was not controlled, an analysis was done for pH 5, 6, 7, 8 and 9, to study the changes in pH over time as the chemical reaction takes place, and any variation there could be with pH change from anatomical pH for bone formation which is 7.4. Previous work by Klop (2018) demonstrated that maturation occurred within six days; therefore, this was the length of the experiments. A summary of the experimental conditions for the unbuffered run is found in Table 1. Solutions which produced visible precipitate were then analyzed using the Fourier-transform infrared spectroscopy (FTIR) to study changes in spectra as the sample matured over time.

5.1.2 Buffered experiments conducted with titrator

The solutions that had most Ca-P precipitate formation were then re-run in the second set of tests in buffered conditions at room temperature. These were S_{carb} at pH 7 and S_{py}, S_{cit} and $S_{no\ add}$ all at pH levels of 7, 8 and 9. A pH-stat titration was set up to keep the pH constant throughout the experiment. A sample of 10 mL was taken each day, for three days instead of six as in the unbuffered experiments as after three days the chemical reaction appeared not to change very much. A summary of the experimental conditions for the buffered run is found in Table 1. The samples obtained from the buffered experiments were also analyzed using the FTIR to study changes in spectra over time and were additionally analyzed using Raman spectroscopy for mineralogical characterization, as P and OH groups produce characteristic vibrational features when synthesizing apatites due to their covalent bonding (Drouet, 2013).

Table 1: Experimental conditions for the unbuffered and buffered run summarized

Experimental conditions	**Unbuffered**	**Buffered – using a titrator**
Solute	0.12 M NaH_2PO_4	0.12 M NaH_2PO_4
Solution	0.1 M $CaCl_2$	0.1 M $CaCl_2$
Temperature	Room Temperature	Room Temperature
Set 1: $S_{no\ add}$ pH levels - No additive present	5,6,7,8,9	7,8,9
Set 2: S_{py} pH levels - $P_2O_7^{4-}$ inhibitor present	5,6,7,8,9	7,8,9
Set 3: S_{cit} pH levels - $C_6H_8O_7$ inhibitor present	5,6,7,8,9	7,8,9 Note: two sets of pH 7 tests conducted, a 5,88g and 0.001g citrate content
Set 4: S_{carb} pH levels - CO_3^{2-} present	7	7
Duration	6 days	3 days
Sample size	1 mL per hour for 5 hours a day	10 mL a day

5.2 Sample preparation

To prepare the 0.1 M $CaCl_2$ stock solution, 8.8223 g of $CaCl_2$ was dissolved in 800 mL of distilled water. Using a measuring cylinder, 250 mL of the 0.1 M $CaCl_2$ solution was poured into two bottles. In one bottle, 0.066495 g of sodium pyrophosphate ($Na_4P_2O_7$) was add to make a 0.001 M $P_2O_7^{4-}$ + 0.1 M $CaCl_2$ solution (abbreviation: S_{py}). To the second bottle, 29.4 g of sodium citrate ($Na_3C_6H_5O_7$) was added to make a 0.4 M $Na_3C_6H_5O_7$ solution (abbreviation: S_{cit}). These solutions were then divided into five bottles of 50 mL each. The remaining 300 mL of the 0.1 M $CaCl_2$ solution was divided into six bottles of 50 mL which would serve as a test with no additives (abbreviation: $S_{no\ add}$) and one carbonate experiment (abbreviation: S_{carb}).

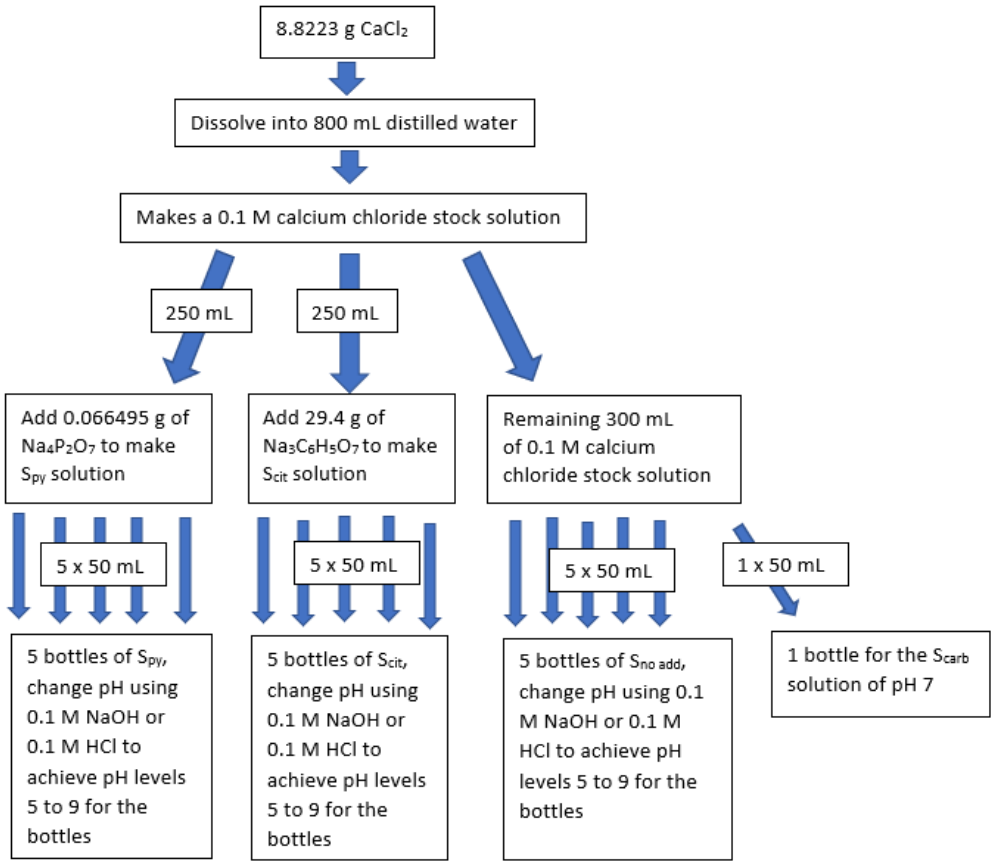

Figure 2. Sample preparation flow chart summarizing preparation of the 0.1 M calcium chloride stock solution and the 4 sets of experiments to be run: S_{py}, S_{cit}, $S_{no\ add}$ and S_{carb}

For the 0.12 M Na_3PO_4 stock solution, 13.62816 g of NaH_2PO_4 was dissolved in 800 mL of distilled water. To make the 0.24 M sodium carbonate (Na_2CO_3) stock solution (abbreviation: S_{carb}), 1 g of Na_2CO_3 was dissolved in 50 mL of the 0.12 M Na_3PO_4 solution. The remaining 750 mL was divided into 50 mL samples.

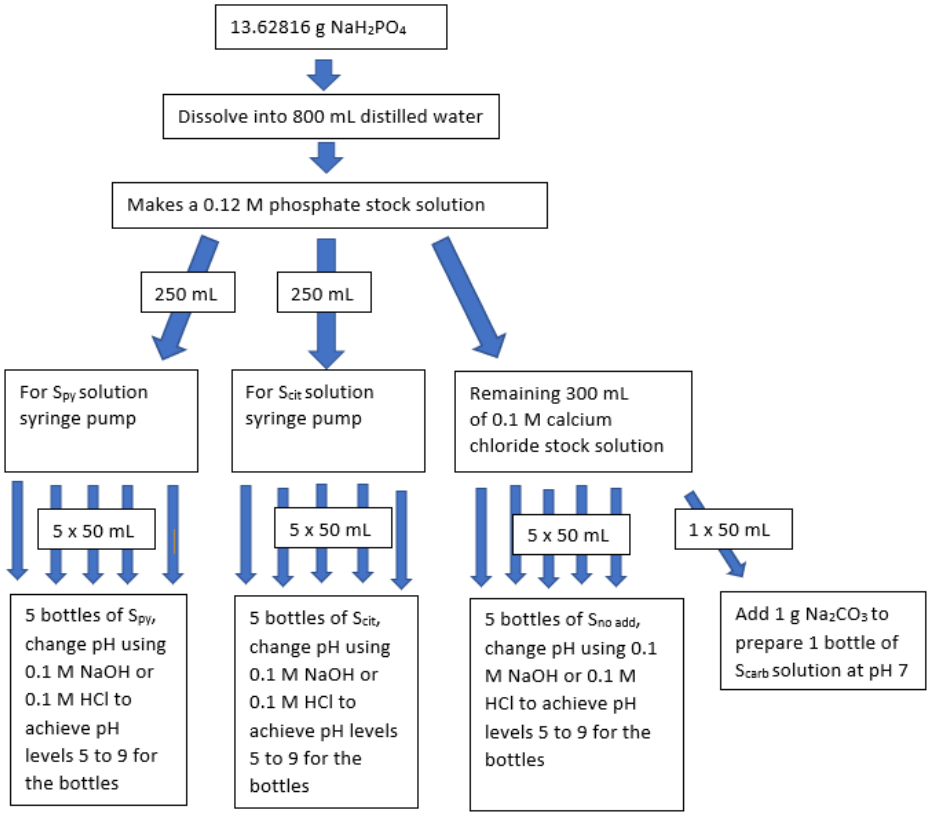

Figure 3. Sample preparation flow chart summarizing preparation of the 0.12 M phosphate stock solution and the 4 sets of experiments to be run: S_{py}, S_{cit}, $S_{no\ add}$ and S_{carb}

5.2.1 Unbuffered experiments conducted without pH control

The pH was tested of all 50 mL solutions, to get the desired initial pH level per bottle, either a 0.1 M NaOH or HCl was added manually using a titrator pipette (Figure 2). In the end, the 5 bottles of 0.001 M $P_2O_7^{4-}$ + 0.1 M $CaCl_2$ solution, the 5 bottles of 0.4 M $Na_3C_6H_5O_7$ + 0.1 M $CaCl_2$ and the 5 bottles of the 0.1 M $CaCl_2$ solution were brought to pH levels of 5,6,7,8 and 9. The 0.1 M $CaCl_2$ + 0.24 Na_2CO_3 and 0.12 M Na_3PO_4 + 0.24 Na_2CO_3 solutions had pH levels of 7.1 and 7.2 respectively, without any pH manipulation. These values are close to the approximate pH of blood serum.

5.2.2 Buffered experiments conducted with titrator

The unbuffered experiments which had produced most precipitate were prepared and re-run using the titrator set up (S_{carb} at pH 7 and S_{py}, S_{cit} and $S_{no\ add}$ all at pH levels of 7, 8 and 9). Into two separate flasks, 50 mL of the 0.1 M $CaCl_2$ solution and 50 mL of the 0.12 M Na_3PO_4 solution were set apart. Using a pipette, 0.1 M NaOH or 0.1 M HCl was added to each flask to change the pH to the desired pH level per sample (Figure 3).

5.3 Experimental Run

Samples were taken at different time points of equal intervals throughout the crystallization and maturation process that has been observed in a previous experiment (Klop, 2018).

5.3.1 Unbuffered experiments conducted without pH control

The 16 samples of 0.1 M $CaCl_2$ solution, including those with additives, were placed on the multi magnetic stirrer at 300 rotations per minute. Using tubes and syringe pumps, the 0.12 M Na_3PO_4 solutions were pumped into the respective pH $CaCl_2$ solutions at 3.00 mL/minute. The first sample was taken using a pipette at time T_0 at which the pumping of the solution began. After this, 1 mL samples were taken every hour for 5 hours for six days. The samples were stored in a freezer to prevent further reactions.

5.3.2 Buffered experiments conducted with titrator

The 736 GP Titrino was set up and used to run the pH-controlled precipitation experiments. As previously mentioned, each buffered experiment would only be run for three days as the results from the unbuffered run showed that after three days, the solution stayed quite constant. 0.1 M NaOH was connected to the titrator as the chemical reaction caused the initial pH levels to drop significantly except for the S_{carb} solution which was connected to 0.1 M HCl. The sample was stirred using a magnetic stirrer. The bottle was not sealed with additional security to reduce possible reaction with atmospheric CO_2. Using a syringe pump and tube, the 0.12 M Na_3PO_4 solution was pumped into appropriate $CaCl_2$ solution at 3.00 mL/minute. Unlike the unbuffered experiments, the samples taken were 10 mL per day for three days, to have more sample to obtain better analysis from the FTIR and have sample remaining to test in the Raman. The first 10 mL sample was taken at T_1, one hour after the syringe pump had emptied its contents and precipitate had formed. The second sample was taken on day two (approximately twenty-four hours after the first sample), and the final sample was taken on day three, about forty-eight hours after the first sample was taken. Samples were taken using a pipette and were stored in a freezer to prevent further reactions

5.4 Spectroscopy

5.4.1 FTIR spectroscopy

The type of Diffuse Reflectance Infrared Fourier Transform Spectroscopy (DRIFTS) used was the Thermo- Scientific Nicolet 6700 Fourier transform infrared (FTIR) spectrometer with 64 scans. The FTIR uses infrared light to measure wavelength absorption as most molecules absorb light within this region of the electromagnetic spectrum. This technique allows us to obtain vibrational spectra per sample studied as the bands produced in specific regions are associated with vibrations for different molecular groups. They are also used to identify the phases present and assess sample crystallinity. To reduce any background noise due to CO_2 or H_2O vapor effects, the instrument is purged with nitrogen (N) before analysis. Background data were collected for the first run using dried non-absorbent potassium bromide (KBr) to observe the amount of background noise present. The OMNIC program was then used to manipulate the collected spectral data.

The samples taken from both the unbuffered and buffered experiments were taken out of the freezer to defrost and prepare for chemical analysis. Once defrosted, the test tubes were placed into a centrifuge to separate the precipitate. Excess water was removed using a pipette and to thoroughly dry the sample, the precipitate was placed on a glass plate, and a drop of 96% Isopropanol was added to remove any remaining water by promoting evaporation. The glass plate was kept under the desktop fume hood. The dried sample was then scraped into a mortar and finely ground to < 5 µm together

with KBr and placed in a sample cup into the instrument per experiment. In between scanning and collecting sample spectra, the apparatus was flushed with N for one minute.

The spectral data collected using the FTIR was then analyzed using the FITYK program. The $v_1PO_4^{3-}$ and $v_3PO_4^{3-}$ peaks at approximately 960 and 1020 cm^{-1} were used to study the peak area ratios and to determine the crystallinity index by using the inverted full-width half maximum (further referred to as FWHM). The FWHM provides a measure of changes in band shape as it describes the width of the band at its midway point. This value can give insight into the level of crystallinity of a material. In a perfect crystal, the sites are equivalent, and therefore, the amount of energy required for each type of vibration is expected to be identical. This will appear as sharp and narrow bands in spectroscopy data. In contrast, if a crystal has low crystallinity, changing the local ordering, distances, and site shapes, the energies to initiate vibrations for specific molecular groups (e.g., P) will differ from each other. Thus, broader bands will be observed in the spectra.

5.4.2 Raman spectroscopy

Samples $S_{no\ add}$ pH 8, S_{py} pH 8 and 9, S_{cit} pH 7 with 5.88 g, pH 7 with 0.001 g and pH 8 and S_{carb} pH 7 were also analyzed using the WITec UHTS Raman spectrometer. Raman spectroscopy allowed us to study the vibrational particle mode, relative intensities, and band shifts in the system to provide an identification for the material examined, including types of chemical bonding and the degree of crystallinity. This technique uses a light scattering method as the sample is exposed to the light source. Molecules within the sample can either scatter elastically (with the same energy) or inelastically (with different energy) compared to the incident photons. The inelastic scattering of the molecules is used in Raman to obtain data. The heavier the atoms and the weaker the bonds are, the peak shift observed will be to longer wavelengths of lower energy, while atoms that have strong bonding and are lighter will show a peak shift to shorter wavelengths, thus higher energy levels. Raman spectra were also taken for the pH 8 experiments as the different calcium phosphate phases show significant spectral changes, aiding phase identification. However, Raman spectroscopy is a spot analysis method and therefore does not allow for bulk characterization of the sample.

The samples intended for analysis were taken out of the freezer, defrosted, and the test tubes were placed into a centrifuge to separate the precipitate. Excess water was removed using a pipette, and a small amount of precipitate was placed onto a glass plate to allow for evaporation. Once the sample was dry, the plate was put into the Raman spectrometer chamber with a magnifying lens of 50x. Four to five different spots were analyzed per sample to make sure all four to five measured spots produced a consistent spectrum for phase identification. To analyze the spectra collected and remove any noise, the WITEc Project Four software was used.

5.4.3 Error margin

The standard deviation for the experiments conducted is = $\pm$ 1.52 $cm^{-1,}$ and the error propagation is 0.106 cm^{-1}. As the standard deviation is low, peak shifts of 10 cm^{-1} in the spectra are considered to be significant. Calculations of the standard deviation and error propagation are found in Appendix H.

6. Results

6.1 No additives experiments

6.1.1 No pH control

During the pH drift experiments, the initial solution pH, set from pH 5 to 9, displayed a significant decrease directly upon mixing the 0.1 M $CaCl_2$ and 0.12 M Na_3PO_4 solutions (Appendix A). The initial decline was overall maintained with minor increase or decreases following the initial drop. For instance, pH 9 and 5 experiments dropped to 5.27 and 4.34 upon mixing and reached a final pH of 6.07 and 3.97 after six days. The pH 7, 8, and 9 runs produced a cloudy white precipitate immediately while the pH 5 and 6 experiments produced limited precipitate after a few hours.

FTIR analysis of the pH 7, 8, and 9 solids on day one and day six produced similar spectra in terms of band positions, but relative band intensities were observed to differ (Appendix B.1). An example of such spectra can be seen in Figure 4 below. The pH 5 and 6 experiments were not analyzed further due to limited precipitate formation. The most intense bands produced by the pH 7,8 and 9 precipitates were in the spectral region between 930 and 1400 cm^{-1}. This region is characteristic for oxyanion vibrations, including PO_4^{3-} and CO_3^{2-}; where PO_4^{3-} vibrations are found at wavenumbers up to 1100 $cm^{-1,}$ and CO_3^{2-} vibrations form weaker IR adsorption bands between 870 and 880 cm^{-1} and stronger bands between 1400 and 1530 cm^{-1} (Featherstone et al., 1984; Berzina-Cimdina and Borodajenko., 2012). The position of a broad band between 800 and 1400 cm^{-1} in the spectra indicate that PO_4^{3-} is represented more strongly compared to CO_3^{2-} in the precipitates. All spectra show four prominent and sharp bands between 930 and 1400 cm^{-1}. An adsorbed water band (hydroxyl region) related to symmetrical stretching of liquid water is present in the region above 3000 cm^{-1} for all samples. While the pH 7 and 8 spectra show bands positioned around 1358 cm^{-1}, 3265 cm^{-1}, and a characteristic doublet at 3488 cm^{-1} and 3534 cm^{-1}, the pH 9 spectra do not show distinct bands in the hydroxyl region besides the doublet close to 3500 cm^{-1}. Changes in the FWHM were measured for the PO_4^{3-} related bands between 1000 and 1400 cm^{-1}; however, no specific trends were observed across any spectrum. For example, in the pH 7 and 9 spectra, the FWHM of bands at wavenumbers up to 1000 cm^{-1} increased by an average of 15 cm^{-1} while the bands positioned above 1000 cm^{-1} show no specific trend, as various bands decreased in width while others become wider. The decrease in width in pH 7 is not very large. For instance, the peak at 1221 cm^{-1} drops from 70.24 cm^{-1} to 68.09 cm^{-1} at the end of six days. From the three experiments, pH 7 showed the highest crystallinity after six days.

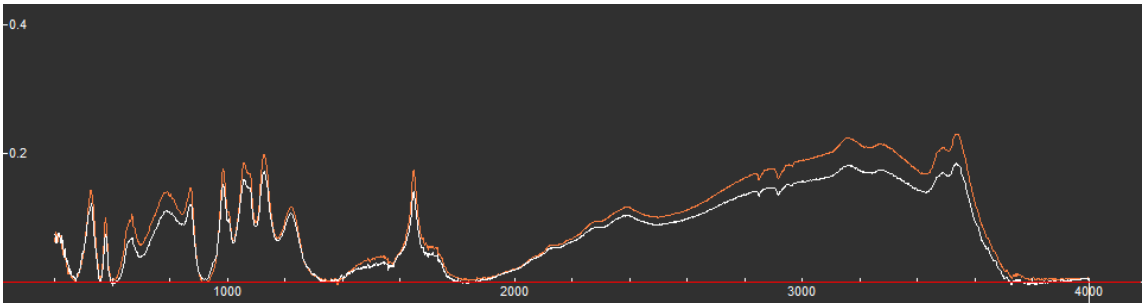

Figure 4 Unbuffered run for $S_{no\ add}$ pH 7: White – day one and Orange – day six

6.1.2 pH-controlled experiments with a titrator

Three pH levels were tested: 7, 8, and 9. Two runs were conducted at pH 8 to test for reproducibility. A white precipitate was observed to form immediately upon injection of the 0.12 M Na_3PO_4 fluid into the chamber containing the 0.1 M $CaCl_2$ solution. The pH 7 experiment produced the least precipitate and pH 9 the most, even though a similar amount of NaOH was added by the titrator (Table 2). Despite the addition of 65.46 mL of NaOH required to retain a pH of 7, the precipitate showed no visibly distinguishable change in the amount of precipitate formed.

Table 2: amount of mL of 0.1 M NaOH added to each experiment over three days of the no additive experimental run

pH	Run 1: mL added 0.1 M NaOH	Run 2: mL added 0.1 M NaOH
7	65.46	-
8	52.85	55.64
9	57.11	-

All three pH levels produced FTIR spectra displaying that the precipitate has similar chemistry and structure to that observed in the unbuffered experiments as the bands are found in the same positions with a similar shape (Appendix B.1). Band positions for the pH 7 experiment are listed in Table 3 along with assigned peak types based on previous studies as an example. Only the positions and assignments for bands produced by day one precipitates are shown in the table, as bands obtained from day two and three precipitates were very similar, and the data can be found in Appendix C.

Similar to the unbuffered experiments, the pH 7,8 and 9 precipitates produced the most intense bands in the spectral region between 850 – 1600 cm^{-1} producing overall apatitic phases (Appendix B and C). As observed in the experiments without pH moderation, the relative intensities of the bands changed with increasing time. For example, all three tests showed a shoulder band at 960 cm^{-1} attributed to v_1 stretching PO_4^{3-} (Rehman and Bonfield, 1997; Drouet, 2013; Boudia, 2018; Mroz et al., 2010) which is weakly visible on day one, but becomes increasingly intense and sharper from day two onward. A similar trend was observed with the 1036 cm^{-1} band, part of a doublet associated with the v_3 stretching of PO_4^{3-}, which showed increasing definition over time (Rehman and Bonfield, 1997; Sauer and Wuthier, 2988; Mroz et al., 2010). The doublet present in the pH 9 run at 1028 and 1119 cm^{-1} on day one become more dominant and shift to the left by 12 cm^{-1} by day three. With increasing pH, the bands produced are more developed as the bands become more separated and clear shoulder peaks evolve.

In addition to PO_4^{3-}, bands related to CO_3^{2-} were found between 1420 and 1643 cm^{-1} (Drouet, 2013; Featherstone et al., 1984; Berzina-Cimdina and Borodajenko., 2012). The doublet associated with CO_3^{2-} showed a better differentiation of the bands in day two and three pH 7 samples as well as a minor shift to lower wavenumbers by 10 and 29 cm^{-1}, respectively. The pH 8 and 9 precipitates showed stronger CO_3^{2-} related bands at these positions compared to pH 7. No CO_3^{2-} was added to the solutions; hence, we expect that the CO_3^{2-} present originates from the interaction of atmospheric CO_2 with the solutions. The band intensities in the hydroxyl region and the band at 1635 cm^{-1} both decrease in height over three days, suggesting water is being removed from the material and that the 1635 cm^{-1} band most likely represents v_2 water molecule bending mode (Maréchal, 2011).

The buffered experiments produce overall broader bands at each time step in comparison to the unbuffered experiments. The shifting apatitic band in the pH 7 spectra between 1020 and 1036 cm^{-1} shows decreasing FWHM from 94.1 cm^{-1} on day one to 72 cm^{-1} by day three. The same trend is observed in the pH 8 and 9 spectra for the same bands. The v_1 PO_4^{3-} shoulder band at 950 cm^{-1} decreases in its FWHM over the days as well and is most defined by day three in the pH 9 spectra

compared to the pH 7 and 8 spectra. The carbonate-related bands decrease in FWHM over time. In the pH 8 spectra, the band at 1428 cm^{-1} has a value of 45.13 cm^{-1} on day one dropping to 37.09 cm^{-1} by day three. Overall the band FWHM of pH 8 precipitates were narrower than those observed at pH 7 but broader than those from precipitates formed in the experiments initiated, but not maintained, at pH 8. Although the main bands showed decreased FWHM over time, some bands, such as the v_1 PO_4^{3-} band at 1106 cm^{-1} increased in FWHM in the pH 7 and 9 spectra, from 115.4 cm^{-1} and 75.42 cm^{-1} on day one to 117.8 cm^{-1} and 108.08 cm^{-1} by day three, respectively.

Table 3: Peak types assigned to FTIR peak positions (cm^{-1}) where PO_4^{3-} = Phosphate, CO_3^{2-} =carbonate, CA = carbonated apatite, HA = hydroxyapatite and OH = hydroxide. Types based on finds from studies by (1) Rehman and Bonfield, 1997; (2) Drouet, 2013; (3) Martinez-Huitle et al, 2013; (4) Boudia, 2018; (5) Sauer and Wuthier,1988; (6) Mroz et al., 2010 (7) Maréchal (2011)

S no add– pH 7			
Day 1	**Day 2**	**Day 3**	**Peak type**
467	471	467	$V_2PO_4^{3-}$ (1)
558	553	562	$V_4PO_4^{3-}$ CA + HA/OCP (1,6)
601	603	601	$V_4PO_4^{3-}$ O-P-O bending HA (1,2,4,6); H_2O molecule (7)
896	871	880	HPO_4^{2-} mode (2)
959	960	960	$V_1PO_4^{3-}$ P-O stretching CA + OCP (1,2,4,6)
1036	1028	1020	$V_3PO_4^{3-}$ OCP (1,5,6)
1106	1104	1102	$V_3PO_4^{3-}$ HA (1,5)
-	1214	1218	HPO_4^{2-} in plane bending (4)
1284	1296	1305	
1422	1412	1412	V_3CO_3 OCP (2,6)
1495	1466	1466	V_3CO_3 CA + OCP (2,6)
-	1548	1532	V_3CO_3 (2)
1635	1635	1647	V_3CO_3 CA + HA (2); v_2H_2O bending mode (7)
1994	1990	1977	
2460	2427	2456	
>2600	>2600	>2600	OH- stretching (1,2,3,7)

Raman spectroscopy of different points on the precipitate showed similar results as the FTIR analysis. Band positions for the three consecutive days and their assigned peak type using literature and data from previous studies are recorded in tables in Appendix E. The Raman spectra showed dominant bands between 400 and 1200 cm^{-1} with similar band positioning over three days (Appendix E.1). The bands formed are attributable to PO_4^{3-} groups, as seen in the example Table 4. The dominant band at 963 cm^{-1} is attributed to a strong v_1 symmetrical stretch of PO_4^{3-} (Litasov, 2017; Li et al., 2016; Falcke et al., 1990; Frost et al., 1990) and becomes narrower by day three compared to days one and two which remain identical. Raman spectroscopy confirms the presence of CO_3^{2-} at pH 8 as a v_3 CO_3^{2-} band at 1662 cm^{-1} develops over the three days and shifts to lower wavenumbers by 24 cm^{-1} (Li et al., 2016). The shifting band between 1069 and 1078 cm^{-1} could be a v_1 symmetrical stretch of CO_3^{2-} which may be overshadowed by the stronger PO_4^{3-} v_3 asymmetrical stretch band (Litasov, 2017; Frost et al., 2013; Penel et al., 1998). A broad band is visible at 2923 cm^{-1} on day one, but, is absent in the other two spectra.

Table 4: Peak types assigned to Raman peak positions (cm^{-1}) where PO_4^{3-} = Phosphate, CO_3^{2-} =carbonate and OH = hydroxide. Types based on finds from studies by (1) Litasov, 2017; (2) Li et al, 2016; (3) Falcke et al, 1990; (4) Frost et al, 2013; (5) Crane, 2016; (6) Penel et al., 1998

S no add– pH 8			
Day 1	**Day 2**	**Day 3**	**Peak type**
429	429	429	$V_2PO_4^{3-}$ bending (1,4,6)
447	453	-	$V_2PO_4^{3-}$ bending (1,4)
586	586	595	$V_4PO_4^{3-}$ bending (1,4,6)
613	613	-	$V_4PO_4^{3-}$ bending (1,4)
963	963	963	$V_1PO_4^{3-}$ strong symmetrical stretch (1,2,3,4)
1001	-	-	$V_3PO_4^{3-}$ asymmetrical stretch (1)
-	1043	1048	$V_3PO_4^{3-}$ asymmetrical stretch (1,4)
1069	1078	1075	$V_3PO_4^{3-}$ asymmetrical stretch (1,4); $v_3CO_3^{2-}$ symmetrical stretch (6)
1442	-	-	$V_3CO_3^{2-}$ (2)
1662	1653	1638	$V_3CO_3^{2-}$ CA + HA (2)
2855	-	-	
2923	-	-	
-	-	3255	OH stretching (4)
3445	3445	3412	

6.2 Carbonate experiments

6.2.1 No pH control

One experiment was conducted for the carbonate sample with initial solution pH 7. The solution increased to 7.07 directly upon mixing the 0.1 M CaCl and 0.12 M Na_3PO_4 solution. Overall, the initial increase continued, reaching a final pH of 8.23 after six days with minor fluctuations (Appendix A).

The FTIR analysis showed the same type of precipitate forming, as observed in $S_{no\ add}$ (Appendix B.4). However, the bands were broader for precipitates produced in the presence of CO_3^{2-}. As seen without additives, the precipitates appeared to mature with time. This is expressed as a clear shoulder peak at 958 cm^{-1} forming by day six. Similarly, the doublet associated with CO_3^{2-} was found at 1424 and 1486 cm^{-1} on day one but, shifted to lower wavenumbers and became more defined by day six, by which the 1424 cm^{-1} band became the dominant peak. The single band at 1643 cm^{-1} on day one transformed into a doublet with bands at 1627 and 1668 cm^{-1} by day six. In addition, a band at 1924 cm^{-1} was observed on day six, which was absent on day one. A broad band and a small sharp peak appeared at 2500 and 2972 cm^{-1} respectively in the hydroxyl region, which were also absent on day one. Changes in the distinctiveness of the bands were correlated with a difference in the band FWHM. For instance, the 1062 cm^{-1} band has an initial FWHM of 126.79 cm^{-1} but significantly decreased to 51.75 cm^{-1} by day six. Similarly, as for the $S_{no\ add}$ experiment spectra, the 1413 cm^{-1} band showed an increase over the experiment from 100.46 cm^{-1} to 130.83 cm^{-1}. The band at 1648 cm^{-1} had a significant reduction in FWHM from 110.92 cm^{-1} to 33.20 cm^{-1} by day six, with a difference of 77.72 cm^{-1}.

6.2.2 pH-controlled experiments with a titrator

As pH was observed to increase in the presence of CO_3^{2-} as an additive, the S_{carb} experiments were buffered using a 0.1 M HCl solution. However, during an initial experiment, it was observed that the pH dropped after precipitation had begun, unlike the unbuffered run. Therefore, 0.1 M NaOH had to be added manually to keep the pH constant at the beginning of the experiment. Once more precipitate formed, the system appeared to stabilize, and further reaction caused a pH shift to more alkaline solutions. This experiment was duplicated to ascertain the reproducibility of this pH change, added mL of NaOH and HCl are seen in Table 5. Both experiments produced cloudy white precipitates.

Table 5: mL of 0.1 M NaOH added to each experiment over three days of the carbonate experimental run

pH	**Run 1**		**Run 2**	
	mL added 0.1 M NaOH	**mL added 0.1 M HCl**	**mL added 0.1 M NaOH**	**mL added 0.1 M HCl**
7	18	91.6715	15	101.8112

The bands present on all three days show the same FTIR band positions with different relative intensities, as observed in $S_{no\ add}$ and the S_{carb} unbuffered run (Appendix C.1 and C.2). Day two and three spectra are more alike compared to day one, as more bands develop and doublets form from day two onwards. The 875cm^{-1} band on day one became two distinct bands in the following days at 863 and 903 cm^{-1}. This is attributed to B-type v_2 CO_3^{2-} out of plane bending mode as this band intensifies compared to $S_{no\ add}$, confirming the band is CO_3^{2-} as more CO_3^{2-} has been added to the solutions compared to previous experiments (Mroz et al., 2010; Rehman and Bonfield, 1997). The CO_3^{2-} present in the system is characterized by the v_3 CO_3^{2-} and v_2 CO_3^{2-} bands forming a doublet at 1416cm^{-1} and 1482cm^{-1} (Appendix B.4) (Rehman and Bonfield, 1997; Drouet, 2013) showing an increasingly dominant right band on day two onwards. The left band in the broad doublet between 1000 and 1200cm^{-1} became increasingly more dominant as the reaction proceeded. As in the $S_{no\ add}$, this band is associated with v_3 asymmetric stretching of PO_4^{3-} (Rehman and Bonfield, 1997; Boudia, 2018). A minor band present on day one at 1569cm^{-1} is absent from day two onwards while the band

at 1288 cm^{-1} only appears as of day two. The hydroxyl region increases in height, unlike in the $S_{no\ add}$ spectra, and the 1631 cm^{-1} water band follows this trend. The vibrational spectra band width changes are similar to those in $S_{no\ add}$. The 1024 cm^{-1} band shows decreasing FWHM from 99.93 cm^{-1} to 78.76 cm^{-1} by day three. The shoulder bands at 875 and 958 cm^{-1} become sharper, and their FWHM of 90.80 cm^{-1} and 33.47 cm^{-1} respectively on day one drop to 74.05 cm^{-1} and 26.68 cm^{-1}. All other bands present show a reduction in FWHM by day three, except the 1119 cm^{-1} band, which increases from 78.30 cm^{-1} to 81.86 cm^{-1}.

The S_{carb} precipitate Raman spectra confirm the trends observed in the FTIR analysis. The largest changes occurred between day one and two (Appendix E.2). After day two, the spectra remain very similar. On day one the 583 cm^{-1} band becomes a doublet at 583 and 613 cm^{-1} while the developing doublet at 429 and 450 cm^{-1} becomes more defined. Overall, bands shifting in their wavelength appear to all shift to higher wavenumbers, for instance, the shoulder peaks on day one at 998, 1026 and 1072 cm^{-1} shift by 14, 25 and 7 cm^{-1} respectively. A characteristic band present at 2935 cm^{-1} for all three days in the hydroxyl region. The S_{carb} and $S_{no\ add}$ Raman spectra are very similar (Appendix E.1 and E.2) confirming CO_3^{2-} presence in the $S_{no\ add}$ precipitates. The S_{carb} pH 7 day two spectra had a lower intensity of the 1072 cm^{-1} CO_3^{2-} band with a concomitant increase in the intensity of the PO_4^{3-} 1026 cm^{-1} band. The PO_4^{3-} band is narrower compared to day one. As the sample matured, a decrease in the 1078 cm^{-1} CO_3^{2-} band was observed, the drop was smaller than in the $S_{no\ add}$ pH 8 spectra, which would be expected from the higher CO_3^{2-} concentration in these experiments, thus, vibrational spectroscopy data confirms that the precipitates produced had a higher CO_3^{2-} content than those in the $S_{no\ add}$.

6.3 Pyrophosphate experiments

6.3.1 No pH control

The pH 7, 8 and 9 experiments with pyrophosphate added to solution produced a cloudy white precipitate immediately while the pH 5 and 6 experiments produced very little precipitate after a few hours, similarly as the $S_{no\ add}$ run. Initial pH levels 5 to 9 displayed a significant decrease upon mixing the 0.1 M CaCl solution and 0.12 M Na_3PO_4 solution (Appendix A). The initial decline was overall maintained with minor increase or decreases following the initial drop. For instance, the pH 7 and 9 experiments directly dropped to 5.16 and 5.42, respectively, reaching 4.8 for pH 7 and 6.45 for pH 9 after six days.

FTIR analysis was conducted on solutions pH 7, 8, and 9, as pH 5 and 6 produced a limited precipitate. Comparing the pH 7,8 and 9 FTIR spectra, all appear very similar to one another; therefore, no effect of pH was observed (Appendix B.2). As in $S_{no\ add}$, the pH 7 run shows little change in band position, but the increased definition of specific bands within the spectra between day one and day six. For example, in pH 7, day one there is a broad band between 2000 and 2539 cm^{-1} in the hydroxyl region. By day six, three bands at 2118, 2275 and 2385 cm^{-1} are observed in this region. These defined bands are also present in the pH 8 and 9 spectra but already present as of day one. A sharp band present around 721 cm^{-1} would be attributed to $P_2O_4^{3-}$ and would indicate calcium pyrophosphate presence (Salimi and Javadpour., 2012; Gras et al., 2013). However, this band was absent in all spectra produced in the unbuffered run, and the closest band present was at 785 cm^{-1}.

Similar to $S_{no\ add}$ and S_{carb}, the v_3 PO_4^{3-} band observed at 1062 cm^{-1} shows a decreasing FWHM over three days for pH 7 and 8, with 49.61 cm^{-1} and 39.98 cm^{-1} on day one, respectively, dropping to 46.71 cm^{-1} and 39.93 cm^{-1} by day six. The pH 9 experiment showed a FWHM increase of this band, from 42.09 cm^{-1} on day one to 47.46 cm^{-1} by day six. Comparing FWHM changes for the three pH levels, pH 7 and 8 spectra showed decreasing band width after six days for the majority of the bands while pH 9 spectra showed the opposite. For example, the band at 1220 cm^{-1} had a FWHM of 72.07 cm^{-1} and 69.70 cm^{-1} on day one for pH 7 and 8 respectively. These decreased to 69.90 cm^{-1} and 26.24 cm^{-1} by day six, while in the pH 9 experiment the band at the same position had a FWHM of 70.14 cm^{-1} on day one and increased to 75.63 cm^{-1} by day six.

6.3.2 pH-controlled experiments with a titrator

All three pH experiments produced cloudy white precipitate immediately upon addition of the 0.12 M Na_3PO_4 solution and was present over the three days. Two runs were conducted for S_{py} at pH 8 and 9 for reproducibility.

Table 6: mL of 0.1 M NaOH added to each experiment over three days of the pyrophosphate experimental run

pH	Run 1: mL added 0.1 M NaOH	Run 2: mL added 0.1 M NaOH
7	35.52	
8	31.70	51.33
9	32.61	37.36

The FTIR spectra are similar over the three days for each pH with minor variation in relative intensities, and the bands became more defined as the sample matures (Appendix B.2). In pH 7, the v1 symmetrical stretch of PO_4^{3-} at 954 cm^{-1} becomes more defined in the band envelope related to the v3 PO_4^{3-} band on days two and three. Besides, the v3 PO_4^{3-} band at 1032 cm^{-1} becomes more dominant throughout the experiment. The same is seen in the pH 8 and 9 spectra, in which, maturation of the

precipitate with time produced a better definition of the shoulder peak at 962 cm^{-1} while the 1024 cm^{-1} band becomes progressively more dominant.

The presence of pyrophosphate in the initial solution did not affect the ability of the system to uptake CO_2 as evidence for CO_3^{2-} was found as a doublet at 1428 and 1490 cm^{-1} consistent with v3 CO_3^{2-} stretching (Drouet, 2013; Mroz et al., 2010). These bands showed a shift in their position by 20 cm^{-1} to lower wavenumbers as well as an increase in their definition from day two onwards in pH 7 spectra. The pH 8 spectra show CO_3^{2-} bands observed to have slightly different positions, 1416 and 1474 cm^{-1}. In pH 9, these bands are most defined compared to pH 7 and 8 and show a shift to the lower wavenumbers by 16 and 38 cm^{-1} respectively with time. No sharp and intense band was observed in the spectra at approximately 721 cm^{-1} which would be attributed to $P_2O_4^{3-}$ and would indicate the presence of calcium pyrophosphate in any of the experiments (Salimi and Javadpour., 2012; Gras et al., 2013) and unlike in the unbuffered spectra, no band is present in the 700 to 800 cm^{-1} range, therefore pyrophosphate was not detected. Between the pH 7, 8 and 9 spectra, there is a loss of the v_3 PO_4^{3-} band between 1000 and 1200 cm^{-1} by day three. In the pH 7 spectra, this band evolves over the three days and remains visible throughout the experiment, increasing in its intensity while in the pH 8 spectra, the bands do not develop as clearly but continue to increase in intensity. Finally, the pH 9 spectra show the decreasing intensity and poor development of the v_3 PO_4^{3-} band.

Increased definition of the FTIR bands corresponded to a decrease in their FWHM. For example, in pH 7, the band at 1032 cm^{-1} decreased from 83.58 to 77.10 cm^{-1} by day three. This same band decreases from 88.78 cm^{-1} to 65.81 cm^{-1} by day three in the pH 8 spectra, which also follows the trend observed in the $S_{no\ add}$ and S_{carb} experiments. Both shoulder bands located at 892 and 954 cm^{-1} in the pH 7 spectra become narrower by day three with a decrease in their FWHM from 85.77 cm^{-1} and 34.59 cm^{-1} on day one to 79.69 cm^{-1} and 23.47 cm^{-1} by day three respectively. Unlike the pH 7 experiment, the shoulder band at 896 cm^{-1} becomes wider for pH 8, from 97.49 cm^{-1} on day one to 153.34 cm^{-1} by day three.

The pH 8 and 9 precipitates Raman spectra, confirm the findings of the FTIR analysis (Appendix D.2 and D.3). The S_{py} pH 8 and 9 spectra are similar, with minor differences in the relative intensity of the peaks for all three days. Both spectra show the PO_4^{3-} peak at 957 cm^{-1} shifting to higher wavenumbers upon maturation, while the v_3 PO_4^{3-} peak at 1075 cm^{-1} shifts to the left (Appendix E.3). The v_4 PO_4^{3-} band at 577 cm^{-1} becomes more developed and shifts by 6 cm^{-1} to higher wavenumbers from day two onwards in the pH 8 spectra. In pH 9, the band at 592 cm^{-1} on day one, develops into a doublet with the second peak at 613 cm^{-1} on day two onward. In addition, the v_1 PO_4^{3-} band at 957 cm^{-1} also shows a shift to 963 cm^{-1} by day two and becomes narrower with each day, confirming the decrease in FWHM seen in the FTIR data (Appendix B.2). There is less evident CO_3^{2-} presence observed than in the FTIR data, likely due to the overlap of the most Raman active bands with those of PO_4^{3-}. However, a small contribution from the CO_3^{2-} symmetrical stretch apatite can be seen at 1078 cm^{-1} in the spectra (Crane, 2016).

6.4 Citrate experiments

6.4.1 No pH control

The unbuffered experiments used 5.88 g of citrate for all samples. Initial pH was set in the range of pH 5 to 9. All experiments produced a white precipitate, with pH 5 producing the least and pH 9 the most. In comparison with the S_{carb}, $S_{no\ add,}$ and S_{py} runs, precipitate did not form immediately. Once produced, the precipitate remained for a few minutes before re-dissolving. The pH 5 and 6 runs showed pH increase during the experiment to 5.32 and 6.28 after six days, respectively while experiments initiated at pH 7,8 and 9 decreased in pH immediately upon injecting the 0.12 M Na_3PO_4 solution reaching 6.88, 7.92 and 7.74 after six days (Appendix A).

Only pH 7,8 and 9 were analyzed with the FTIR as pH 5 and 6 produced limited precipitate. The FTIR spectra produced many sharp bands between 500 and 1800 cm^{-1} and are visibly different in band position compared to S_{carb}, $S_{no\ add,}$ and S_{py} spectra which produced the main banding between 800 and 1200 cm^{-1} and only have two to four bands present between 1400 and 1800 cm^{-1}(Appendix B.3). Citrate spectra band positions for all pH show little change over six days; however, bands become more defined. For example, in the hydroxyl region, the bands located at 2972 and 2981 cm^{-1} in the pH 7 spectra evolve into more dominant bands in the pH 8 spectra. The FWHM trend changes are similar for the pH 7 and 8 spectra while those in the pH 9 spectra are often the opposite. For instance, the calcium citrate asymmetrical vibration band at 1595 cm^{-1} band shows increasing FWHM from 59.86 and 67.88 cm^{-1} day one for the pH 7 and 8 spectra respectively to 75.59 cm^{-1} and 79.86 cm^{-1} after six days. The same band for pH 9 shows a decrease from 47.46 cm^{-1} on day one to 42.09 cm^{-1} after six days. Similar as to the S_{py} spectra, the pH 7 and 8 spectra showed an overall decrease in band width for the majority of the bands over six days while pH 9 showed the opposite.

6.4.2 pH-controlled experiments in the titrator

Two sets of experiments were conducted for pH 7, one with 5.88 g citrate and the other with 0.001 g citrate in solution. The pH 8 and 9 samples used 5.88 g citrate. Unlike the $S_{no\ add}$, S_{carb} and S_{py} which produced white precipitate upon addition of the 0.12 M Na_3PO_4 solution, all 5.88 g S_{cit} samples produced precipitate after a few minutes, and remained for a short moment before re-dissolving, leaving limited precipitate present for the remainder of the experiment. The 0.001 g pH 7 S_{cit} experiment produced white precipitate immediately, similar to the previous tests and remained over the three days.

Table 7: mL of 0.1 M NaOH added to each experiment over three days of the citrate experimental run

pH	Run 1: mL added 0.1 M NaOH
7	30.75
7 – 0.001 g	24.56
8	28.69
9	57.68

All spectra produced appear different from the spectrum of pure citrate and are therefore related to the structure of the material and not the citrate content (Appendix B.6). For instance, the 2247cm^{-1} band is absent in the pH 8 spectrum and is therefore characteristic to pure citrate. The FTIR spectra produced by the 5.88 g and 0.001 g citrate samples were distinctly different from each other.

The samples with 5.88 g citrate produced spectra with many more bands. For the pH 7 spectra, the day one spectrum is similar to the previous experiments, appearing more apatitic, including a $v_3\ PO_4^{3-}$

band at 1020cm^{-1} (Rehman and Bonfield, 1997; Boudia, 2018). Day two and three spectra show a significant change in band shape and position shifts, appearing more citric (Appendix B.3.2). For instance, the 1581 cm^{-1} band develops into two bands at 1540 and 1565 and is attributed to a calcium citrate asymmetrical vibration of the COO^- (Martinez-Huitle et al., 2013), the v_4 PO_4^{3-} vibration doublet band at 551 and 559 cm^{-1} becomes a single band at position 586 cm^{-1} and the PO_4^{3-} shoulder band at 956 cm^{-1} shifts to 962 cm^{-1} by day two. The pH 8 and 9 spectra show most significant change between the three days, is the development of the v_3 PO_4^{3-} band between 1000 and 1200 cm^{-1} (Rehman and Bonfield, 1997; Boudia, 2018; Mroz et al., 2010). The v_3 PO_4^{3-} band appears as a gentle and more dominantly right-sided band on day one at 1078 cm^{-1} and evolves into a clear doublet on day two onwards with the more dominant band at 1036 cm^{-1}. The hydroxyl region shows bands at positions 2914, 2939 and 2972cm^{-1} on days two and three in the Ph 7 spectra.

The 0.001g citrate FTIR spectra showed less signal, which could be due to a lower material input (Appendix B.3.1). Unlike the 5.88 g S_{cit} spectra, the 0.001 g S_{cit} spectra have fewer bands present and are to the those of the S_{py}, $S_{no\ add}$ and S_{carb} samples appearing more apatitic. The band positions do not change, only their relative intensities. For example, the v_3 PO_4^{3-} band observed at 1024 cm^{-1} continues to become more dominant over the days. T

The FWHM of the PO_4^{3-} bands decreased for S_{cit} pH 7 (0.001 g), 8 and 9 experiments with time, and increase overall for the pH 7 (5.88 g) experiment. For example, the v_3 PO_4^{3-} band at 1078 cm^{-1} in pH 8 becomes narrower from a FWHM of 98.48 cm^{-1} on day one to 62.63 cm^{-1}by day three. The PO_4^{3-} shoulder bands at 892 and 941 cm^{-1} also show a decrease in width from 30.10 cm^{-1} and 26.54 cm^{-1} to 19.62 cm^{-1} and 24.66 cm^{-1} respectively. Comparing the calcium citrate band at 1412 cm^{-1} (Martinez-Huitle et al., 2013) in the two pH 7 experiments, the increase in FWHM for the 5.88 g sample is from 39.34 on day one to 54.05 cm^{-1} becoming wider by day three while the same band shows a decrease in FWHM from 78.54 cm^{-1} to 54.83 cm^{-1} by day three in the 0.001 g sample.

Raman spectroscopy analysis of different points in the pH 8 precipitate showed similar results as the FTIR analysis. The day one spectrum appears more apatitic while day two and three spectra produced citrate crystals (Appendix E.4). Many wide bands are produced and remain so over the three-day experiment. The day two spectrum shows bands evolving, produce multiple bands which are otherwise seen as a single band in the day one spectrum. For instance, the v_1 PO_4^{3-} band at 903 cm^{-1} and the v_3 PO_4^{3-} band at 1086 cm^{-1} present on all three days, develop into doublets on day two with a second band at 921 cm^{-1} for the v_1 $PO_4^{3-}$and band positions at 1065 and 1079 cm^{-1} for the v_3 PO_4^{3-}. The hydroxyl region has a characteristic band at 2936 cm^{-1} present on days one and three. The day two spectra also produce this band; however, the band has multiple bands with positions at 2926, 2947, 2968 and 2989 cm^{-1}.

6.5 Peak area ratios

Peak area ratios were calculated for $v_1PO_4^{3-}$ PO_4^{3-} and plotted into Figure 5 below. The ratios were then compared to the v_3CO_3/v_2H_2O ratios in Figure 6 to see if there were any trends visible over the three days and with varying pH levels on the maturation and development of the system.

No trend is visible between all of the experiments conducted, in Figure 5. S_{cit} pH 7 – 0.001g and S_{cit} pH 9 (Figure 5C) show an initial increase to day two in $v_1PO_4^{3-}$ / $v_3PO_4^{3-}$ followed by a drop on day three, resulting in a more dominant $v_3PO_4^{3-}$ by day three. The majority of the experiments show a decrease in $v_1PO_4^{3-}$ / $v_3PO_4^{3-}$ over the days with the exception of $S_{no\ add}$ pH 9, S_{cit} pH 7 and S_{py} pH 9, increasing the amount of $v_1PO_4^{3-}$ in the system compared to $v_3PO_4^{3-}$. In Figure 5A, the changes are linear, and the day one data points show a varied $v_1PO_4^{3-}$ / $v_3PO_4^{3-}$. Thus, the precipitate that had formed at the beginning of the experiment was different in composition compared to one another. By day two, this difference is smaller, and the pH 8 and 9 samples become more similar. The end $v_1PO_4^{3-}$ / $v_3PO_4^{3-}$ of pH 7 and 9 are almost identical while pH 8 shows deviation. In Figure 2D, the day one plotted points are clustered close together, suggesting a very similar first precipitate formed for all pH levels with a similar $v_1PO_4^{3-}$ / $v_3PO_4^{3-}$. By day three, the points deviate more as the reaction continues to take place, with increasing pH there is a higher reactivity.

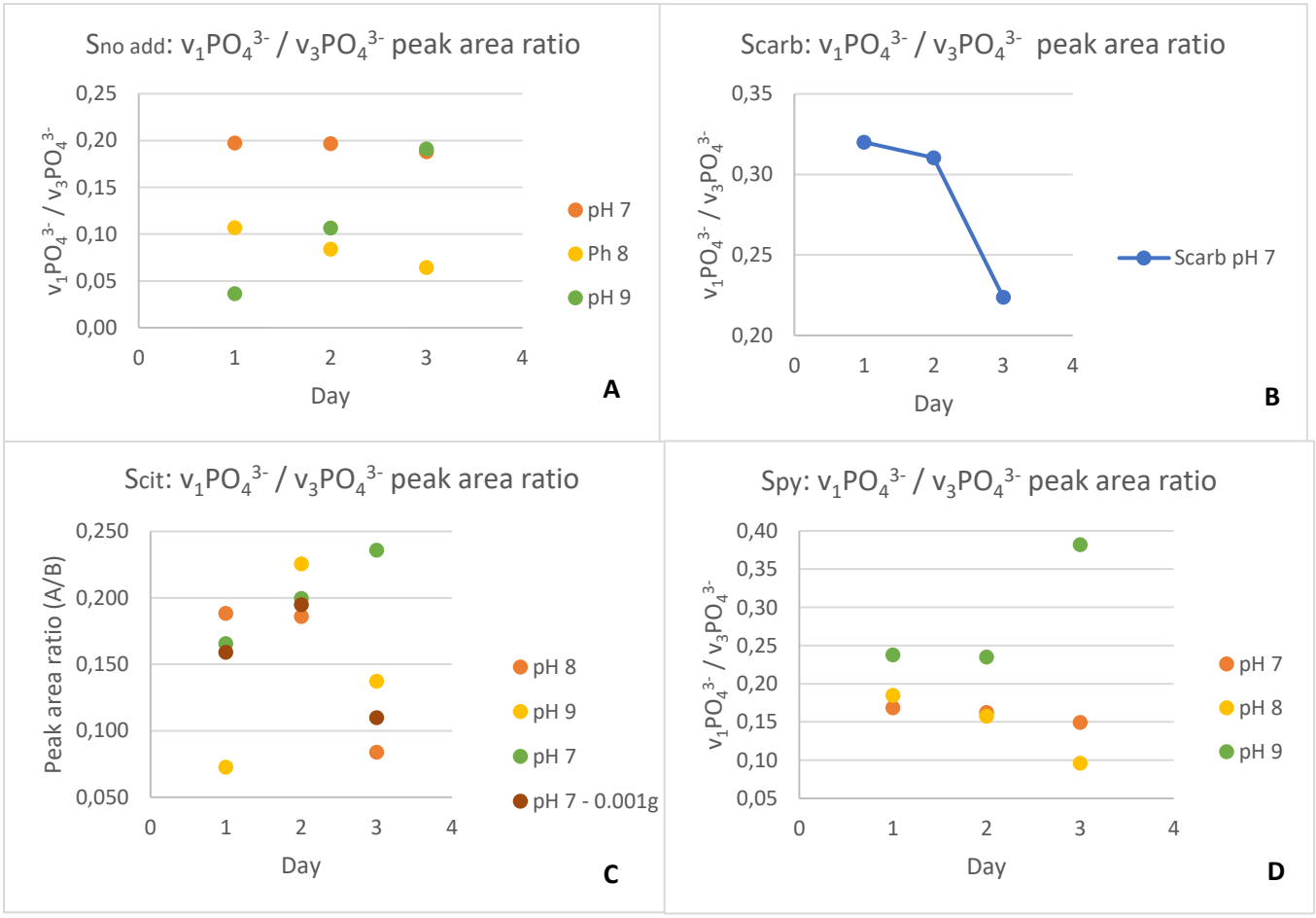

Figure 5: Peak area ratios calculated for peaks within the range 800 – 1300 cm^{-1} for (A)$S_{no\ add}$, (B) S_{carb}, (C) S_{cit}, and (D) S_{py} for all pH levels

When looking at the pH 7 data plots in Figure 6, they are clustered close showing very little change over the days while pH 9 appears to be more scattered; however, there is no trend observed in regards to the days. Overall, no correlation can be found in the different pH levels used or the development over the days when comparing the $v_1PO_4^{3-}/v_3PO_4^{3-}$ against v_3CO_3/v_2H_2O.

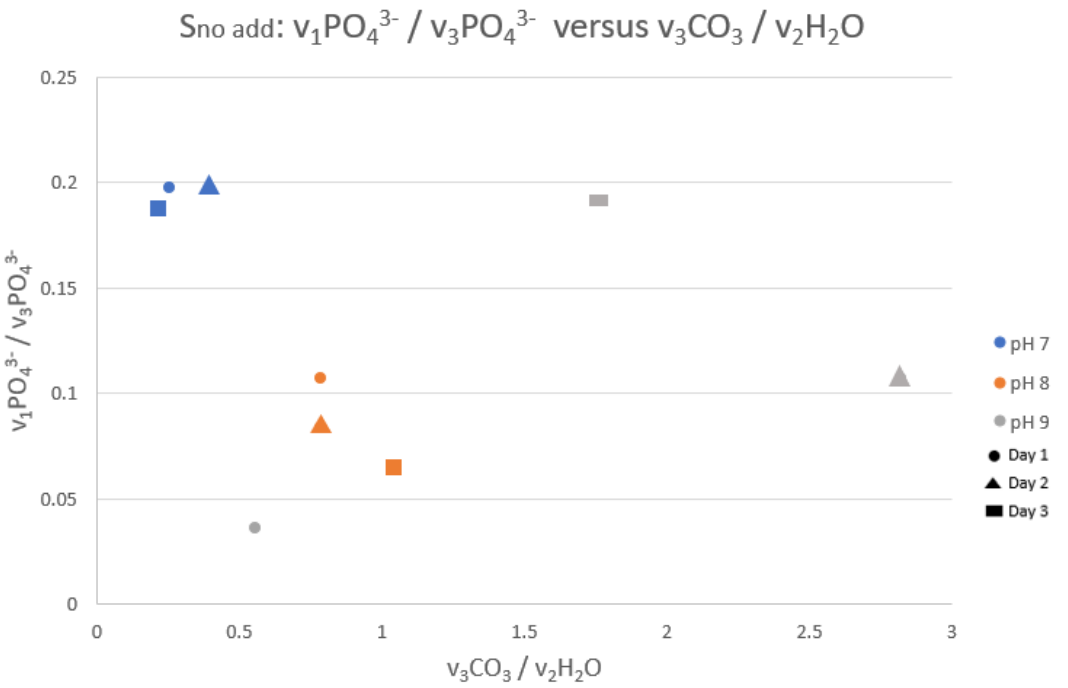

A

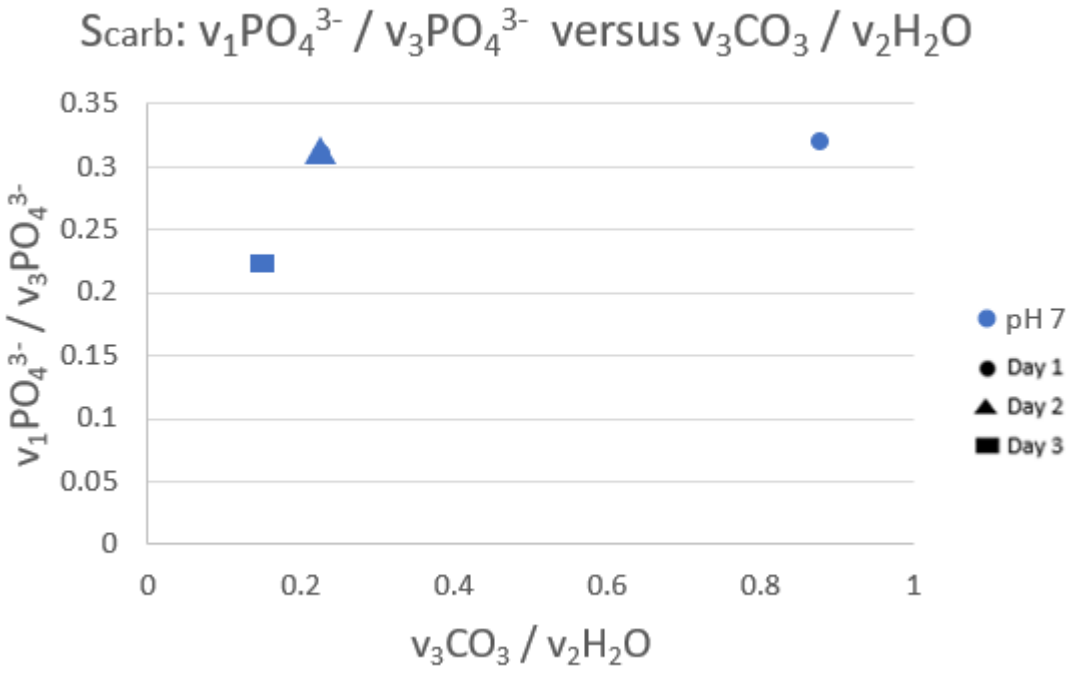

B

Figure 6: Comparing between $v_1PO_4^{3-}/v_3PO_4^{3-}$ and v_3CO_3/v_2H_2O for (A)$S_{no\ add}$, (B) S_{carb}, (C) S_{cit}, and (D) S_{py} for all pH levels

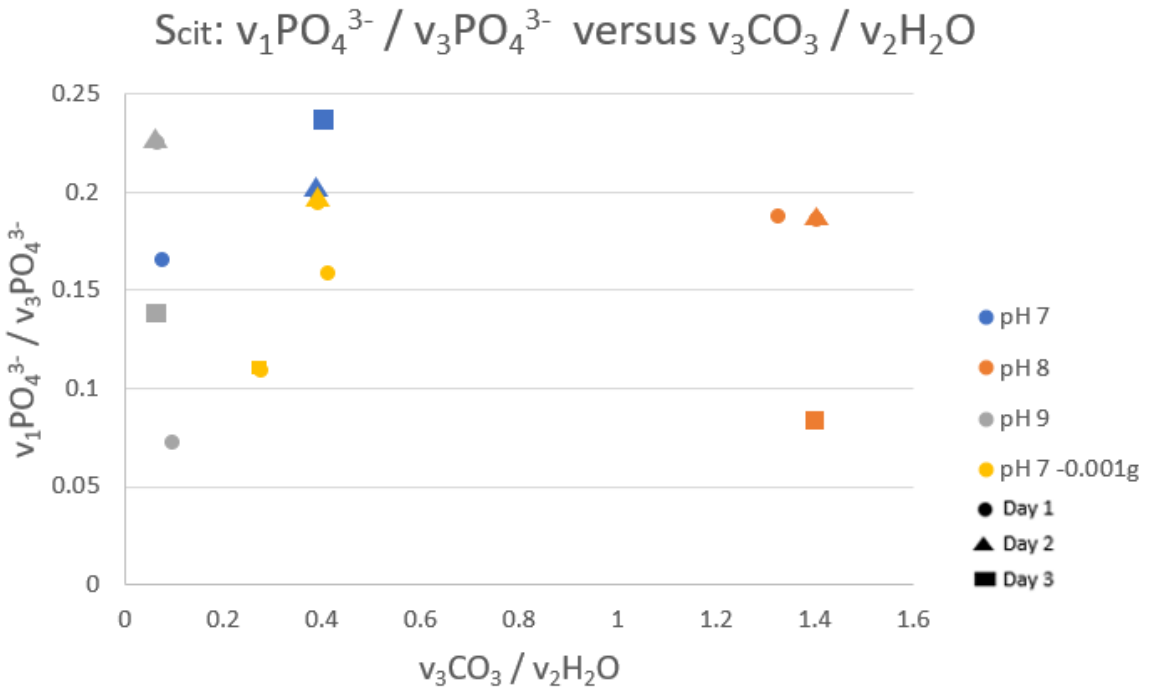

C

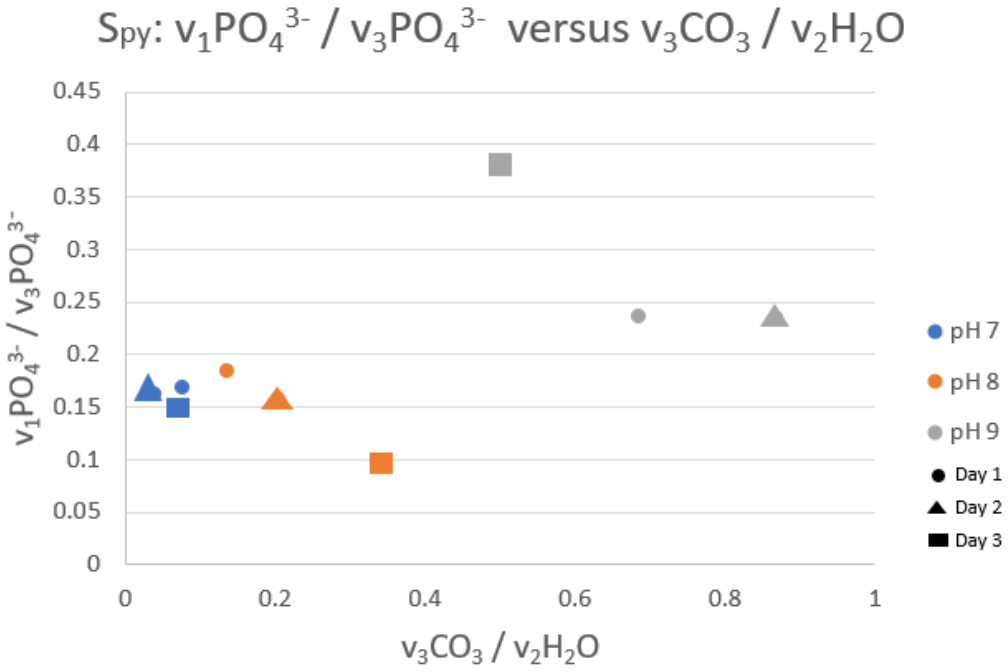

D

Figure 6: Comparing between $v_1PO_4^{3-}/v_3PO_4^{3-}$ and v_3CO_3/v_2H_2O for (A)$S_{no\ add}$, (B) S_{carb}, (C) S_{cit}, and (D) S_{py} for all pH levels

6.6 Crystallinity Index

The crystallinity index was calculated for all the samples using the inverted FWHM for two different bands: $v_1PO_4^{3-}$ at approximately 960 cm^{-1} and $v_3PO_4^{3-}$ at about 1020 cm^{-1} in the spectra (Appendix G). An example of the graph is seen below in Figure 7 for the $S_{no\ add}$ experiments. The graph displays an increase in crystallinity over the three days. All other graphs in Appendix G show increasing crystallinity for both $v_1PO_4^{3-}$ and $v_3PO_4^{3-}$ except S_{cit} sample for the crystallinity of $v_3PO_4^{3-}$, in which pH 7 shows slight increase in crystallinity while pH 8 and 9 show an initial decrease to day two, followed by an increase by day three.

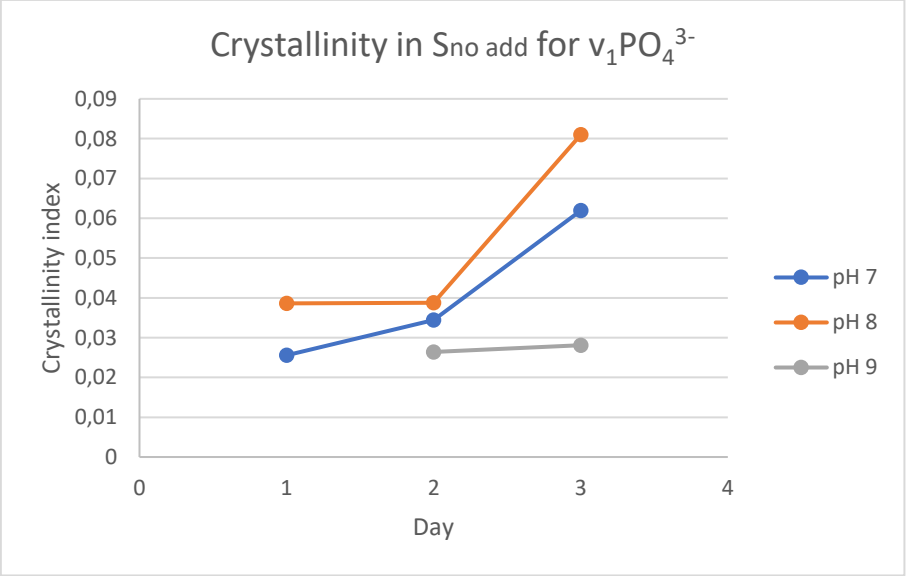

Figure 7: Crystallinity index for the $S_{no\ add}$ experiments for all pH levels

7. Discussion

7.1 Solution condition before precipitation at different pH levels

The experiments conducted used 0.12 M Na_3PO_4 as the solute and 0.1 $CaCl_2$ as the solvent. Solubility is the maximum concentration of a solute which can be dissolved in a solvent at equilibrium, meaning that both the process of dissolution and precipitation are taking place at the same rate (Ruffini et al. 2019).

The equilibrium constant for a solute dissolving in a solution can be described using the solubility product constant K_{sp}. The K_{sp} studies the activity of the system at equilibrium, and as the K_{sp} value increases, the substance becomes more soluble. The difference between the concentration or activity is that concentration is a measure for the amount of dissolved solute in solution while activity is the ''effective concentration'', based on the chemical potential of a species in non-ideal conditions, such as a concentrated solution. For instance, pH measures the activity of H^+. The ion activity product (IAP) is equivalent to the K_{sp} except involves actual measured activities and is a product of solute concentrations. Both the IAP and the K_{sp} are related to the saturation index (SI), which determines the saturation of a solution and is defined as:

$$SI = \log_{10}(IAP/K_{sp}) \qquad \textit{(Equation 1)}$$

A saturated solution is when maximum solubility is achieved and is, therefore, in equilibrium. A solution becomes under- or super-saturated depending on the amount of solute in solution relative to its equilibrium (Cuballis and Anderson, 2010). When:

$SI = 0$	$IAP = K_{sp}$	solution is saturated and in equilibrium
$SI < 0$	$IAP < K_{sp}$	solution is undersaturated, dissolution occurs
$SI > 0$	$IAP > K_{sp}$	solution is supersaturated, precipitation occurs

The thermodynamic driving force for any phase is supersaturation (Bahrig et al.,2014; Johnsson and Nancollas. 1992). Supersaturation drives precipitation of phases, which is the concept that bone growth and the precipitation experiments we had conducted are based on. It forces the synthesis of HA via nucleation and growth; thus, it is a critical parameter for crystallization. In our system, when SI > 0 the HA crystals will form and grow and if SI < 0, the HA crystals will undergo dissolution.

The solubility equations for HA are:

$$Ca_5(PO_4)_6(OH)_{(s)} \rightleftharpoons 5\,Ca^{2+}_{(aq)} + 3\,PO_4^{3-}{}_{(aq)} + OH^-_{(aq)} \qquad \textit{(Equation 2)}$$

$$PO_4^{3-}{}_{(aq)} + H_3O^+_{(aq)} \rightleftharpoons HPO_4^{2-}{}_{(aq)} + H_2O_{(l)} \qquad \textit{(Equation 3)}$$

$$HPO_4^{2-}{}_{(aq)} + H_3O^+_{(aq)} \rightleftharpoons H_2PO_4^-{}_{(aq)} + H_2O_{(l)} \qquad \textit{(Equation 4)}$$

$$OH^-_{(aq)} + H_3O^+_{(aq)} \longrightarrow 2\,H_2O_{(l)} \qquad \textit{(Equation 5)}$$

Changing pH in a system affects the ion concentration of H^+ in solution and oxyanion (e.g., PO_4^{3-}) species distribution, which is known as ionic speciation (Ruffini et al., 2019). Free ions are ions which are available in solution and can interact to make new species called ion pairs or ion complexes. In our system, the Ca^{2+} and PO_4^{3-} readily produce ion pairs, resulting in a decrease of free ions in solution (Johnsson and Nancollas, 1992). The formation of such pairs and complexes can increase the solubility as they increase the K_{sp}, which, in turn, will decrease the NaCl saturation (Equation 1) (Murray, 2004).

Decreasing pH will increase the solubility of a soluble base and a basic salt, following Le Châtelier's Principle. This Principle states that when a change occurs which drives the system away from equilibrium, there will be an opposite reaction to oppose this change and bring the system back to equilibrium. According to a study by Drouet (2013), HA is more stable in alkaline environments, thus, favors forming at higher pH conditions unlike the more acidic Ca-P phases such as OCP, DCPD or DCPA. If the pH is increased, the rate of HA crystal growth would also increase. This is because to produce apatite, PO_4^{3-} is theoretically needed (Equation 2). In a system with protonated phosphate (often also dehydrated), commonly under physiological conditions, crystallizing HA is expected to be at a slower rate as deprotonation has to occur to produce PO_4^{3-} (Gómez-Morales et al., 2013). At higher pH levels, PO_4^{3-} dominates the system over the protonated species HPO_4^{2-}. Thus, with increasing pH, a higher supersaturation of PO_4^{3-} in the system is suggested (Equation 6). As the experiments are conducted at pH 7,8 and 9, the dominant phosphate in this pH range is HPO_4^{2-}, as PO_4^{3-} is more dominant at pH 10 and above. During the unbuffered experiments, there was a significant drop in pH immediately upon the addition of the 0.12 M Na_3PO_4 solution (Appendix A). As the pH of the system is lowered, the additional acid will react with the HPO_4^{2-} and H_3O^+ basic anions resulting in more protonated phosphates, H_2PO_4, shifting the equilibrium of Equation 4 to the right. This results in a solution less saturated of HPO_4^{2-}, allowing the potential for re-dissolution (Meyer and Nancollas, 1972).

For our system:

$$SI = \frac{\{Ca^{2+}\}\{PO_4^{3-}\}\{OH^-\}}{[Ca_5(PO_4)_5(OH^-)]} \qquad \textit{(Equation 6)}$$

Both the IAP and K_{sp} are affected by the system. The K_{sp} equilibrium changes with changing pH and the IAP changes as the PO_4^{3-} react, producing $\{H_2PO_4\}$ and $\{HPO_4^{2-}\}$. These changes are reflected on the SI.

The buffered experiments had an increase in volume as the 0.1 M NaOH or HCl was added per day. Therefore, the saturation of the solution decreased. The change in solution volume relative to the starting volume could have driven dissolution in these experiments was encouraged due to the change in the solution volume rather than changing pH levels. Therefore, whether the volume or pH is changed will have the same effect on the system, encouraging it to re-dissolve. However, as the crystalline phase can form in the unbuffered experiments, it appears not to have the ability to dissolve and re-precipitate in the buffered experiments.

As seen in Figure 8, DCPD and HAP intersect around pH 4. Above pH 4, DCPD has a higher solubility and is, therefore, less stable compared to HAP. HAP is the most thermodynamically stable phase, followed by TCP, OCP, and finally, DCPD (Pinto et al., 2011). Geochemical modeling software PHREEQC was used to simulate speciation for six of our experiments. The tests simulated were $S_{no\ add}$ at pH 7,8 and 9; S_{carb} at pH 7 and S_{cit} at pH 7 and 8. The program was not able to simulate S_{cit} at pH 9. The program was set to simulate equilibration of the solutions with air and to model the presence of a small amount of CO_2 in solution through this interaction as our experiments were exposed to atmospheric CO_2. The log [P] for all simulations are plotted into Figure 8. All values plot above the DCPD isotherm; thus, there is enough P in the solution for it to be supersaturated with respect to this phase. All plotted points on Figure 8 suggest that our experiments were supersaturated with respect to all the phases that are in the diagram. Thus, our solutions are of a composition that any of the precursor phases and HA could have precipitated.

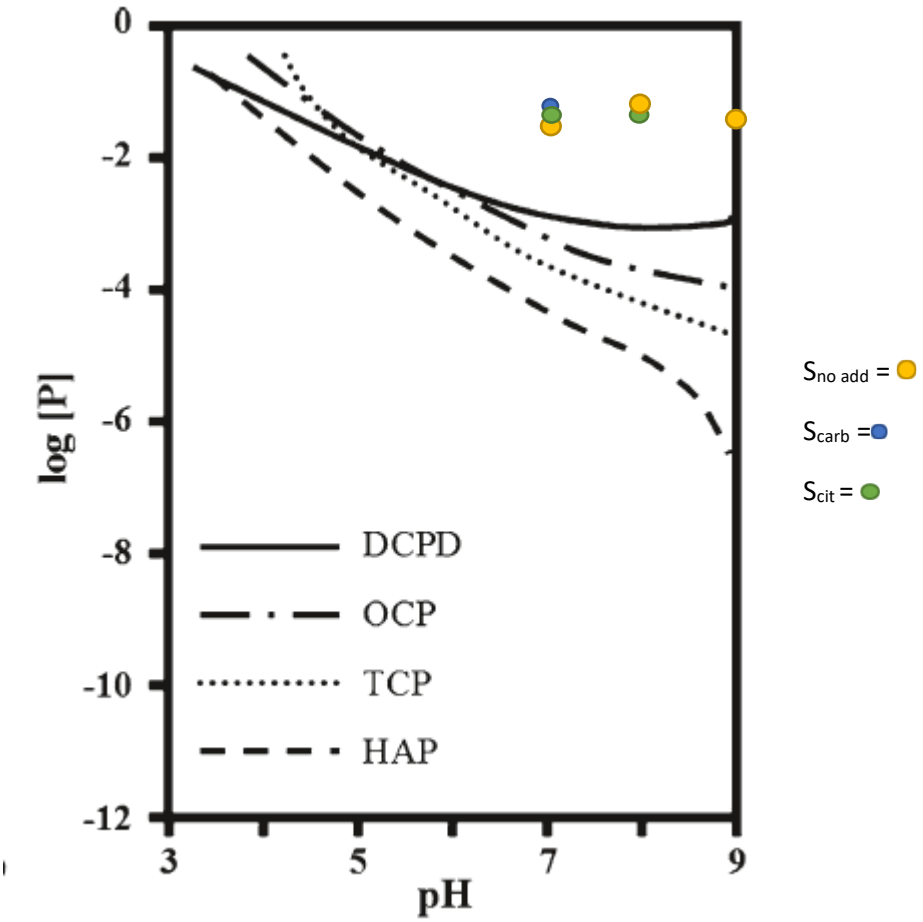

Figure 8: Demonstrates the dependence of pH on the different phases of calcium phosphate indicated by the solubility isotherms. Where log [P] - total phosphate molar concentration, DCPD - Brushite, OCP – octacalcium phosphate, TCP – tricalcium phosphate, HAP – hydroxyapatite. As pH increases, the phases become less soluble and below pH 6, all phases become soluble. Taken from Pinto et al., (2011). Plotted points represent the log [P] for our experiments. Data was collected by simulating the solutions tested in the program PHREEQC for the tests $S_{no\ add}$ at pH 7,8 and 9; S_{carb} at pH 7 and S_{cit} at pH 7 and 8.

7.2 Precipitated phases

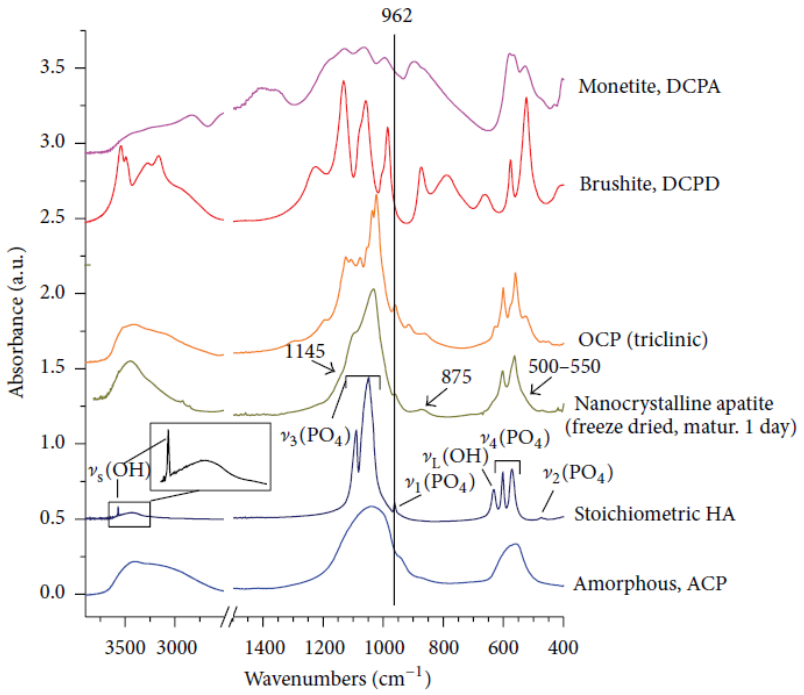

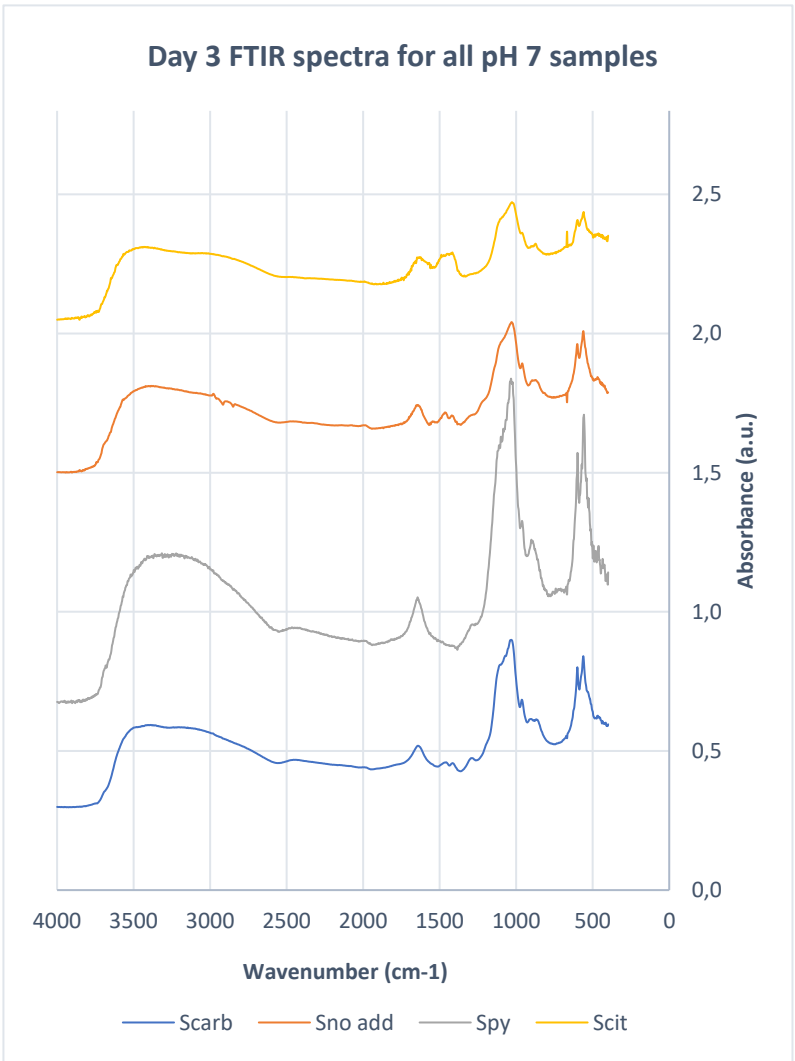

Phase identification is obtained from vibrational spectroscopy based on characteristic bands associated with different Ca-P phases. For example, the dominant v_3 PO_4^{3-} band for OCP is at 1030 cm^{-1}, and for ACP at 1060 cm^{-1}. Although both phases are related to the same motion, the structure of the material is different, leading to a band shift (Sauer and Wuthier., 1988; Mróz et al., 2010).

Our FTIR spectra (Appendix B) were compared to those from different Ca-P phases in Figure 9A taken from the paper by Drouet (2013). A summary of the phases precipitated per sample studied per day are found in Table 8. The representative spectra of the day three pH 7 samples are shown in Figure 9B.

Samples coinciding with the spectrum of nanocrystalline apatite, such as $S_{no\ add}$ pH 7 or S_{carb}, all share the same trend of a band envelope present between 900 and 1200 cm^{-1} with a shoulder around 962 cm^{-1}. The spectra also have two bands are located at 550, and 600 cm^{-1} and the band present at 875 cm^{-1} in Drouet (2013) is positioned around 896 cm^{-1} in our samples. The main band between 1000 and 1200 cm^{-1} is tall and gently slopes down at higher wavelengths. Although the remainder of the spectra appears like OCP, our FTIR data is missing the sharp, characteristic split band at 1030 cm^{-1}. Unlike previous studies, our FTIR spectra show evidence for CO_3^{2-} incorporation, which may lead to the discrepancy in band positions found in our spectra and the reference spectra in Figure 9.

Figure 9A Characteristic FTIR spectra for a range of apatitic phases taken from the paper by Drouet (2013)

Figure 9B Day three FTIR spectra obtained for all samples. The S_{cit} sample with 0.001 g citrate in solution was used as it is more representable. The S_{carb} spectra is shifted up the vertical axis by + 0.5; S_{py} by + 1; $S_{no\ add}$ by + 1.5 and S_{cit} by + 2, in order to make the figure more comparable.

Spectra similar to ACP in Figure 9, like S_{py} and S_{cit} pH 8 day one spectra, all have a poorly defined band between 500 and 600 cm^{-1}, broad single band between 1000 and 1200 cm^{-1} and a weak 960 cm^{-1} shoulder band present.

The S_{cit} pH 8 day two and three spectra appear to be transforming from OCP to nanocrystalline apatite. The spectra up to 1000 cm^{-1} matches OCP more due to developed peaks between 500 and 600 cm^{-1} and two bands present at 842 and 901 cm^{-1} which are absent in the nanocrystalline apatite spectrum. However, the main band at 1000 cm^{-1} is missing the characteristic split band specific to OCP. No corroborative identification of OCP was obtained in Raman spectroscopy pH 8 analysis, in which OCP bands would be expected to be present at approximately 918 and 1116 cm^{-1} (Appendix E.4.3).

The S_{cit} pH 7 with 5.88 g citrate and pH 9 spectra (Appendix A.3) do not match any spectra in Figure 9. For example, the pH 7 day one spectrum has three bands present in between 450 and 680 cm^{-1}, similarly as in Brushite. However, the rest of the spectra does not coincide. No shoulder band is present around 962 $cm^{-1,}$ and the bands are too sharp and narrow to match that of ACP. The pH 9 spectra produced broad, undefined bands like ACP but many bands are present below 1000 cm^{-1} which is not characteristic for the ACP spectrum.

Table 9: Summary of the phases precipitated per sample per day, samples were compared with spectra from Figure 9A. Nanocry. Ap. = Nanocrystalline apatite; ACP = Amorphous calcium phosphate and OCP = Octacalcium phosphate

		Phase precipitated (day)		
Sample	**pH**	**1**	**2**	**3**
$S_{no\ add}$	7	Nanocry. ap.	Nanocry. ap.	Nanocry. ap.
	8	ACP	Nanocry. ap.	Nanocry. ap.
	9	ACP	Nanocry. ap.	Nanocry. ap.
S_{carb}	7	Nano ap.	Nanocry. ap.	Nanocry. ap.
S_{py}	7	Nanocry. ap.	Nanocry. ap.	Nanocry. ap.
	8	ACP	Nanocry. ap.	Nanocry. ap.
	9	ACP	ACP	ACP
S_{cit}	7*	Nanocry. ap.	Nanocry. ap.	Nanocry. ap.
	7	No match	No match	No match
*0.001 g citrate used	8	ACP	OCP/ Nanocry. ap.	OCP/ Nanocry. ap.
	9	No match	No match	No match

7.3 Chemical feedbacks and maturation pathways with no additives

The $S_{no\ add}$ unbuffered experiments produce very similar spectra to one another over the six days even though the pH changed throughout the chemical reaction. An example of this is seen in Figure 10 below, showing the FTIR spectra produced for the pH 7 run for day one and day six. The only exception is that the relative intensity of the bands is much greater in the pH 8 spectra compared to those in pH 7 and 9 (Appendix B.1.2). Primary banding is produced between 500 and 1800 $cm^{-1,}$ and the number of bands produced is the same in similar positions. However, these bands are more defined with higher pH.

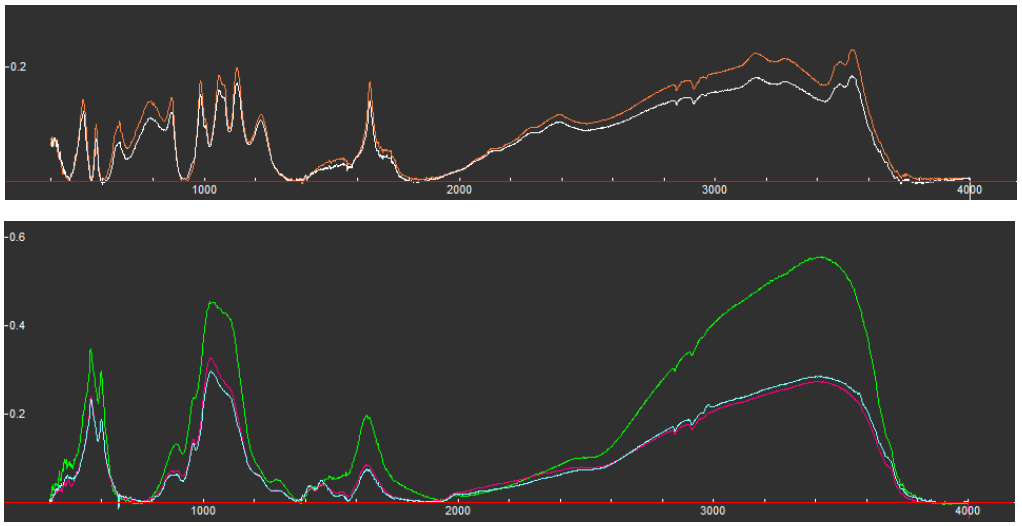

Figure 10, (A) The $S_{no\ add}$ pH 7 unbuffered run FTIR spectra, where White – Day one and Orange – Day six, (B) All three days of $S_{no\ add}$ at pH 7, buffered experiment: Green – Day one, Pink – Day two and Blue – Day three

Parameters such as pH can affect the formation of apatites as it alters ionic speciation. Within a Ca-P system precipitating apatite, it is common that pH will affect the concentration of the PO_4^{3-}, HPO_4^{2-} and $H_2PO_4^-$ ions, but also the Ca^{2+} and OH^- ions. According to Drouet (2013) and Vandecandelaere et al. (2012), during (hydroxy) apatite precipitation, OH^- ions are incorporated into the structure which suggests possible acidification of the solution, which may result in an inappropriate pH for the desired apatite to form. This acidification was confirmed as the pH significantly drops from initial pH for all samples during the unbuffered run upon mixing the 0.12 M NaH_2PO_4 solution is added to the 0.1 M $CaCl_2$ solution (Appendix A) which was also seen in the pH data of Klop, (2015). Such low pH levels can result in the formation of other apatite forms which are stable at lower pH levels such as the apatite precursor OCP which preferentially forms at pH 4-6.5 (Pompe, 2015), brushite or monetite (Drouet, 2013). On the other hand, HA precipitates preferentially in alkaline environments, ideally between pH levels 7.4 to 8.4 (Inskeep and Silvertooth, 1988; Lazić, 1995; Drouet, 2013). As the pH influences the PO_4^{2-} balance in solution, with decreasing pH, there is a shift in PO_4^{2-} species in the order by:

$$PO_4^{3-} \rightarrow HPO_4^{2-} \rightarrow H_2PO_4^- \rightarrow H_3PO_4$$

With lower pH, the phosphates are more protonated, and therefore, precipitation is not as favored. (Gómez-Morales et al. (2013)

Comparing the buffered $S_{no\ add}$ spectra with those from the unbuffered run we can conclude two main differences (Figure 10A and B). Firstly, more bands are produced in the unbuffered series, and second of all, these bands are initially narrower (Appendix B.1). Therefore, the unbuffered run provides more structured and crystalline material as of the start. For instance, in the pH 7 spectra, the 1640 cm^{-1} band has an initial FWHM of 40.02 and 112.78 cm^{-1} in the unbuffered and buffered run respectively and drops to 38.36 and 81.34 cm^{-1} by the end of the experiment. Both bands increase in crystallinity throughout the experiment; however, the band is more crystalline initially without pH control. The same band in pH 8 and 9 experiments follows the same trend. A similar example is a band around 1025 cm^{-1} for all three pH levels, which decreases in FWHM over time from approximately 94.1 to 72 cm^{-1}, indicating that the material matures to a more organized phase. Overall, the buffered experiments show increasing crystallinity over time. No specific trend is observed with the unbuffered run as various bands show increasing FWHM while others are decreasing over time, excluding that initial crystallinity of the bands is of a higher degree compared to the initial buffered spectra. This increase and decrease visible in FWHM for different bands may perhaps be due to the appearance of new bands within the band envelope that are not distinguishable which may skew the FWHM data. The changes in FWHM values are much more significant for the experiments in which pH was controlled, and the FTIR spectra for both the unbuffered and buffered experiments show that at higher pH levels, more bands are present with greater changes in the band parameters with maturation time. For example, the $S_{no\ add}$ pH 8 and 9 spectra show a more defined formation of the v_3 CO_3^{2-} doublets between 1400 and 1600 cm^{-1} while the pH 7 run shows less developed bands in the same region (Appendix B.1). Therefore, it appears that at higher pH, there is a higher reactivity in solution.

So, the effect of pH buffering slows down recrystallization within the system, which is observed as the PO_4^{3-} bands become narrower over the days as the experiment takes place, increasing the crystallinity, allowing the bone to mature and change over time. Bones are required to remain highly reactive to have the ability to continuously re-model and play a role in body homeostasis as bones act as an ion reservoir. Therefore, the material should preferentially be semi-crystalline and is a non-stoichiometric HA allowing for cation and anion vacancies present in the structure and reducing the crystallinity of the material (Gómez-Morales et a., (2013).

Many studies, such as by Drouet (2013) and Liu et al. (2000) suggest that precursor phases are present before HA precipitation, in which ACP transforms into OCP, then into Ca-deficient HA and finally into HA. In the current experiments, ACP formed initially on day one for the $S_{no\ add}$ pH 8 and 9, S_{py} pH 8 and 9 and S_{cit} pH 8 experiments (Table 9). ACP has a less ordered crystal lattice compared to a more crystalline phase; thus, its interfacial energy is lower, especially if also hydrated. Therefore, ACP is likely to precipitate first in solution prior to transforming into a more stable and crystalline phase such as OCP (Gómez-Morales et al., (2013). A study by Meyer and Weatherall (1982), observed that ACP formed first in the initial slow stage of the reaction taking place, also known as the induction period and was followed by the precipitation of a crystalline apatite phase after the induction period when the reaction is accelerated. The induction period in Meyer and Weatherall's research (1982) showed a decrease in the time taken as the pH levels became more alkaline within pH range of 7 to 10.20, but increased in length again at pH levels higher than 10.20 as there was a drop in HPO_4^{2-} in the solution and increased $CaPO_4$ (Meyer and Weatherall, 1982; Lazić, 1995). With a shorter induction period, there is less time for ACP to precipitate properly; thus, more likely to form a different phase. In comparison to Meyer and Weatherall's (1982) data, the higher pH samples (8 and 9) in the current study produced ACP initially (Table 9), however, these experiments were below pH 10.20, suggesting decreased induction period, perhaps other external factors played a role in the precipitation of ACP other than the induction period.

By maintaining pH, the auto-catalytic reaction is slowed down. An auto-catalytic reaction is a reaction in which a product or products are also a reactant. Such reactions often have a slow, induction period as little catalyst is present, which is followed by a rapid increase in the rate of production. This quick and progressive increase is due to the increase in catalyst content. Once the concentration of the reactant decreases as it is used up, the reaction will slow down, producing a sigmoid curve. Such a reaction was observed in the study conducted by Meyer and Weatherall (1982) as ACP initially precipitated during the slow induction period before forming apatite. As the pH changes due to precipitation to facilitate crystallization of a new and more stable phase such as HA, the recrystallization of the system is seen as auto-catalytic. With decreasing pH, we increase the ability of the system to be crystalline.

7.4 Additive influence on the reaction pathway

During the precipitation of Ca-phosphate phases, additional molecules in solution may affect the nucleation and growth. Such molecules include small ions such as citrate and pyrophosphate, human serum albumin and even simple ions (e.g., F^- or Zn^{2+}). According to Johnsson and Nancollas (1992), anionic proteins have a significant influence on HA crystallization at physiological pH compared to neutral or cationic ions, as they bind to surface Ca^{2+} and active growth sites that have been produced during crystal growth. The additives studied in our experiments were the addition of citrate, pyrophosphate, and carbonate.

Whether pH was controlled or not during the experiments and whether inhibitors such as citrate or pyrophosphate were added into the solution, did not alter the system pathway taken significantly and produced spectra that are apatitic, demonstrating that the inhibitors did not change the reaction pathway greatly (Figure 11). In Figure 11, the pH 7 day three samples of the S_{cit} and S_{py} run were compared to $S_{no\ add}$. As S_{cit} with 0.001 g citrate in solution was representable for the study and was only conducted at pH 7, all pH 7 spectra were used for comparison. However, the S_{py} pH 7 spectra showed to be different from those of pH 8 and 9 which appear more like the $S_{no\ add}$ spectra and is thus, a S_{py} pH 8 spectrum was also plotted for comparison. Overall, the bands are found in similar positions. The only exception was for the 5.88g S_{cit} samples, which showed that using an excessive amount of the citrate inhibitor in solution resulted in calcium citrate crystal formation instead of HA.

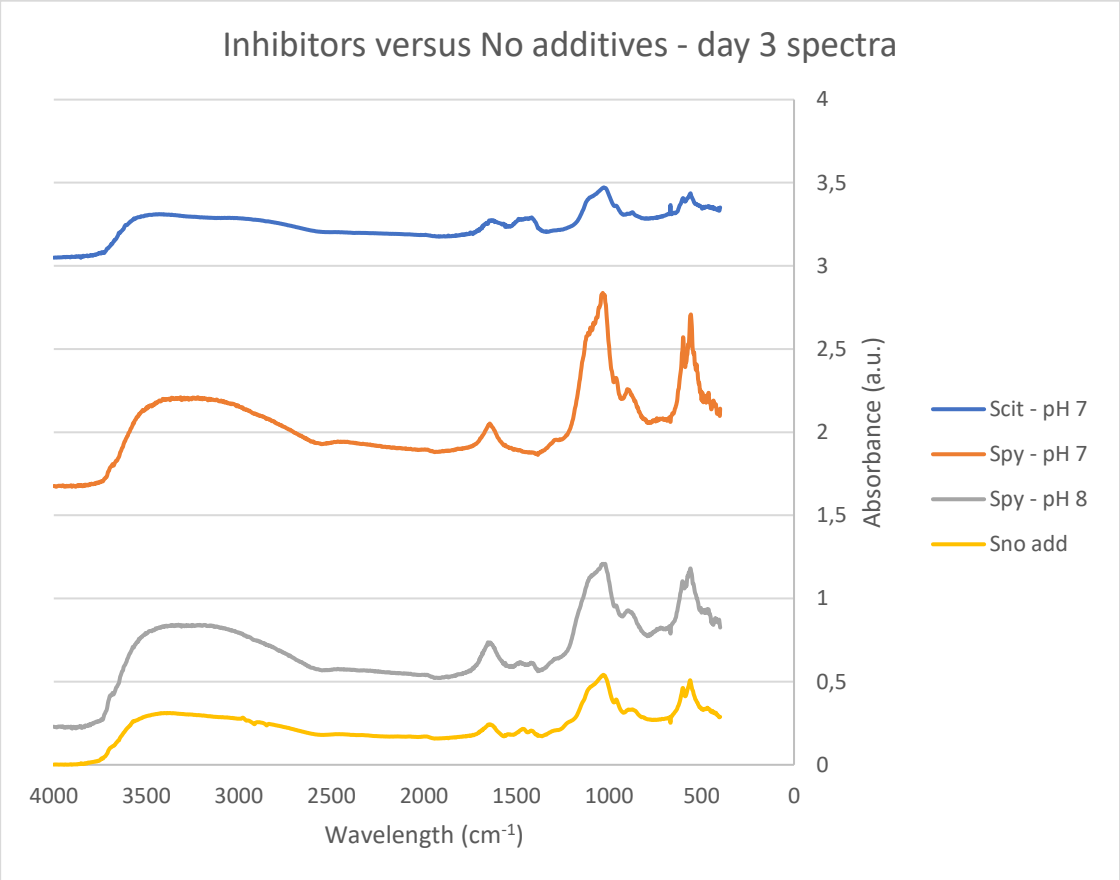

Figure 11 Comparison of the no additive spectrum at pH 7 with spectra tested with inhibitors present: Citrate at pH 7 and Pyrophosphate at pH 7 and 8, all spectra are from the day three FTIR analysis

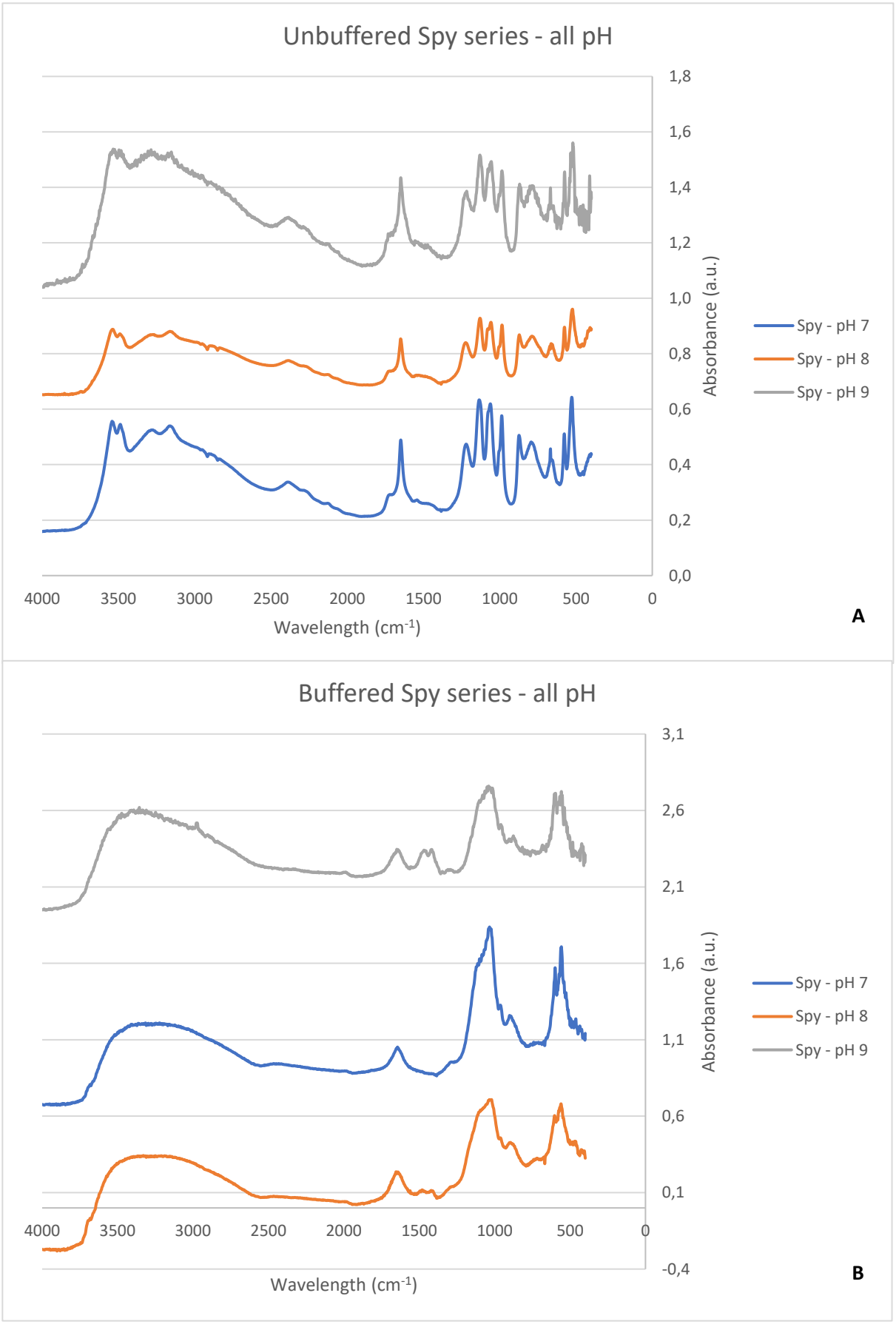

Figure 12 (A) The S_{py} unbuffered series for day six for all pH levels; (B) The S_{py} buffered series for day six for all pH levels

The FTIR spectra for both the unbuffered and buffered experiments for all pH levels show that overall with higher pH levels more bands are present and/or there are greater changes in the band parameters, as bands become more evolved with maturation time (Figure 12A and 12B). For example, as seen in Figure 12B, the buffered pH 7 S_{py} sample has a single broad v_3 CO_3^{2-} band present between 1400 and 1600 cm^{-1} over the three days, while the pH 8 and 9 samples have a doublet v_3 CO_3^{2-} band from day one between 1400 and 1500 cm^{-1} which continues to evolve and an additional v_3 CO_3^{2-} band present between 1500 and 1600 cm^{-1}, confirming that at higher pH, there is a higher reactivity in solution.

7.4.1 Citrate

The 0.001 g pH 7 S_{cit} sample showed no significant changes in its FTIR or Raman spectra over the three days and are more apatitic compared to the 5.88 g S_{cit} samples and is, therefore, more representative for the aim of this study (Appendix B.3 and D.4). The S_{cit} (5.88 g) pH 7 experiment showed slightly more apatitic Raman spectra on day one, but becomes more citric by day two and three, most likely due to the dissolution of the sample (Figure 13B). As the experiment continued, re-dissolution allowed re-liberation of Ca atoms which allowed to form the small amount of apatite found in the day one spectrum. The S_{cit} (5.88 g) pH 7 sample produced very little precipitate, suggesting that citrate inhibits the formation of apatitic phosphate at pH 7 when present in high concentrations, producing citrate crystals. Citrate readily bonds with Ca in two ways, either a citrate molecule binds to a Ca atom or two citrate molecules bond and then bind together to one Ca atom, inhibiting the nucleation of apatite (Coe, n.d.). Referring to Figure 1B in the introduction, the 5.88 g S_{cit} samples follow the initial nucleation but cannot grow into HA due to a lack of material. Therefore, the PO_4^{3-} that manages to form is not stable, re-dissolves, and the second nucleation of calcium citrate occurs. On the other hand, with lower citrate content the chemical reaction directly goes into the apatitic phase as seen in the S_{cit} (0.001 g) pH 7 sample (Figure 13A), in which the precipitate remained after being immediately produced.

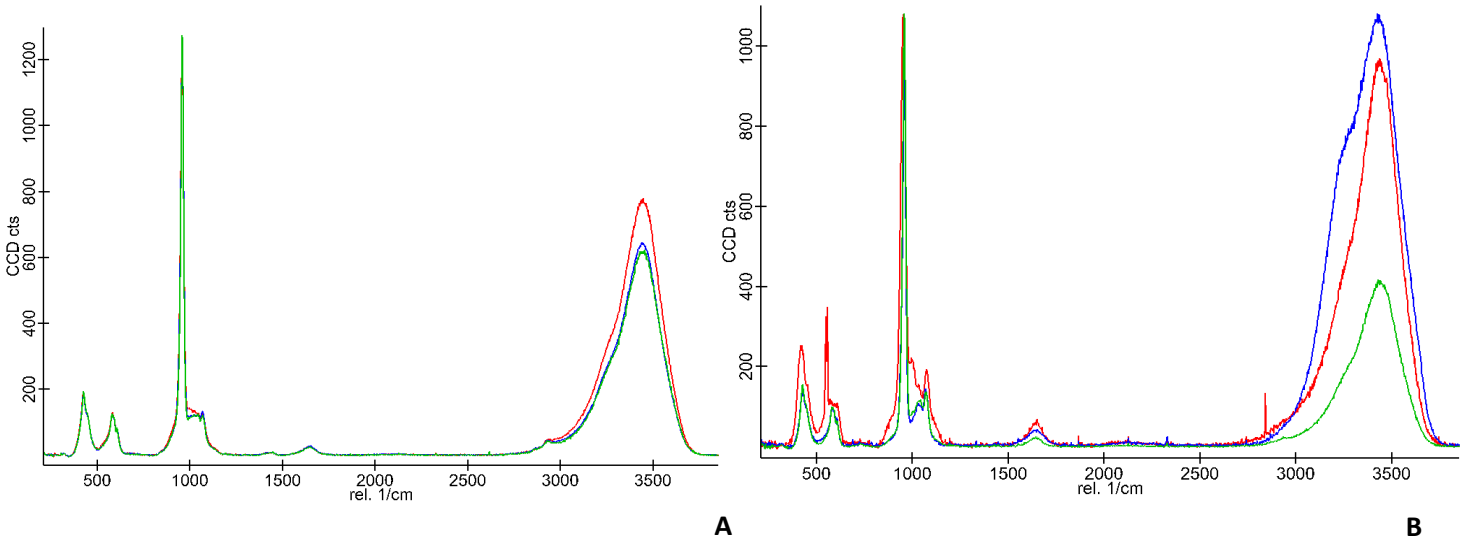

Figure 13 Raman spectra of the buffered experiment precipitates from the S_{cit} samples in which, Red – day one, Blue – day two and Green – day three; (A) S_{cit} sample with 0.001 g citrate in solution; (B) S_{cit} sample with 5.88 g citrate in

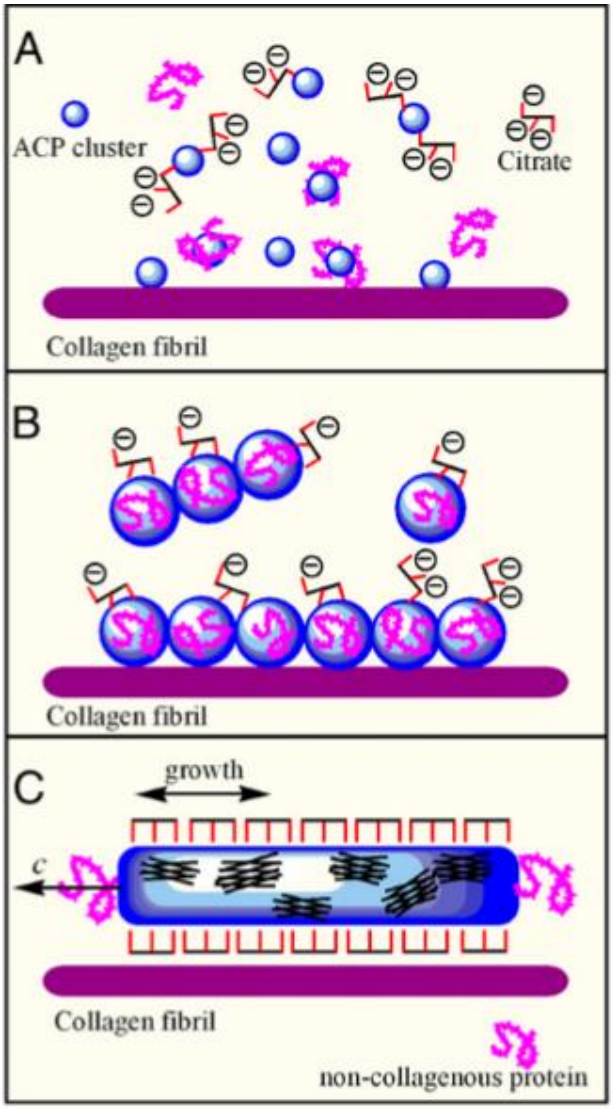

Figure 14: Diagrams showing citrate molecules control over HA crystal synthesis. (A) Citrate partly binding to ACP clusters during nucleation (B) ACP clusters increase in size (C) apatite crystals form, citrate molecules and apatite surface carboxylate groups match in orientation, reducing the spacing between them. Figure taken from Xie and Nancollas (2010)

A report conducted by Xie and Nancollas (2010), studied how strongly binding citrate molecules inhibit the thickness of crystal growth in bone using an advanced multi-NMR spectroscopy and distance measurements. During the early nucleation, ACP clusters precipitate in supersaturated Ca-P solutions. If citrate molecules are present in this stage (Figure 14A), some may partially bind to the surface of the ACP formed, slowing down the growth of the cluster and therefore increasing the time of induction. Citrate molecules which attach to the surface can only slow down the process of nucleation as the spacing between the carboxylate group of citrates and the ACP cluster surface are not aligned, resulting in lower binding density. As nucleation continues, the ACP cluster grows with the help of non-collagenous proteins in the system, and the collagen fibrils assemble the ACP clusters in a preferred orientation on the collagen surface. Within the larger clusters, pre-nuclei may form (Figure 14B), promoting a minor increase of the citrate attached surface area. Once an apatite nucleus is formed, inhibition of crystal growth occurs as the citrate molecule spacing of the carboxylate group is nearly parallel to the apatite Ca^{2+} found on the c-axis. This results in inhibited crystal thickness growth by the citrate molecules (Figure 14C), which explains the plate-like habit of the apatite crystals found in bones.

Citrate is considered to be an inhibitor to the growth of HA crystals. In the presence of citrate, HA precipitates with a decrease in crystal size, more structural imperfections, and a higher content of CO_3^{2-} (van der Houwen et al., 2003). In Wilson's et al., (1985) experiments, diluted urine, and a seeded crystal growth system was used to test the inhibitory activity. The samples were run at pH levels 5.80, 6.60, and 7.40 at constant supersaturation using the constant composition technique to study the crystal growth and understand the effect of pH on the inhibitor. The study used the Langmuir adsorption isotherm to calculate the inhibitor activity. This activity was expressed in Inhibitor units per liter, the amount of material causing 50% crystal growth rate reduction in the controlled system studied and concluded that citrate inhibitory effects increased with a decrease in pH requiring 50% increase in citrate content to slow the rate of crystal growth. Due to variation of only one order of magnitude in inhibition activity, Wilson et al. (1985) suggest that pH may not be the determining factor for inhibition in HA growth activity such as the formation of citrate complexes. When comparing the

experiments with ours, their experiments were always kept in the growth phase by keeping the system supersaturated, while our experiments allowed for changes in molarity and supersaturation of the system. From the 0.001 g S_{cit} sample being most representative to this study, no inhibition of HA formation was observed. Perhaps if the experiments would have all be done with 0.001 g of citrate present up until pH 5, we may have seen similar results as the Wilson et al. (1985) study.

7.5.2. Pyrophosphate

In the presence of inorganic pyrophosphate, mineralization of ''soft'' tissues forming may be inhibited as it blocks the binding sites on the crystal surface (Addison et al. 2007). However, its degradation into PO_4^{2-} within bones and teeth would stimulate crystal growth. Addison et al. (2007) used osteoblast cultures to gain insight into pyrophosphate effect on osteoblasts during bone formation and concluded that with high concentrations of extracellular inorganic pyrophosphate present, direct synthesis and mineralization of HA is repressed by adsorbing to the attachment sites of the growing crystals. A study by Ibsen and Birkedal (2018) on the effect of pyrophosphate on apatite crystallization concluded that pyrophosphate acted as a potent inhibitor. With pyrophosphate present in solution, the rate at which the amorphous material transforms into crystalline material and the nucleation time was affected, as well as crystallization onset being increased from a minute to an hour timescale and a reduced rate of growth in crystals produced. To what extent the nucleation time is affected depends on the concentration of pyrophosphate added to the solution. The experiments were run by mixing 0.2 M $CaCl_2$ and 0.12 M Na_3PO_4 at pH 12 and 60°C with HO_4P^{2-} as the main species present.

On the contrary, in the experiments that we have run using pyrophosphate, there appears to be no inhibitory effect as the spectra produced by the FTIR and Raman show apatitic phases present (Appendix B and D). The reason for the difference observed may be due to different set of conditions used by Ibsen and Birkedal (2018), although both experiments used 0.12 M Na_3PO_4, we used 0.1 M $CaCl_2$ solution at studied pH levels 7,8 and 9 at room temperature. As previously mentioned, apatite preferably forms at pH levels of 7.4 and higher (Drouet, 2013) but below pH levels of 10.20 (Meyer and Weatherall, 1982; Lazić, 1995). Perhaps at such high pH levels such as 12, apatite is already at a disadvantage in terms of precipitating. The pyrophosphate may have been present at too low concentrations within our experiment to have the ability to interact with the Ca in solution to produce complexes, inhibiting HA formation. Compared to previous research, it seems that carbonated hydroxyapatite has more difficulty crystallizing in the presence of pyrophosphate than regular hydroxyapatite. However, this could also be due to the experiments by Ibsen and Birkedal being held at different temperatures.

To understand the difference between the experiments, more research would need to be conducted. Pyrophosphate was also tested by Wilson et al. (1985) alongside citrate as an inhibitor of crystal growth and observed the same trend of inhibitory activity as with citrate. Pyrophosphate increased its activity with a decrease in pH levels and showed to be a stronger inhibitor of the two at a lower pH.

7.5.3 Carbonate

All experiments show CO_3^{2-} being incorporated into the experiments and can be seen from the Raman data on the bands positioned around 1072, 1440 and 1660 cm^{-1} which are attributed to v_3 CO_3^{2-}, as seen in the example Figure 15 below. These bands can be seen in the $S_{no\ add}$ pH 8, S_{carb}, S_{py} pH 8 and 9, and both S_{cit} pH 7 Raman spectra and identification tables (Appendix C and F).

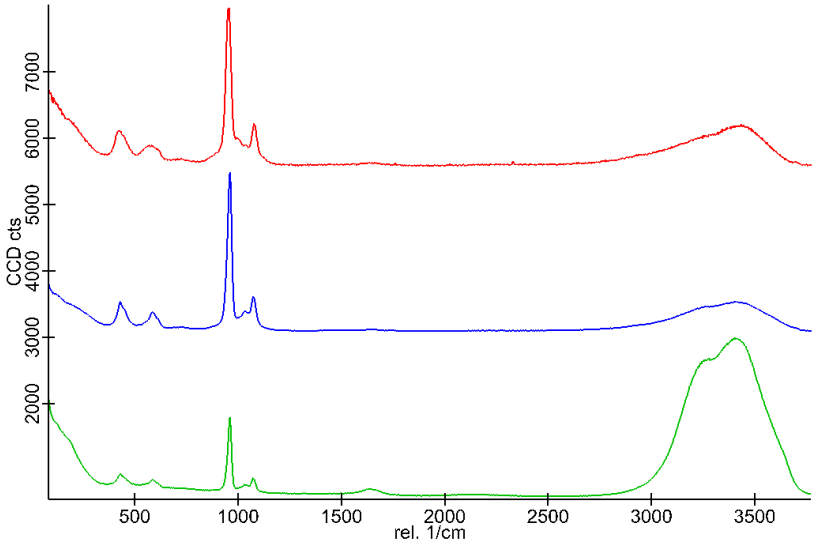

Figure 15 Buffered S_{carb} precipitate Raman spectra, red – day 1, blue – day 2 and green – day 3

According to Sader (2013) and Wopenka (2005), when CO_3^{2-} is present in the B-site, apatite with increased CO_3^{2-} content will be more soluble than HA as the calcium phosphate bonding is stronger than calcium carbonate bonding. According to the Raman data obtained from the current study experiments, the S_{carb} spectra showed a defined band at 1072 cm^{-1} which represents B type v_1 CO_3^{2-} (Penel et al., 1998). This band is also found in the other Raman spectra made for $S_{no\ add}$, S_{py} and S_{cit}, which all have a well-defined band between 1068 and 1081 cm^{-1} which according to Penel et al. (1998) would be attributed to B type v_1 CO_3^{2-}.

With increased structural defects within a crystal structure, the crystal stability is reduced, and there is an increased disorder, making the crystals more susceptible to dissolution (Baig et al., 1996). With a higher CO_3^{2-} content in solution, there is increased CO_3^{2-} incorporation into the crystal structure resulting in the formation of structural defects (Barry, 2002). As mentioned previously in the introduction, there are two types of CO_3^{2-} substitutions that can take place: A-type and B-type substitution, in which ions substitute for the OH^- channel or PO_4^{2-} tetrahedral sites in the apatite structure respectively. During B-type CO_3^{2-} substitution the overall charge balance of a mineral may be disrupted as the ion substituting another ion have the same sign but a different charge, such as CO_3^{2-} replacing for PO_4^{3-}. To return to a neutral charge balance, a second ionic substitution must occur in which CO_3^{2-} with low valence cations are added into the structure (also known as coupled ionic substitution), or a lattice vacancy must be created. Therefore, HA is commonly a poorly crystallized compound as a result of the ionic vacancies present in the Ca and OH^- sites and due to the ionic substitution of CO_3^{2-} or even hydrogen phosphate (HPO_4^{2-}), decreasing the crystallinity and thereby increasing its solubility (Ibrahim et al., 2011). This lowered crystallinity is an essential characteristic of biological apatites such as bones, as they have an important role in bone remodeling (Vandecandelaere et l., 2012).

Based on previous laboratory studies, B-type CO_3^{2-} substitution showed to alter HA physical properties, such as decreasing a-axial length, crystallite size, and increasing c-axial length and solubility (Wopenka, 2005). The level of crystallinity of a mineral describes how stable it is, therefore, with increasing

crystallinity, the solubility decreases (Baig et al., 1996). This statement was confirmed in the thesis by Sleeman (1955) studying the solubility of synthetic HA, in which experiments displayed this relationship between crystallinity and solubility. During a 90 ^{o}C experiment which ran for 96 hours, less soluble but more crystalline HA crystals precipitated compared to the 40 ^{o}C experiment which ran for 24 hours and produced more soluble but less crystalline HA. This was studied by placing flasks with the supersaturated solution into a constant temperature bath and passing CO_2-free N_2 through the experiment preventing CO_2 contamination. X-ray analysis was used to confirm precipitation of HA crystals, and X-ray diffraction was used to test the crystallinity of the samples. Average solubility (K_{sp}) values were calculated for the HA, and regression line slopes were made after precipitation for the different experiments with varying temperature and reaction period after dissolution. The average $K_{sp\ for}$ both precipitation and dissolution showed to be similar and suggested that HA crystal synthesis at temperatures below 90 ^{o}C did not have the conditions of supersaturation in the Ca-P system, and another external factor must have been involved. Results of the average K_{sp} values concluded that as both the temperature and reaction period of the experiments increased the solubility decreased. The research done by de Groot (2017) found that at a constant temperature with increased carbonate content, the phosphate band FWHMs increased in both FTIR and Raman data, resulting in a decreased crystallinity compared to the samples studied with little to no CO_3^{2-} present. Her carbonated calcium phosphate samples showed initial low crystallinity which then increased within 72 hours of the experiment while at the same time, the CO_3^{2-} content decreased. It was concluded that this was the result of CO_3^{2-} incorporation affecting the disorder within the structure. The crystallization rate was also influenced by the CO_3^{2-} incorporation, as the samples studied which had a higher CO_3^{2-} content had a smaller crystallinity increase in the 72 hours compared to the samples with less CO_3^{2-} added.

In the buffered experiments, all the FTIR spectra produced banding between 1400 and 1600 cm^{-1} attributed to v_3 CO_3^{2-}. For example, the pH 8 and 9 $S_{no\ add}$ spectra had a well-defined doublet between 1400 and 1500 cm^{-1} while it is evolving in the pH 7 experiment. On the contrary, the unbuffered experiments have no doublet present in this position. This difference may be due to interaction with atmospheric CO_2 as the unbuffered experiments were sealed for the entire duration while the buffered experiments were not and thus, exposed to the atmosphere. As mentioned before, the crystallinity overall increases over the days for all buffered pH level experiments, including for the doublet band with positions at approximately 1420 and 1470 cm^{-1}. The most crystalline being the pH 7 experiments followed by the pH 8 and lastly, pH 9. For example, in the $S_{no\ add}$ series, the band at 1420 cm^{-1} shows initial FWHM values of 29.89, 45.13 and 53.31 cm^{-1} for pH 7,8 and 9 respectively. These values then decrease to 23.28, 37.09 and 49.36 cm^{-1} by day three. The same trend is seen in the 1470 cm^{-1} band for all experiments. With increasing pH, there is an increased tendency to draw in more CO_3^{2-} from surroundings into the solution. This was confirmed with the degree of crystallinity between the $S_{no\ add}$ experiments conducted, with pH 7 being most crystalline and pH 9 being least crystalline on day one. The v_3 CO_3^{2-} doublet band, is also present and well defined in the majority of the remaining experiments, showing the same trend, apart from the day one S_{py} pH 8, 0.001g S_{cit} pH 7 and the day one S_{cit} pH 9 spectra, in which the doublet is evolving. Thus, the maturation changes and trends may not only be the result of changing pH but can also be explained by the changing CO_3^{2-} content in solution as the CO_3^{2-} present could take the buffering capacity out of the system when it is incorporated leading to potentially local changes in pH in our bodies which are otherwise also pH buffered. Therefore, with increasing pH, the day one spectrum is less crystalline compared to the lower pH experiment, and this may be attributed to the increased CO_3^{2-} content in solution.

8. Conclusions

The main aim of this research was to study the effect of different pH levels on the formation of CHA to understand what factors inhibit and encourage the growth of this phase. This was done by conducting two sets of experiments. The unbuffered run without pH control was done to analyze how pH changes as the chemical reaction progresses for pH levels of 5 to 9. The buffered run, maintained pH throughout the reaction using a stat titrator. The pH levels studied further were 7, 8 and 9 as limited precipitate formed in the pH 5 and 6 samples during the unbuffered run. Samples were made using the double decomposition method between a 0.1 M $CaCl_2$ solution and a 0.12 M Na_3PO_4 solution which has previously been done by Klop (2018) and De Groot (2017). Four different sets of experiments were conducted; without an additive, with CO_3^{2-} and with inhibitor presence of pyrophosphate and citrate.

To identify the mineralogical phases and the maturation of the system over the three days, Fourier transform infrared spectroscopy, and Raman spectroscopy were used. The data obtained from the experiments showed two phases precipitating: ACP and nanocrystalline apatite. Overall, the crystallinity of PO_4^{3-} bands increased over time. The bands that showed a decrease in crystallinity were those that formed newly and were found within band envelopes resulting in unclear FWHM data. The changes in FWHM values were more significant for the buffered experiments. Both the unbuffered and buffered spectra showed that with increasing pH, more bands are produced with greater changes in the band parameters over time, suggesting a higher reactivity. Studies show (Drouet, 2013; Liu et al., 2000) that precursor phases form prior to HA. ACP transforms into OCP, followed by Ca- deficient HA and finally, precipitates to HA. System supersaturation drives precipitation of the phases, when SI > 0 crystallization of HA occurs and when SI < 0, the HA crystals undergo dissolution. Using PHREEQC, speciation for $S_{no\ add}$ at pH 7,8 and 9; S_{carb} at pH 7 and S_{cit} at pH 7 and 8 was simulated with exposure to CO_2 and the log [P] was plotted against pH. All points plotted above the DCPD isotherm, demonstrating that the solutions are of a composition that any of the precursor phases and HA could have precipitated.

According to the study results, the recrystallization of our system is autocatalytic as the pH changes due to precipitation and crystallization is facilitated, which is related to the HA solubility and supersaturation. Increasing pH will also increase the rate of crystal growth suggesting for a higher and effective supersaturated system and promotion of a more crystalline system. This is because at physiological pH levels hydrogen phosphate is dominant and must undergo deprotonation, slowing the rate of crystallization, in comparison to higher pH levels in which PO_4^{3-} is the dominant species. Even though the unbuffered runs showed a drop in pH levels and the buffered experiments had their pH levels kept constant, both experiments had systems encouraging re-dissolution, this was due to change in pH and change in volume of the solution respectively.

We can also conclude that buffering the pH slows down the process of recrystallization, allowing the bone to mature over time, slowing down its autocatalytic reaction. Unbuffered FTIR spectra produced much more crystalline material initially while the buffered FTIR spectra became more crystalline over time, as PO_4^{3-} bands became narrower. The FTIR spectra for both runs showed that at higher pH, more bands were produced, evolved into doublets or became more defined and greater band transitions were observed. Thus, with higher pH levels, there appears to be an increased solution reactivity.

Finally, the inhibitors tested for in our experiments did not show any changes in the reaction pathway as all spectra produced were apatitic in nature and bands are found in similar positions for all experiments. Changing pH or additional inhibitors, unless in excessive content, did not alter the pathway taken. Due to a high content of citrate, with 5.88 g added into solution, the Ca and citrate

preferentially bonded as the solution underwent dissolution and re-precipitation, precipitating citrate crystals instead of HA,. Unlike previous studies, the addition of citrate or pyrophosphate did not show any inhibition as expected, by increasing induction time or increasing inhibition at lower pH. The pH 7 experiments did show less defined and evolved banding compared to those produced in pH 9 experiments. However, this was seen for all experiments, including that with no additives. Therefore, it is more likely due to the pH change and not inhibitor presence.

All buffered experiments were observed to contain CO_3^{2-} in their spectra but was absent in the unbuffered spectra. This difference may be due to interaction with atmospheric CO_2 as the unbuffered experiments were sealed for the entire duration while the buffered experiments were not and thus, exposed to the atmosphere. The crystallinity overall increases over the days for all buffered pH level experiments. With increasing pH there is an increased tendency to draw in more CO_3^{2-} from surroundings into the solution. Thus, the maturation changes and trends may not only be the result of changing pH but can also be explained by the changing CO_3^{2-} content in solution. As the presence of CO_3^{2-} could take the buffering capacity out of the system when it is incorporated leading to potentially local changes in pH in our bodies which are otherwise also pH buffered. Therefore, with increasing pH, the day one spectrum is less crystalline compared to the lower pH experiment, and this may be attributed to the increased CO_3^{2-} content in solution.

In a buffered setting, for example, the effectively buffered system in our bodies in which bones grow, the body will maintain a less crystalline material by slowing down recrystallization as it maintains the high reactivity of a phase. This is preferred compared to a more crystalline material which is produced in the non-buffered experiments, for bone remodeling in which the material should remain reactive.

In order to gain more insight into the effect of pH on bone maturation, more research would need to be conducted. Unlike our experiments, previous studies showed inhibition of HA precipitation by citrate and pyrophosphate. The experiments could be repeated, with 0.001 g of citrate in solution for all S_{cit} pH level experiments and perhaps a higher content of pyrophosphate, as it may have been at too low concentrations within our experiment to have the ability to interact with the Ca in solution to produce complexes, inhibiting HA formation. The repeated experiments would be all be analyzed with Raman spectroscopy to distinguish between phases better, as OCP and HA may be difficult to distinguish in an FTIR spectrum.

References

1. Addison, W. N., Azari, F., Sørensen, E. S., Kaartinen, M. T., & McKee, M. D. (2007). Pyrophosphate inhibits mineralization of osteoblast cultures by binding to mineral, up-regulating osteopontin, and inhibiting alkaline phosphatase activity. *Journal of Biological Chemistry*, *282*(21), 15872-15883.
2. Bailey, A.J., Wotton, S.F., Sims, T.J., Thompson, P.W.: Post-translational modifications in the collagen of human osteoporotic femoral head. Biochem. Biophys. Res. Commun. 185, 801–805 (1992).
3. Bahrig, L., Hickey, S. G., & Eychmüller, A. (2014). Mesocrystalline materials and the involvement of oriented attachment–a review. *CrystEngComm*, *16*(40), 9408-9424.
4. Ben-Nissan, B. (Ed.). (2014). Advances in calcium phosphate biomaterials.
5. Beevers, C. A., & McIntyre, D. B. (1946). The atomic structure of fluor-apatite and its relation to that of tooth and bone material. (With Plates XVI-XVIII.). Mineralogical Magazine and Journal of the Mineralogical Society, 27(194), 254-257.
6. Brecevic LJ, Furedi-Milhofer H (1972) Precipitation of calcium phosphates from electrolyte solutions. II. The formation and transformation of precipitates. Calcif Tissue Res 10:8290
7. Berzina-Cimdina, L., & Borodajenko, N. (2012). Research of calcium phosphates using Fourier transform infrared spectroscopy. In *Infrared Spectroscopy-Materials Science, Engineering and Technology*. IntechOpen.
8. Boudia S, Zuddas P, Fernane F, Fiallo M, Sharrock P. 2018. Mineralogical transformation during hydroxyapatite dissolution in simple aqueous solutions. Chemical Geology. 477:85–91.
9. Combes, C. & Rey, C. (2002). Adsorption of Proteins and Calcium Phosphate Materials Bioactivity. Biomaterials, 23(13), 2817–23.
10. Coe, F. CALCIUM BINDING BY CITRATE | Kidney Stone Evaluation And Treatment Program. Retrieved from https://kidneystones.uchicago.edu/calcium-binding-by-citrate/
11. Crane NJ, Popescu V, Morris MD, Steenhuis P, & Ignelzi MA. 2006. Raman spectroscopic evidence for octacalcium phosphate and other transient mineral species deposited during intramembranous mineralization. *Bone. 39*(3):434-442.
12. Dalmolen, J. (2005). *Synthesis and Application of New Chiral Amines in Dutch Resolution* (Doctoral dissertation, PhD Thesis, University of Groningen).
13. Drouet C. 2013. Apatite formation: why it may not work as planned, and how to conclusively identify apatite compounds. *BioMed research international*.
14. Falcke, H., & Eberle, S. H. (1990). Raman spectroscopic identification of carbonic acid. *Water Research*, *24*(6), 685-688.
15. Featherstone, J., Pearson, S., LeGeros, R., 1984. An infrared method for quantification of carbonate in carbonated apatites. Caries Res. 18, 63-66.
16. Frost, R. L., Xi, Y., Scholz, R., Belotti, F. M., & Lopez, A. (2013). Infrared and Raman spectroscopic characterization of the phosphate mineral fairfieldite–Ca2 (Mn2+, Fe2+) 2 (PO4) 2· 2 (H2O). *Spectrochimica Acta Part A: Molecular and Biomolecular Spectroscopy*, *106*, 216-223.
17. Gómez-Morales, J., Iafisco, M., Delgado-López, J. M., Sarda, S., & Drouet, C. (2013). Progress on the preparation of nanocrystalline apatites and surface characterization: Overview of fundamental and applied aspects. *Progress in Crystal Growth and Characterization of Materials*, *59*(1), 1-46.
18. Gras, P., Teychené, S., Rey, C., Charvillat, C., Biscans, B., Sarda, S., & Combes, C. (2013). Crystallisation of a highly metastable hydrated calcium pyrophosphate phase. *CrystEngComm*, *15*(12), 2294-2300.
19. Hadjidakis, D. J., & Androulakis, I. I. (2006). Bone remodeling. *Annals of the New York academy of sciences*, *1092*(1), 385-396.
20. Ibsen, C., & Birkedal, H. (2018). Pyrophosphate-inhibition of apatite formation studied by in situ X-ray diffraction. *Minerals*, *8*(2), 65.
21. Inskeep, W. P., & Silvertooth, J. C. (1988). Kinetics of hydroxyapatite precipitation at pH 7.4 to 8.4. *Geochimica et Cosmochimica Acta*, *52*(7), 1883-1893.
22. Janssen T. (2018) The effect of pyrophosphate on the crystallization of carbonated hydroxyapatite. Bachelor thesis, Utrecht University

23. Jung, A., Bisaz, S., & Fleisch, H. (1973). The binding of pyrophosphate and two diphosphonates by hydroxyapatite crystals. Calcified tissue research, 11(4), 269-280.
24. Klop, J. (2018). Linking changes in mineral chemistry to reactivity: A study on carbonate incorporation in synthetic hydroxyapatite and its effect on solubility. Master Thesis, Utrecht University
25. King H.E., Tommasini S., Rodriguez-Navarro A.B., Mercado B.Q., Skinner H.C.W. Influence of phosphate deficiency and remodelling regimens in HYP mice bone mineral chemistry and organisation. Accepted for publication in *Journal of Applied Crystallography.*
26. Landi, E., Celotti, G., Logroscino, G., & Tampieri, A. (2003). Carbonated hydroxyapatite as bone substitute. Journal of the European Ceramic Society, 23(15), 2931-2937.
27. Lazić, S. (1995). Microcrystalline hydroxyapatite formation from alkaline solutions. *Journal of crystal growth*, *147*(1-2), 147-154.
28. Li, J., Liu, Y., Gao, Y., Zhong, L., Zou, Q., & Lai, X. (2016). Preparation and properties of calcium citrate nanosheets for bone graft substitute. *Bioengineered*, *7*(5), 376-381.
29. Litasov, K. D., & Podgornykh, N. M. (2017). Raman spectroscopy of various phosphate minerals and occurrence of tuite in the Elga IIE iron meteorite. *Journal of Raman Spectroscopy*, *48*(11), 1518-1527.
30. Macica, C. M., King, H. E., Wang, M., McEachon, C. L., Skinner, C. W., & Tommasini, S. M. (2016). Novel anatomic adaptation of cortical bone to meet increased mineral demands of reproduction. Bone, 85, 59-69.
31. Maréchal, Y. (2011). The molecular structure of liquid water delivered by absorption spectroscopy in the whole IR region completed with thermodynamics data. *Journal of Molecular Structure*, *1004*(1-3), 146-155.
32. Matsuoka, K., Park, K. A., Ito, M., Ikeda, K., & Takeshita, S. (2014). Osteoclast-derived complement component 3a stimulates osteoblast differentiation. *Journal of Bone and Mineral Research*, *29*(7), 1522-1530.
33. Mavropoulos, E., Costa, A. M., Costa, L. T., Achete, C. A., Mello, A., Granjeiro, J. M., & Rossi, A. M. (2011). Adsorption and bioactivity studies of albumin onto hydroxyapatite surface. Colloids and Surfaces B: Biointerfaces, 83(1), 1-9.
34. Meyer, J. L., & Nancollas, G. H. (1972). The effect of pH and temperature on the crystal growth of hydroxyapatite. Archives of Oral Biology, 17(11), 1623-1627.
35. Meyer, J. L., & Weatherall, C. C. (1982). Amorphous to crystalline calcium phosphate phase transformation at elevated pH. *Journal of Colloid and Interface Science*, *89*(1), 257-267.
36. Mróz, W., Bombalska, A., Budner, B., Burdyńska, S., Jedyński, M., Prokopiuk, A., ... & Niedzielski, K. (2010). Comparative study of hydroxyapatite and octacalcium phosphate coatings deposited on metallic implants by PLD method. *Applied Physics A*, *101*(4), 713-716.
37. Murray, J. W. (2004). Activity scales and activity corrections.
38. Naray-Szabo S (1930) The structure of apatite (CaF)Ca4(PO4)3. Z Kristallogr 75:387–398
39. New, S. E. & Aikawa, E. (2013). Role of Extracellular Vesicles in de Novo Mineralization: an Additional Novel Mechanism of Cardiovascular Calcification. Arteriosclerosis, Thrombosis, and Vascular Biology, 33(8), 1753–1758.
40. Office of the Surgeon General (US. (2004). The Basics of Bone in Health and Disease. In Bone Health and Osteoporosis: A Report of the Surgeon General. Office of the Surgeon General (US).
41. Peroos, S., Du, Z., & de Leeuw, N. H. (2006). A computer modelling study of the uptake, structure and distribution of carbonate defects in hydroxy-apatite. Biomaterials, 27(9), 2150-2161.
42. Pinto, O. A., Tabaković, A., Goff, T. M., Liu, Y., & Adair, J. H. (2011). Calcium phosphate and calcium phosphosilicate mediated drug delivery and imaging. In *Intracellular delivery* (pp. 713-744). Springer, Dordrecht.
43. Porfírio, E., & Fanaro, G. B. (2016). Collagen supplementation as a complementary therapy for the prevention and treatment of osteoporosis and osteoarthritis: a systematic review. *Revista Brasileira de Geriatria e Gerontologia*, *19*(1), 153-164.
44. Pompe W, Worch H, Habraken WJEM, Simon P, Kniep R, Ehrlich H, Paufler P. 2015. Octacalcium phosphate – a metastable mineral phase controls the evolution of

scaffold forming proteins. J. Mater. Chem. B. 3:5318-5329.
45. Price, P. A., & Lim, J. E. (2003). The inhibition of calcium phosphate precipitation by fetuin is accompanied by the formation of a fetuin-mineral complex. *Journal of Biological Chemistry*, *278*(24), 22144-22152.
46. Rehman I & Bonfield W. 1997. Characterization of hydroxyapatite and carbonated apatite by photo acoustic FTIR spectroscopy. *Journal of Materials Science: Materials in Medicine*. *8*(1):1-4.
47. Rosenberg, N., Rosenberg, O., & Soudry, M. (2012). Osteoblasts in bone physiology—Mini review. *Rambam Maimonides medical journal*, *3*(2).
48. Ruffini, A., Sprio, S., Preti, L., & Tampieri, A. (2019). Synthesis of Nanostructured Hydroxyapatite via Controlled Hydrothermal Route. In *Biomaterial-supported Tissue Reconstruction or Regeneration*. IntechOpen.
49. Salimi, E., & Javadpour, J. (2012). Synthesis and characterization of nanoporous monetite which can be applicable for drug carrier. *Journal of Nanomaterials*, *2012*, 135.
50. Sauer, G. R., & Wuthier, R. E. (1988). Fourier transform infrared characterization of mineral phases formed during induction of mineralization by collagenase-released matrix vesicles in vitro. *Journal of Biological Chemistry*, *263*(27), 13718-13724.
51. S.K. Haldar, Josip Tišljar, in Introduction to Mineralogy and Petrology, 2014
52. Ślósarczyk, A., Paszkiewicz, Z. and Paluszkiewicz, C. (2005). FTIR and XRD evaluation of carbonated hydroxyapatite powders synthesized by wet methods. *Journal of Molecular Structure*, 744-747, pp.657-661.
53. Sobczak, A., Kowalski, Z., & Wzorek, Z. (2009). Preparation of hydroxyapatite from animal bones. Acta of Bioengineering and Biomechanics, 11(4), 23-28.
54. Thompson, B. & Towler, D. A. (2012). Arterial Calcification and Bone Physiology. Endocrinology, 8(9), 529–43
55. Titov, A. T., Larionov, P. M., Ivanova, A. S., Zaikovskii, V. I., & Chernyavskiy, M. A. (2016). Bone-Like Hydroxyapatite Formation in Human Blood. International Journal of Environmental and Science Education, 11(10), 3971-3984.
56. Tzaphlidou, M. (2008). Bone architecture: collagen structure and calcium/phosphorus maps. *Journal of biological physics*, *34*(1-2), 39-49.
57. Vandecandelaere, N., Rey, C., & Drouet, C. (2012). Biomimetic apatite-based biomaterials: on the critical impact of synthesis and post-synthesis parameters. *Journal of Materials Science: Materials in Medicine*, *23*(11), 2593-2606.
58. Van der Houwen, J. A., Cressey, G., Cressey, B. A., & Valsami-Jones, E. (2003). The effect of organic ligands on the crystallinity of calcium phosphate. Journal of Crystal Growth, 249(3-4), 572-583.
59. Viguet-Carrin, S., Garnero, P., & Delmas, P. D. (2006). The role of collagen in bone strength. *Osteoporosis international*, *17*(3), 319-336.
60. Watt, J. C. (1923). The behavior of calcium phosphate and calcium carbonate (bone salts) precipitated in various media, with applications to bone formation. *The Biological Bulletin*, *44*(6), 280-316.
61. Wopenka, B. and Pasteris, J. (2005). A mineralogical perspective on the apatite in bone. *Materials Science and Engineering: C*, 25(2), pp.131-143.
62. Xie, B., & Nancollas, G. H. (2010). How to control the size and morphology of apatite nanocrystals in bone. *Proceedings of the National Academy of Sciences*, *107*(52), 22369-22370.

Appendix A Unbuffered run – pH data

Time (hr)	Scarb - pH 6.87	S no add - pH 9	S no add - pH 8	S no add - pH 7	S no add - pH 6	S no add - pH 5
-1	**6,87**	**9**	**8**	**7**	**6**	**5**
0	7,07	5,27	5,03	4,8	4,53	4,34
1	7,01	5,82	5,08	4,55	4,4	3,98
2	6,99	5,94	5,21	4,47	4,29	3,83
3	7,30	6,02	5,24	4,6	4,29	3,76
4	7,45	5,99	5,33	4,65	4,2	3,78
23	7,95	5,55	5,6	5,16	4,36	3,76
24	7,66	5,77	5,63	4,88	4,53	3,7
25	7,61	5,88	5,53	4,82	4,5	3,65
26	7,54	5,99	5,6	4,69	4,33	3,74
27	7,54	6,02	5,63	4,81	4,27	3,74
47	7,39	6,37	5,71	4,95	4,42	3,95
48	7,4	6,27	5,66	4,7	4,27	4,1
49	7,39	6,37	5,58	4,82	4,19	4,13
50	7,43	6,3	5,61	4,65	4,22	3,99
51	7,49	6,2	5,6	4,6	4,2	3,97
119	7,75	6,03	5,55	4,78	4,1	4,15
120	7,77	5,97	5,59	4,76	4,21	4,09
121	7,71	5,99	5,54	4,76	4,22	4,06
122	7,64	5,96	5,57	4,83	4,21	4,05
123	7,91	5,81	5,56	4,7	4,12	3,92
144	7,5	6,05	5,73	4,78	4,28	4,09
145	7,64	6,05	5,68	4,82	4,23	3,99
146	7,8	5,97	5,71	4,81	4,2	3,99
147	8,14	5,99	5,7	4,75	4,2	3,8
148	8,23	6,07	5,75	4,84	4,17	3,97

Time (hr)	Spy - pH 9	Spy - pH 8	Spy - pH 7	Spy - pH 6	Spy - pH 5	Scit - pH 9	Scit - pH 8	Scit - pH 7	Scit - pH 6	Scit - pH 5
-1	**9**	**8**	**7**	**6**	**5**	**9**	**8**	**7**	**6**	**5**
0	5,42	5,72	5,16	4,62	5,21	7,48	7,93	6,94	6,16	5,2
1	5,97	5,78	4,8	4,32	4,62	8,1	7,91	6,92	6,2	5,26
2	6,07	5,78	4,76	4,31	4,34	8,27	7,91	6,92	6,26	5,26
3	6,14	5,79	4,65	4,32	4,14	8,31	7,91	6,96	6,26	5,26
4	6,15	5,82	4,69	4,25	4,11	8,36	7,91	6,94	6,23	5,26
23	6,21	5,82	4,83	4,24	4,07	7,63	7,88	6,90	6,27	5,3
24	6,26	5,64	4,71	4,22	3,83	8,1	7,9	6,88	6,24	5,25
25	6,3	5,58	4,75	4,24	4,03	8,15	7,92	6,87	6,26	5,28
26	6,31	5,67	4,71	4,2	3,88	8,08	7,92	6,90	6,27	5,25
27	6,31	5,66	4,79	4,09	3,93	7,99	7,85	6,91	6,26	5,26
47	6,15	5,7	4,69	4,22	4,05	7,69	7,88	6,91	6,28	5,28
48	6,31	5,8	4,78	4,48	4,16	7,79	7,9	6,91	6,28	5,25
49	6,32	5,74	4,74	4,24	4,05	7,82	7,9	6,91	6,26	5,26
50	6,32	5,6	4,7	4,31	4,01	7,82	7,9	6,96	6,23	5,25
51	6,29	5,76	4,66	4,31	4,1	7,83	7,91	6,94	6,25	5,26
119	6,37	5,73	4,78	4,45	3,93	7,63	7,86	6,90	6,26	5,25
120	6,54	5,64	4,89	4,19	4,04	7,67	7,9	6,87	6,3	5,29
121	6,64	5,55	4,69	4,2	4,06	7,57	7,91	6,85	6,23	5,27
122	6,63	5,65	4,63	4,28	4,09	7,62	7,91	6,83	6,25	5,29
123	6,63	6,27	4,7	4,3	3,99	7,66	7,92	6,87	6,24	5,28
144	6,49	5,65	4,75	4,26	4,05	7,54	7,89	6,89	6,32	5,34
145	6,45	5,6	4,7	4,32	3,94	7,69	7,89	6,90	6,28	5,32
146	6,46	5,61	4,64	4,27	3,95	7,7	7,9	6,90	6,29	5,29
147	6,46	5,6	4,63	4,24	3,9	7,68	7,88	6,89	6,28	5,3
148	6,45	5,58	4,8	4,18	3,99	7,74	7,92	6,88	6,28	5,32

Where -1 stands for time before mixing the solutions 0.1 M CaCl and 0.12 M Na_3PO_4 solution, therefore initial pH. Time 0 is the time directly upon mixture.

Appendix B: FTIR data

B.1 S no add

B.1.1 pH7

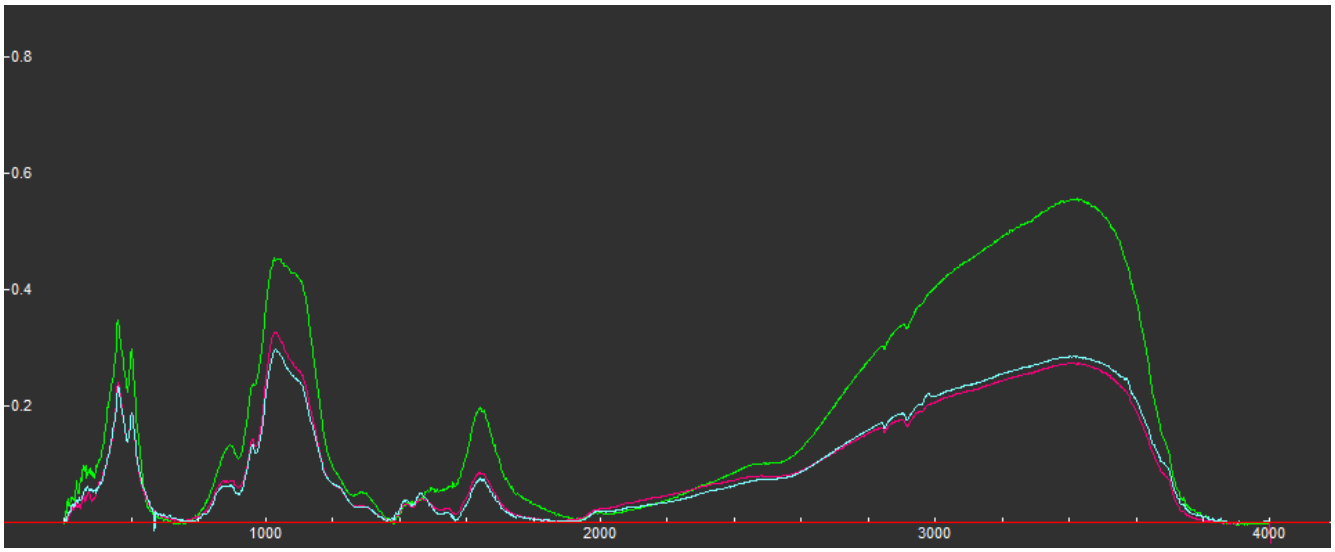

All three days at pH 7, buffered experiment: Green – Day one, Pink – Day two and Blue – Day three

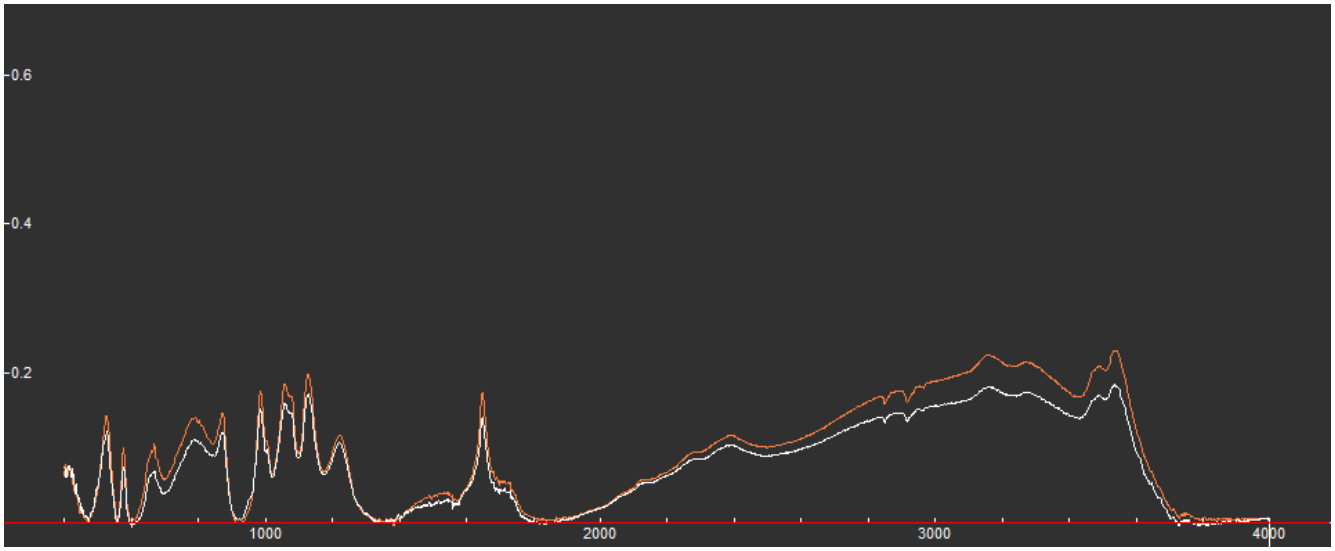

Unbuffered run, pH 7: White – day one and Orange – day six

B.1.2 pH8

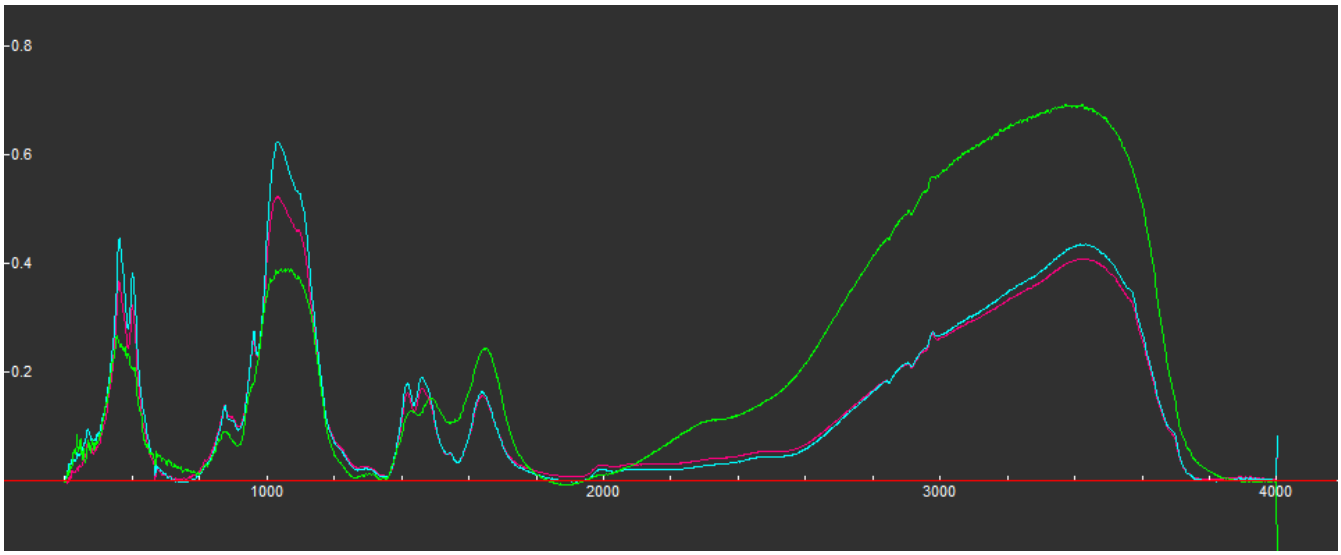

All three days at pH 8, buffered experiment: Green – Day one, Pink – Day two and Blue – Day three

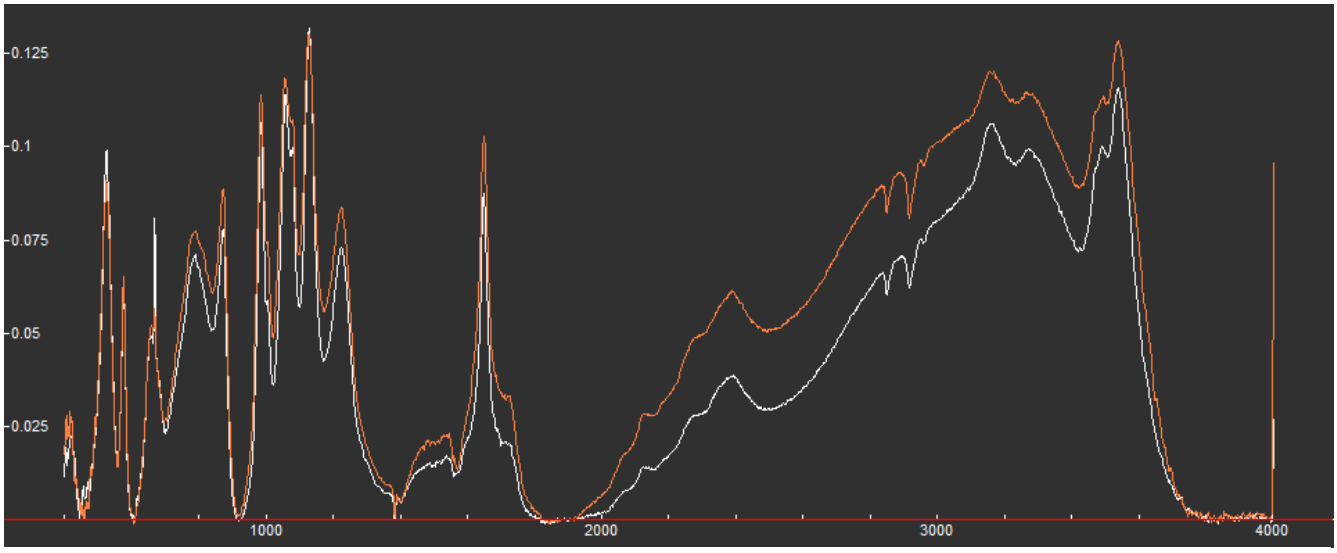

Unbuffered run, pH 8: White – day one and Orange – day six

B.1.3 pH9

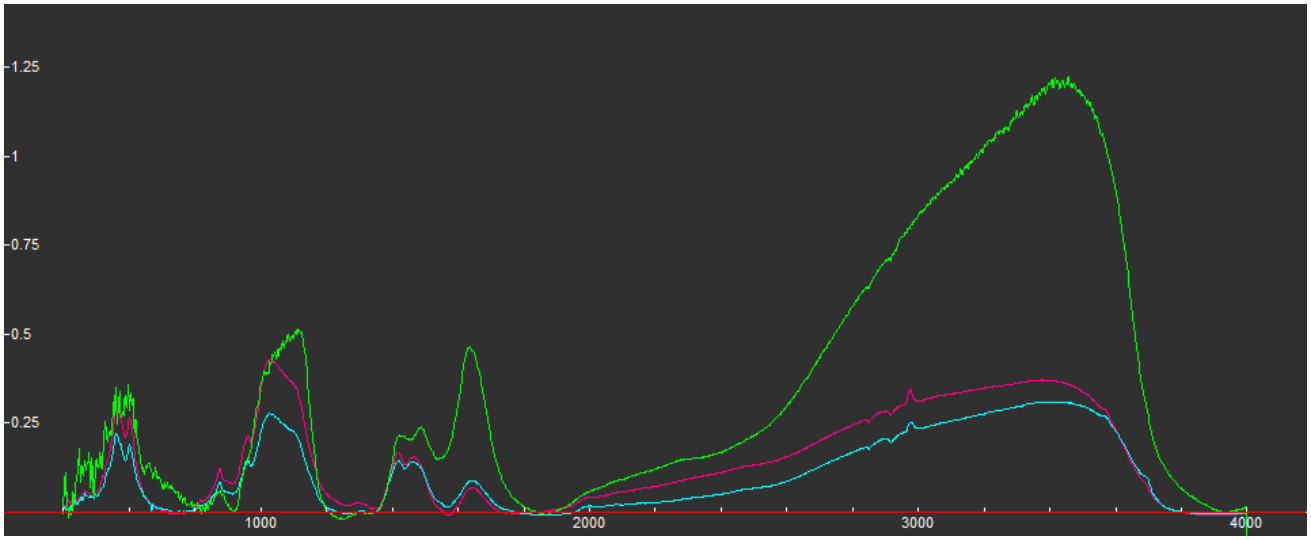

All three days at pH 9, buffered experiment: Green – Day one, Pink – Day two and Blue – Day three

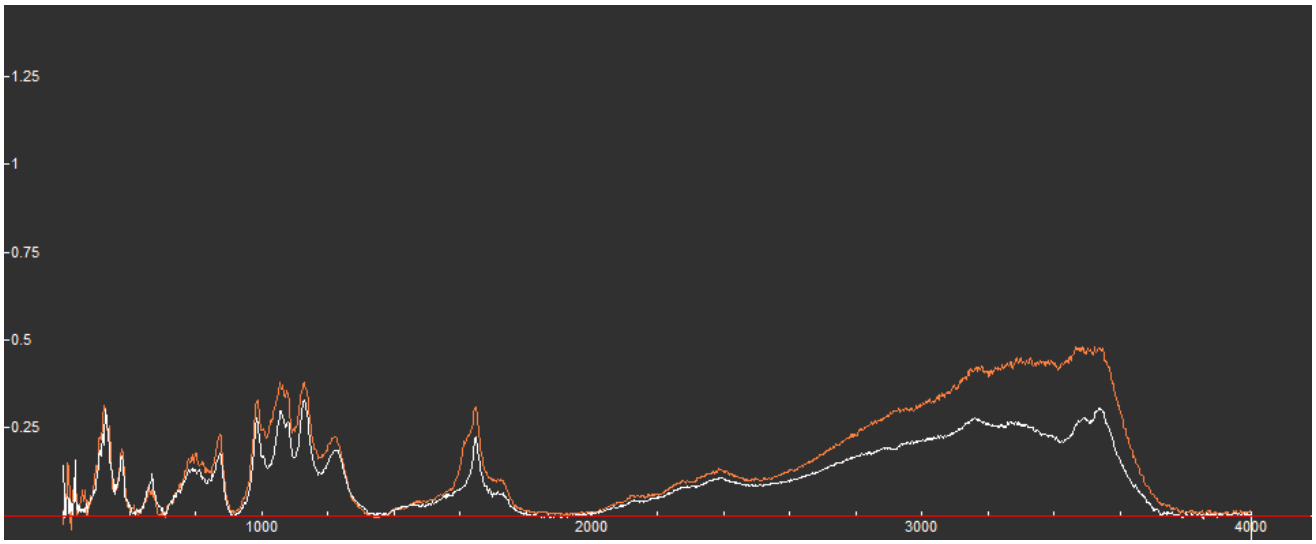

Unbuffered run, pH 9: White – day one and Orange – day six

B.2 Spy

B.2.1 pH7

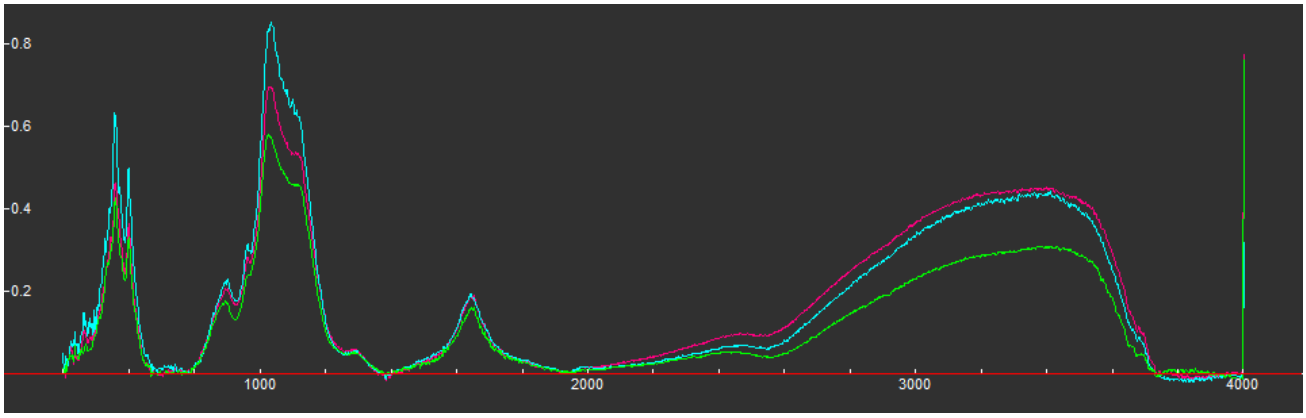

All three days at pH 7, buffered experiment: Green – Day one, Pink – Day two and Blue – Day three

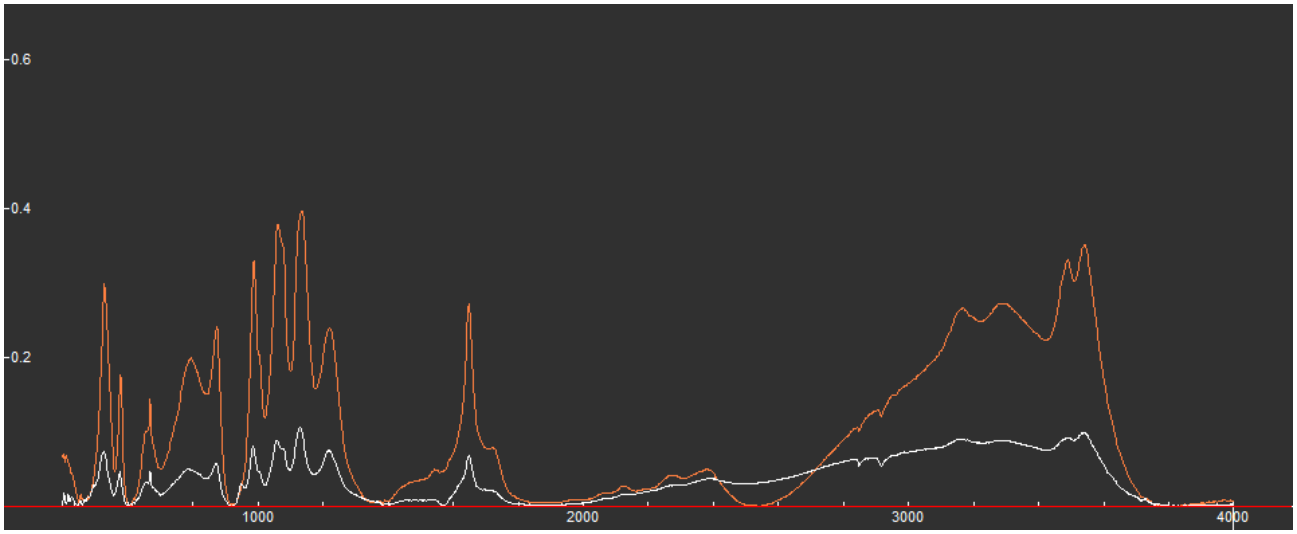

Unbuffered run, pH 7: White – day one and Orange – day six

B.2.2 pH8

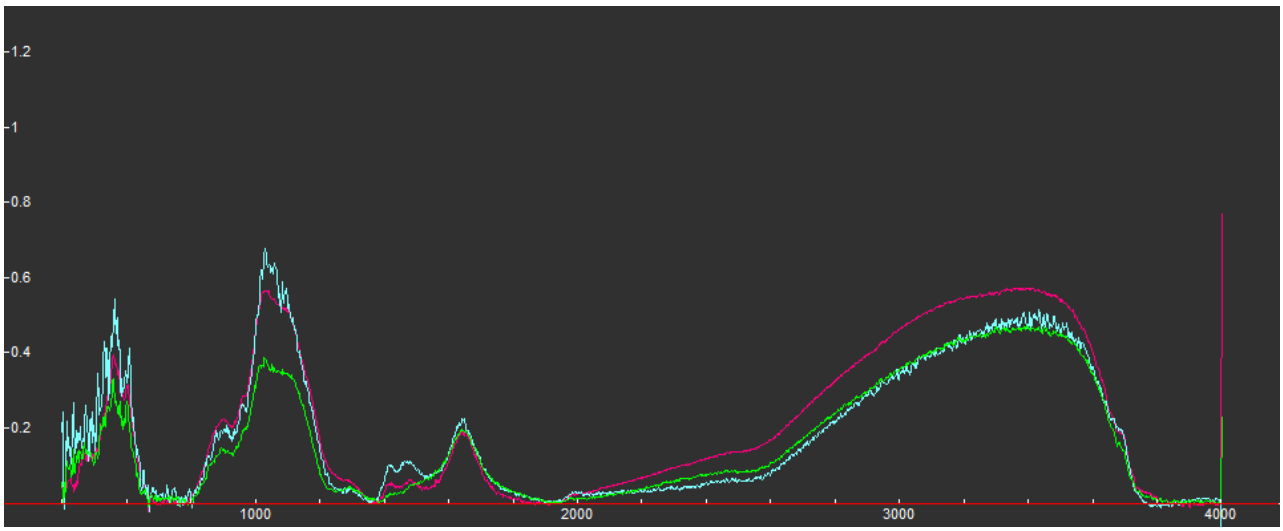

All three days at pH 8, buffered experiment: Green – Day one, Pink – Day two and Blue – Day three

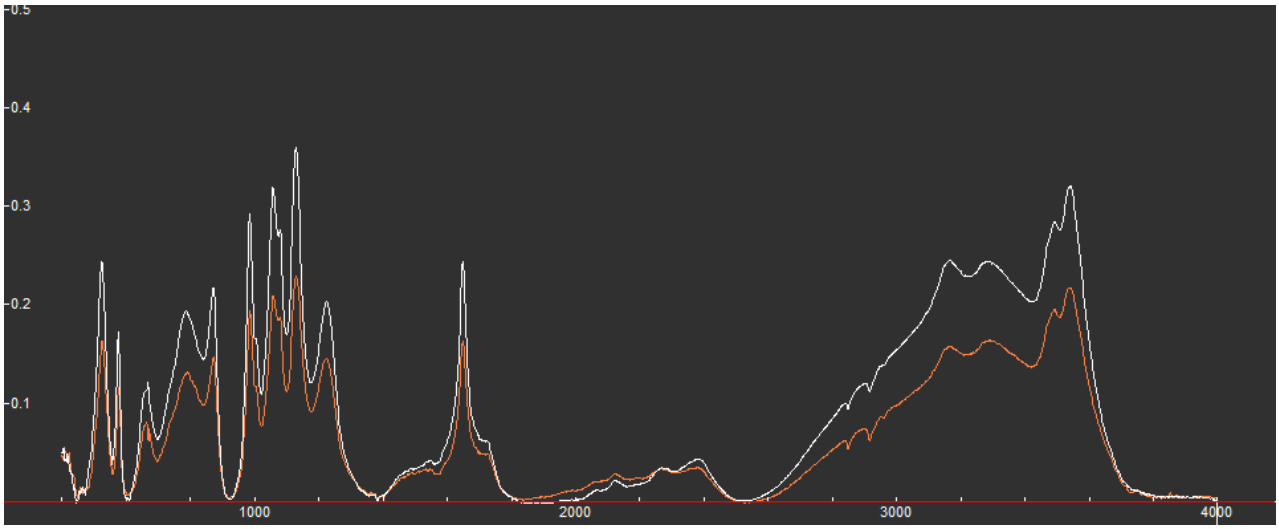

Unbuffered run, pH 8: White – day one and Orange – day six

B.2.3 pH9

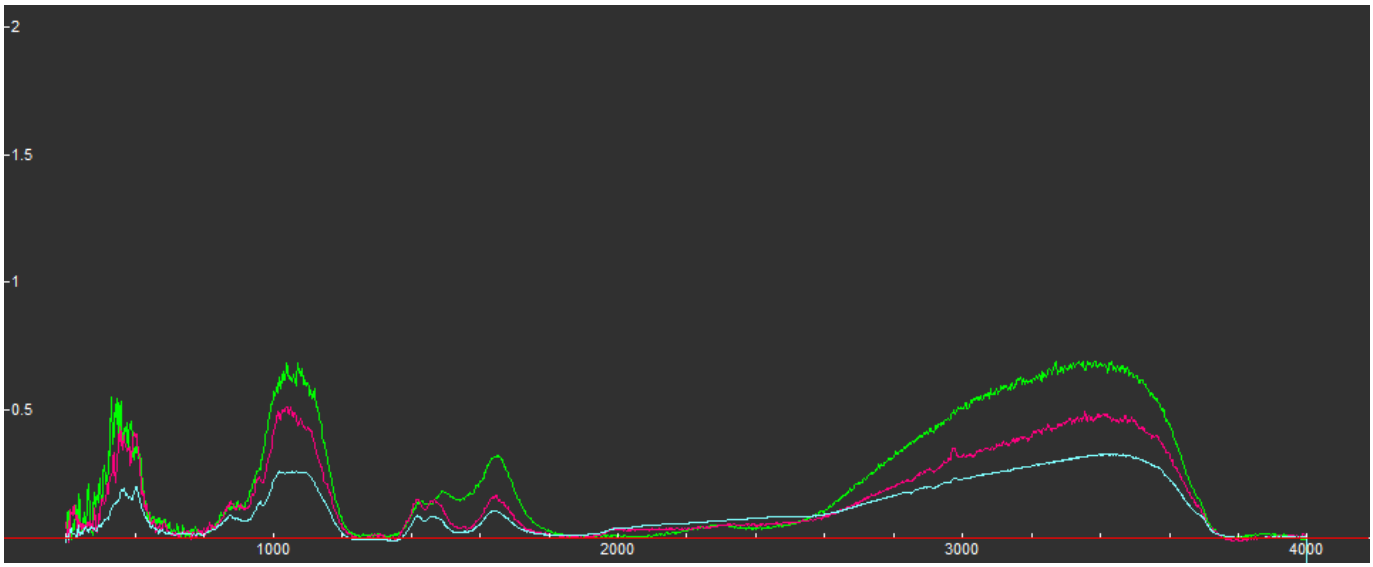

All three days at pH 9, buffered experiment: Green – Day one, Pink – Day two and Blue – Day three

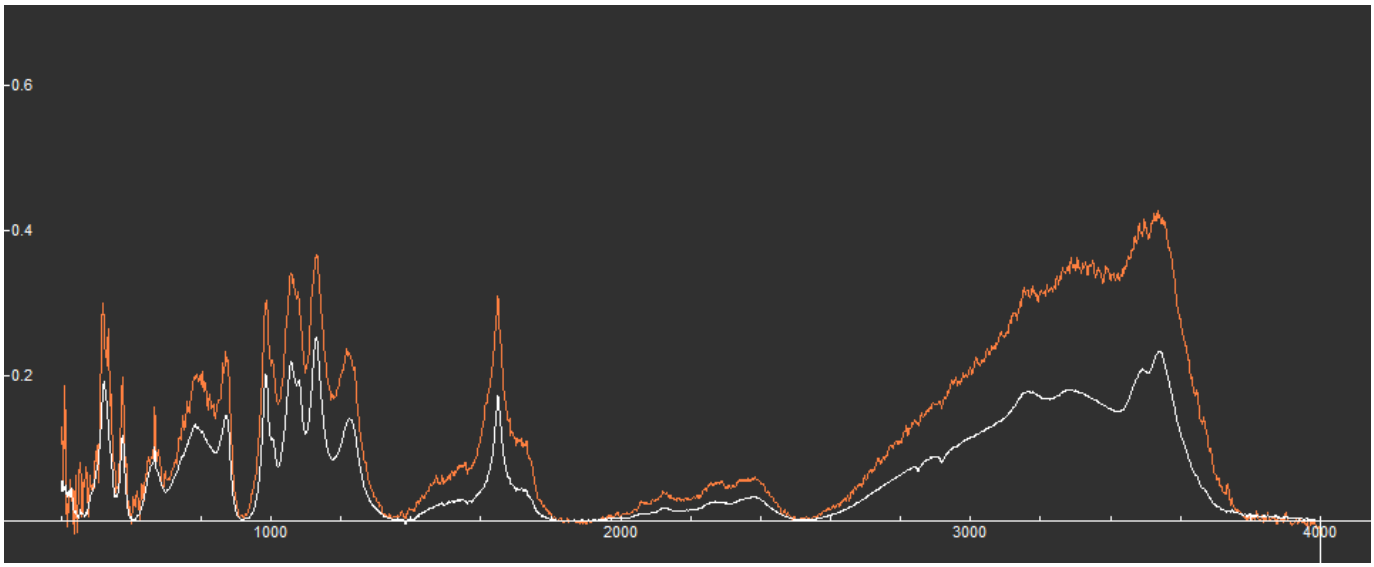

Unbuffered run, pH 9: White – day one and Orange – day six

B.3 Scit

B.3.1 pH7 with 0.001 g citrate

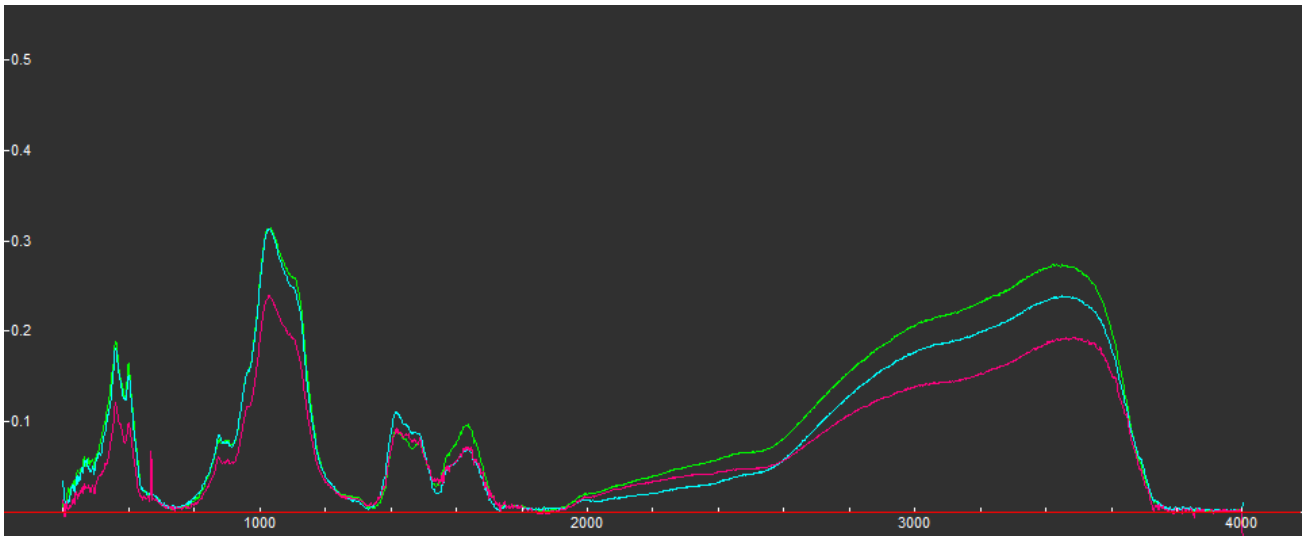

All three days at pH 7, buffered experiment: Green – Day one, Pink – Day two and Blue – Day three

B.3.2 pH 7 with 5.88 g citrate

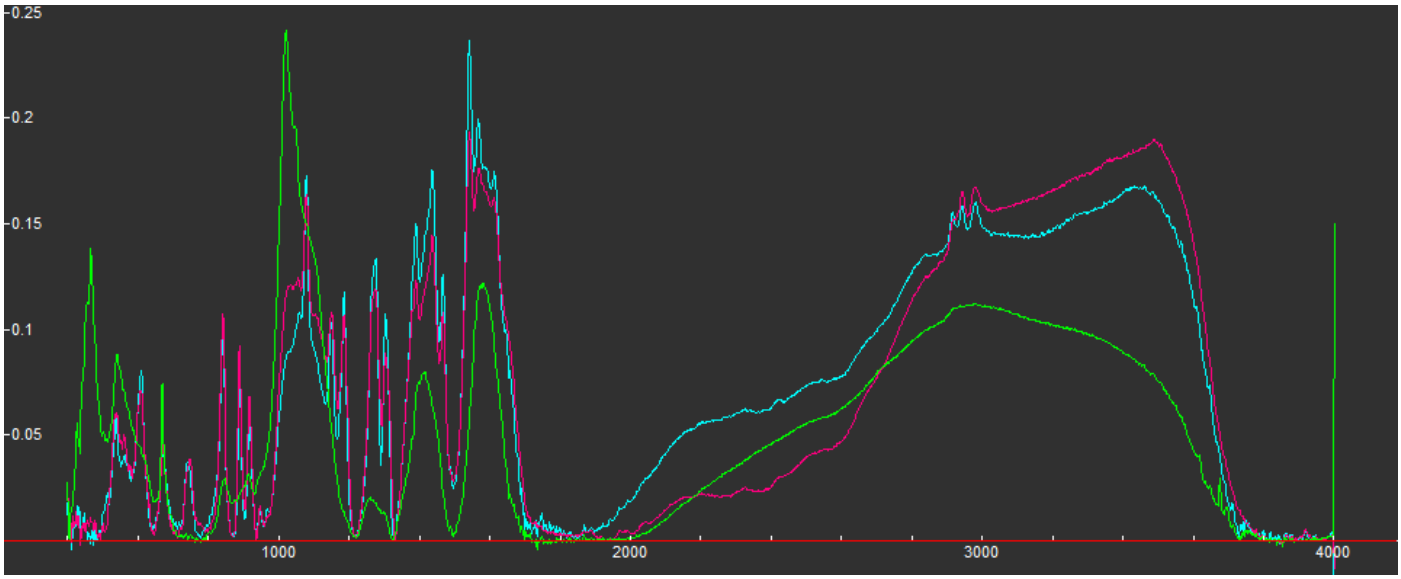

All three days at pH 7, buffered experiment: Green – Day one, Pink – Day two and Blue – Day three

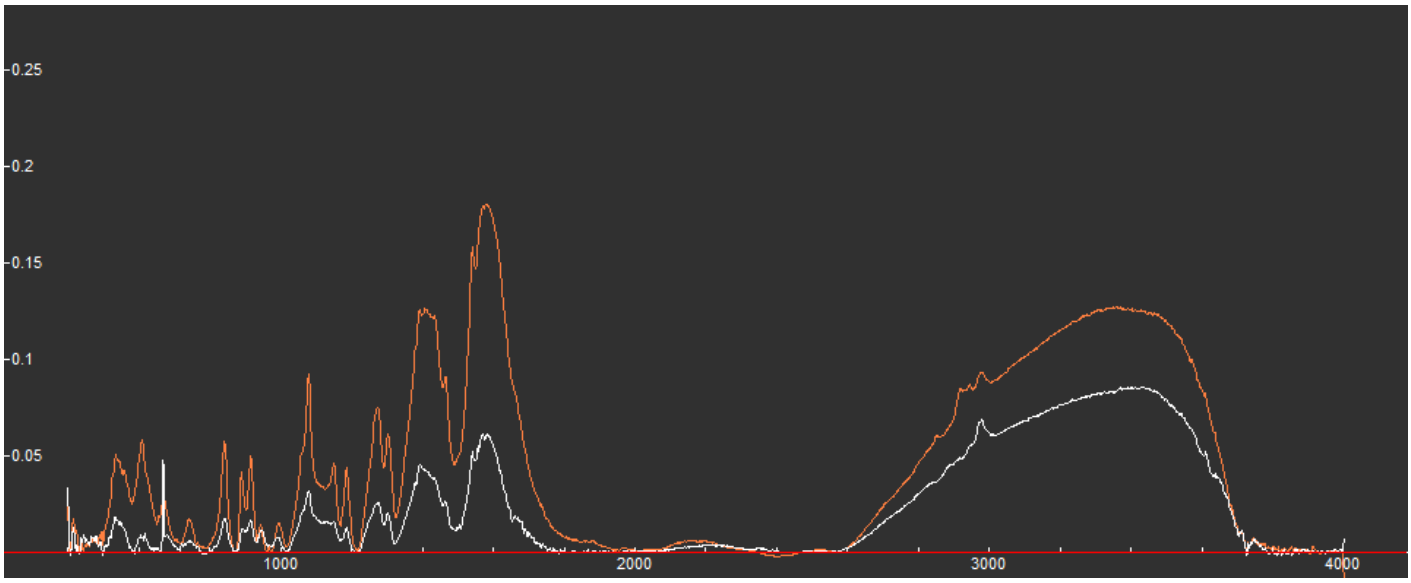

Unbuffered run, pH 7: White – day one and Orange – day six

B.3.3 pH 8 with 5.88 g citrate

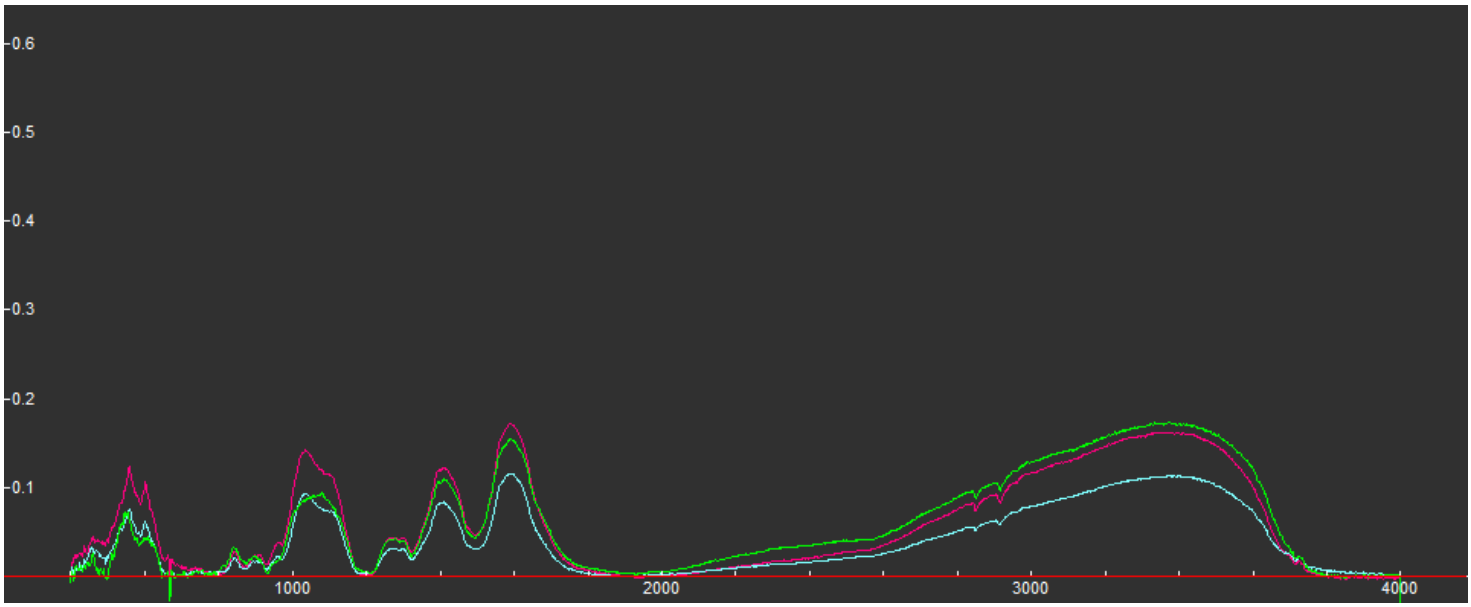

All three days at pH 8, buffered experiment: Green – Day one, Pink – Day two and Blue – Day three

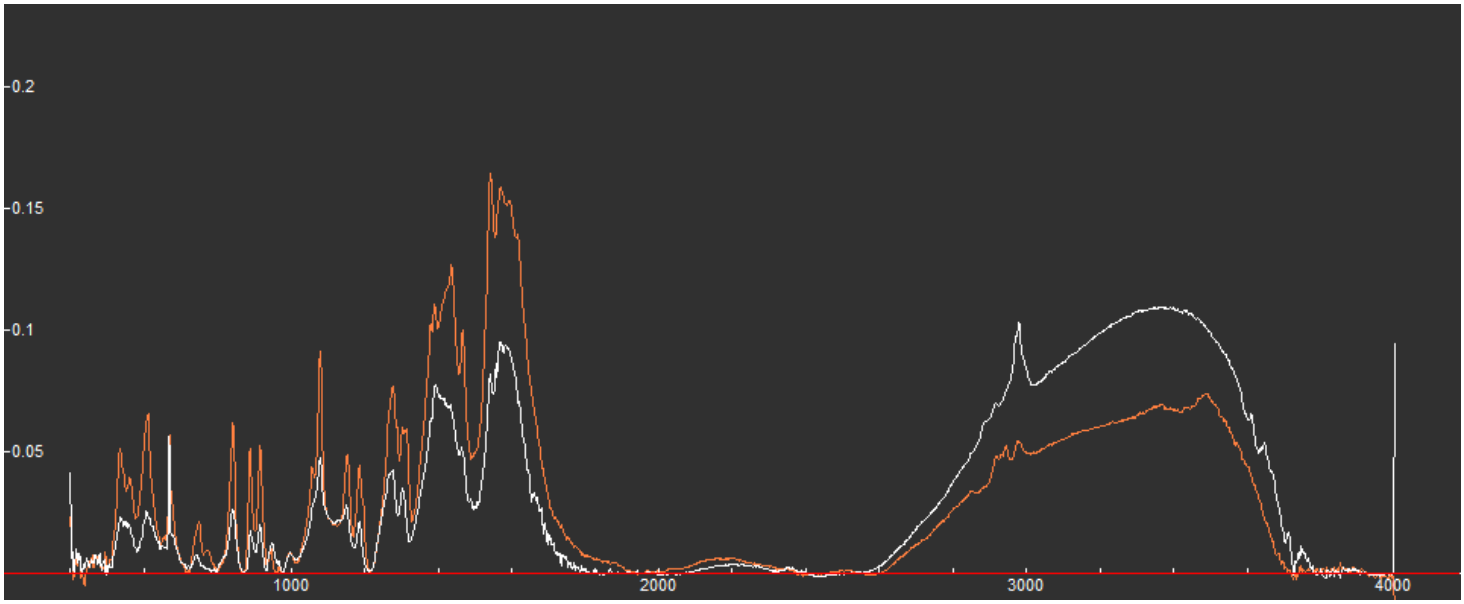

Unbuffered run, pH 8: White – day one and Orange – day six

B.3.4 pH 9 with 5.88 g citrate

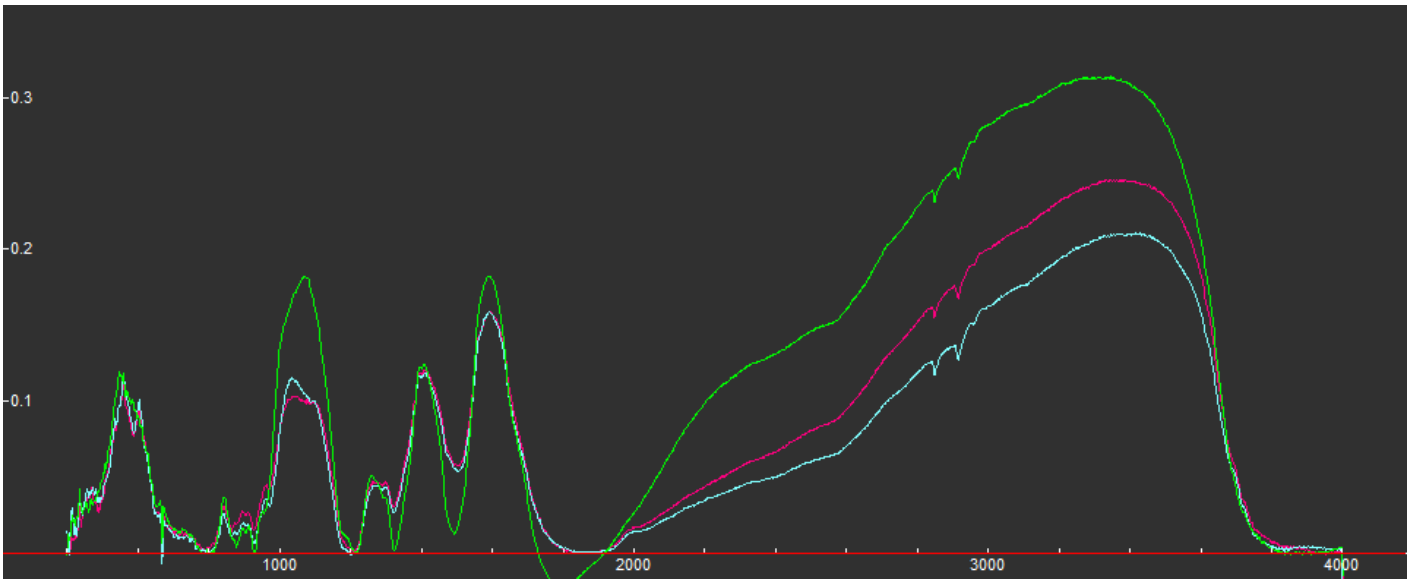

All three days at pH 9, buffered experiment: Green – Day one, Pink – Day two and Blue – Day three

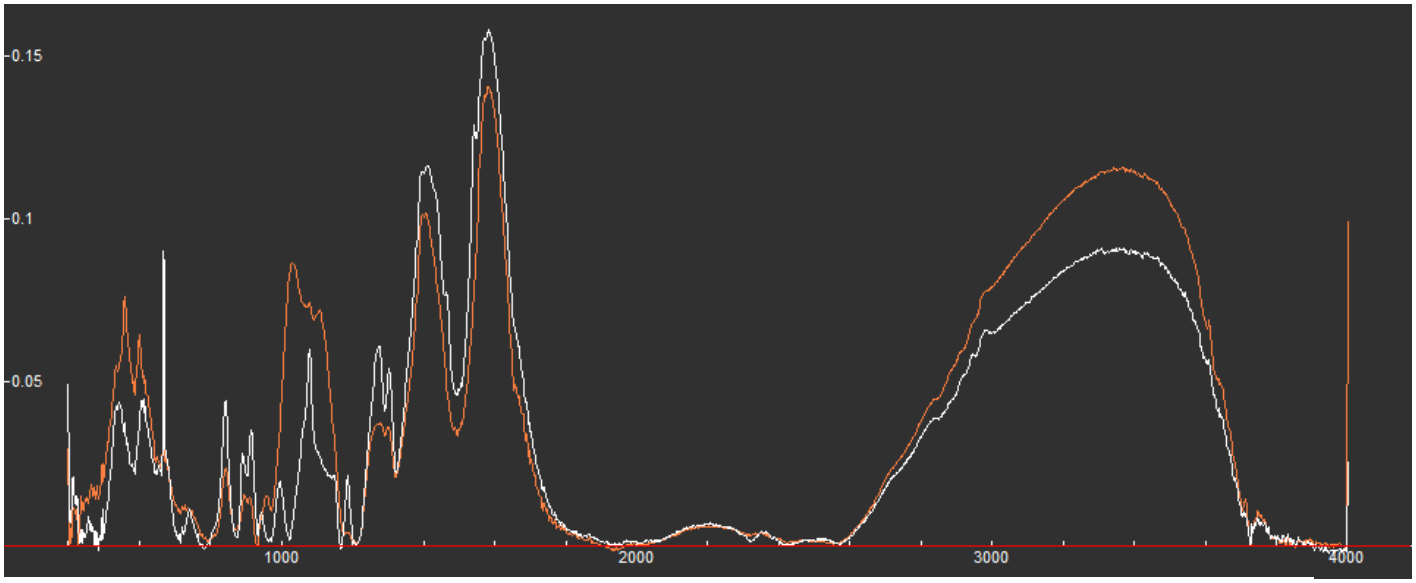

Unbuffered run, pH 8: White – day one and Orange – day six

B.4 Scarb pH 7

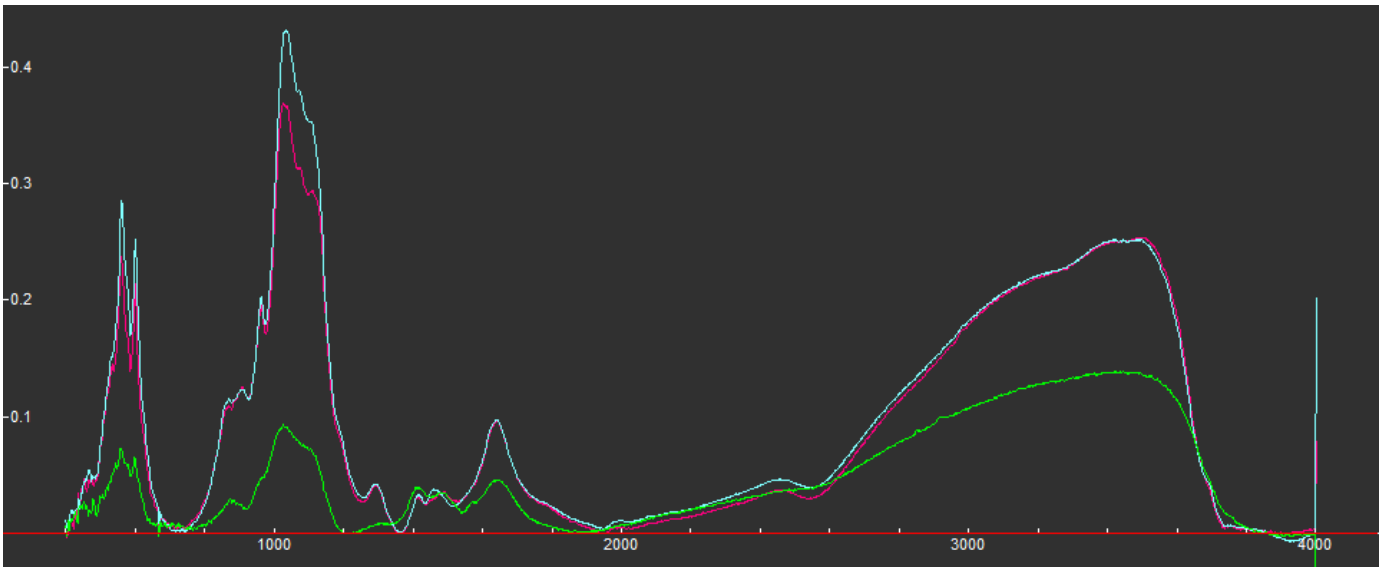

All three days at pH 7, buffered experiment: Green – Day one, Pink – Day two and Blue – Day three

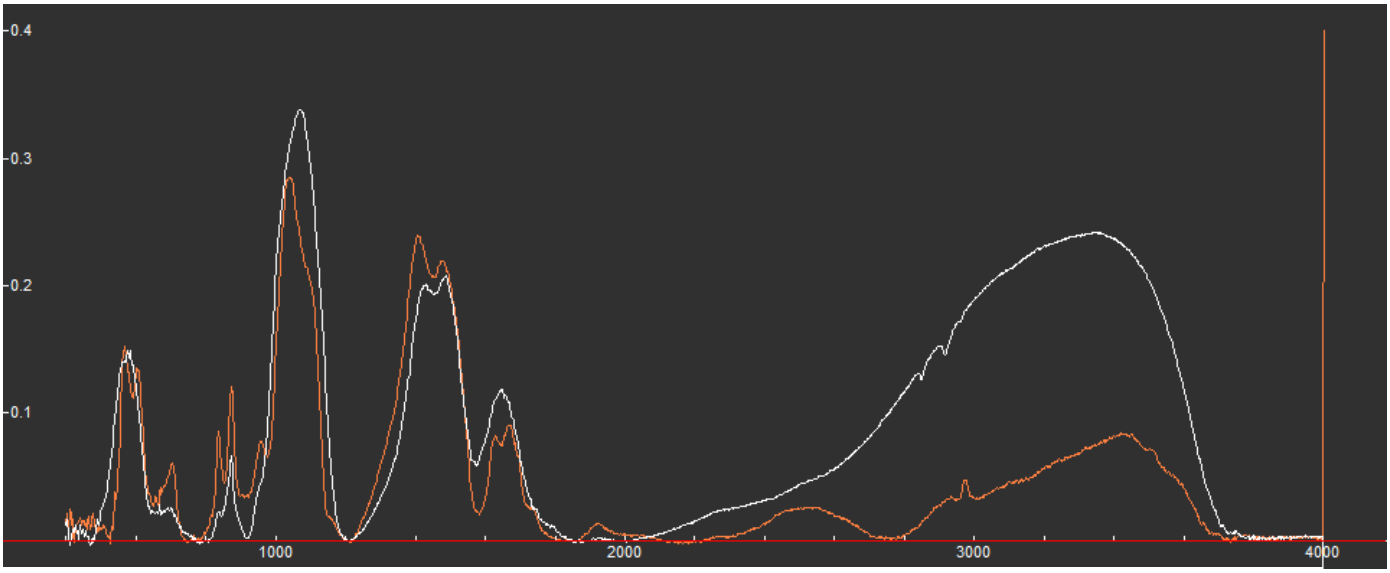

Unbuffered run, pH 8: White – day one and Orange – day six

B.5 All samples day 1 in buffered run

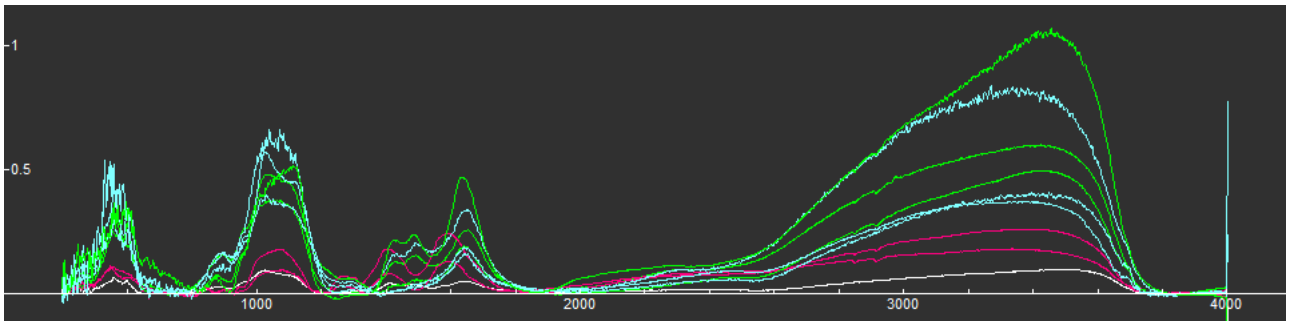

All sample pH levels for day 1, buffered experiment: Green – S no add, Blue – Spy, Red – Scit and White – Scarb

B.6 Scit pH 8 and 9 compared to Citrate spectrum

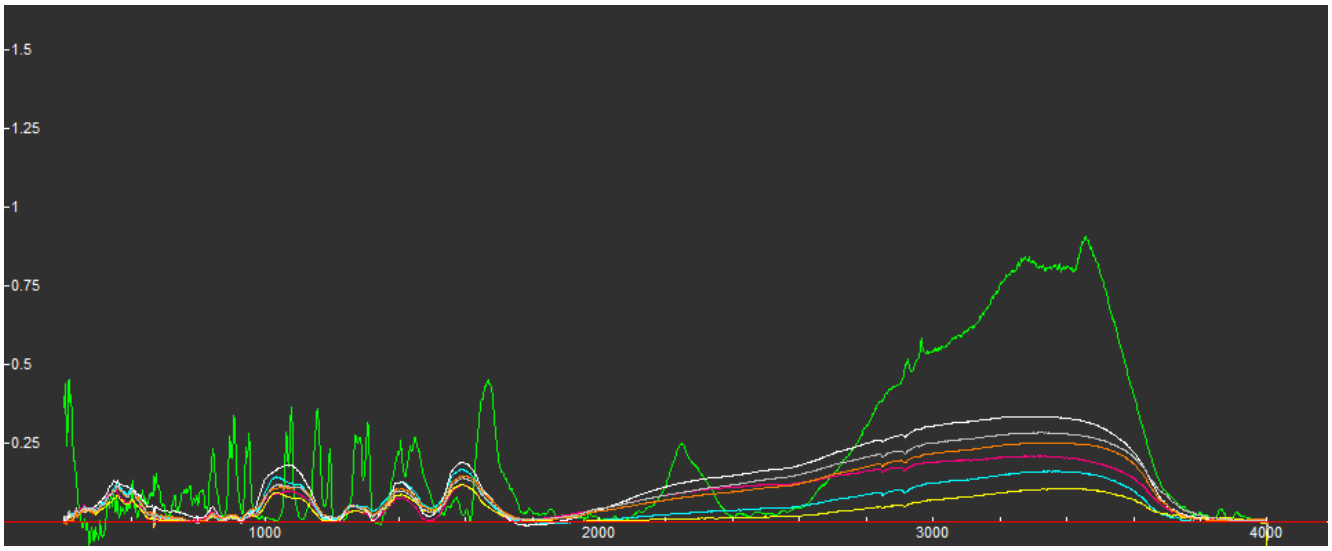

All days of Scit pH8 and 9 against the FTIR Citrate spectra, buffered experiment: Green – Citrate, Other colors – Scit pH 8 and 9 spectra

Appendix C: FTIR band identification tables

Table 1: Peak types assigned to FTIR peak positions (cm^{-1}) where PO_4^{3-} = Phosphate, CO_3^{2-} =carbonate, CA = carbonated apatite, HA = hydroxyapatite and OH = hydroxide. Types based on finds from studies by (1) Rehman and Bonfield, 1997; (2) Drouet, 2013; (3) Martinez-Huitle et al, 2013; (4) Boudia, 2018; (5) Sauer and Wuthier,1988; (6) Mroz et al., 2010 (7) Maréchal (2011)

C.1 $S_{no\ add}$

C.1.1 pH 7

S no add– pH 7			
Day 1	**Day 2**	**Day 3**	**Peak type**
467	471	467	$V_2PO_4^{3-}$ (1)
558	553	562	$V_4PO_4^{3-}$ CA + HA/OCP (1,6)
601	603	601	$V_4PO_4^{3-}$ O-P-O bending HA (1,2,4,6); H_2O molecule (7)
896	871	880	HPO_4^{2-} mode (2)
959	960	960	$V_1PO_4^{3-}$ P-O stretching CA + OCP (1,2,4,6)
1036	1028	1020	$V_3PO_4^{3-}$ OCP (1,5,6)
1106	1104	1102	$V_3PO_4^{3-}$ HA (1,5)
-	1214	1218	HPO_4^{2-} in plane bending (4)
1284	1296	1305	
1422	1412	1412	V_3CO_3 OCP (2,6)
1495	1466	1466	V_3CO_3 CA + OCP (2,6)
-	1548	1532	V_3CO_3 (2)
1635	1635	1647	V_3CO_3 CA + HA (2); v_2H_2O bending mode (7)
1994	1990	1977	
2460	2427	2456	
>2600	>2600	>2600	OH- stretching (1,2,3,7)

C.1.2 pH 8

S no add– pH 8			
Day 1	**Day 2**	**Day 3**	**Peak type**
-	471	463	$v_2PO_4^{3-}$ (1)
553	562	558	$v_4PO_4^{3-}$ CA + HA/OCP (1, 6)
603	603	595	$v_4PO_4^{3-}$ O-P-O bending CA + HA (1,2,4, 6); H_2O molecule (7)
875	875	867	$v_2PO_4^{3-}$ CA (1); HPO_4 bearing apatite P-OH stretching (2,3), OCP (6)
-	892	896	
950	959	960	$V_1PO_4^{3-}$ P-O stretching CA + OCP (1,2,4,6)
1053	1026	1030	$V_3PO_4^{3-}$ HA/ OCP (1,4,5,6)
-	1098	1098	$V_3PO_4^{3-}$ P-O stretch HA (1,4,5)
-	1214	1218	
-	1288	1288	
1305	-	-	
1428	1416	1416	V_3CO_3 HA (2,6)
1486	1462	1457	V_3CO_3 CA (2)
-	1544	1537	V_3CO_3 (2)
1650	1635	1635	V_3CO_3 CA + HA (2); v_2H_2O bending mode (7)
-	1990	1998	
2295	-	-	
>2500	>2600	>2600	OH- stretching (1,2,3,7)

C.1.3 pH 9

S no add– pH 9			
Day 1	**Day 2**	**Day 3**	**Peak type**
-	463	471	$v_2PO_4^{3-}$ (1)
562	558	562	$V_4PO_4^{3-}$ CA + HA/OCP (1,6)
599	599	599	$V_4PO_4^{3-}$ CA (1); H_2O molecule (7)
661	-	-	
-	813	-	
875	871	875	$v_2PO_4^{3-}$ CA (1), HPO_4 bearing apatite P-OH stretching (2), $V_2CO_3^{2-}$ out of plane bending (8)
958	962	962	$V_1PO_4^{3-}$ P-O stretching CA + OCP (1,2,4,6)
999	-	-	$V_3PO_4^{3-}$ (1)
1028	1028	1016	$V_3PO_4^{3-}$ HA/ OCP (1,4,5)
1119	1098	1102	$V_3PO_4^{3-}$ HA (1,5)
-	1284	-	
1428	1416	1412	$V_3CO_3^{2-}$ (2)
1490	1470	1470	$V_3CO_3^{2-}$ CA + HA (2,6)
1635	1643	1631	$V_3CO_3^{2-}$ CA + HA (2); v_2H_2O bending mode (7)
-	1983	1994	
2271	-	-	
>2500	>2500	>2500	OH- stretching (1,2,3,7)
-	2972	-	

C.2 S_{carb} pH 7

Scarb – pH 7			
Day 1	**Day 2**	**Day 3**	**Peak type**
-	-	463	
		525	
553	558	558	$V_4PO_4^{3-}$ CA + HA/ OCP (1,4,6)
593	595	599	
871	863	863	B-type V_2CO_3 CA + OCP (1,2,6)
-	903	903	
958	962	962	$V_1PO_4^{3-}$ P-O stretching CA + OCP (1,2,6)
1024	1028	1032	$V_3PO_4^{3-}$ OCP (1,4,6)
-	1074	1069	$V_3PO_4^{3-}$ (1,4)
1119	1111	1102	$V_3PO_4^{3-}$ P-O stretch HA (1,4,5)
-	1288	1288	
1416	1417	1419	V_3CO_2 HA(1,2,6)
1482	1474	1462	V_3CO_2 CA + OCP (2,6)
1631	1639	1635	V_2H_2O bending (7)
-	1990	1996	
2481	2465	2444	
>2600	>2600	>2600	OH^- stretching (1,2,3,7)

C.3 S_{py}

C.3.1 pH 7

Spy – pH 7			
Day 1	**Day 2**	**Day 3**	**Peak type**
-	417	-	
-	456	467	
553	558	545	$v_4PO_4^{3-}$ CA + HA/OCP (1,6)
599	599	595	$v_4PO_4^{3-}$ CA (1); water molecule (7)
882	882	882	HPO_4^{2-} mode (2)
954	958	958	$v_1PO_4^{3-}$ strong symmetrical stretch CA + HA (1,2,3)
1032	1032	1032	$v_3PO_4^{3-}$ OCP (1,4,5,6)
1119	1102	1111	$v_3PO_4^{3-}$ HA (1,5)
1284	1280	1292	
1428	1428	1428	$V_3CO_3^{2-}$ HA (2,6)
1490	1470	1470	$V_3CO_3^{2-}$ CA (2)
1650	1643	1639	V_2H_2O bending (7)
2432	2456	2456	
>2500	>2500	>2500	OH- stretching (1,2,3,7)

C.3.2 pH 8

Spy – pH 8			
Day 1	**Day 2**	**Day 3**	**Peak type**
463	467	-	
553	553	570	$v_4PO_4^{3-}$ O-P-O bending CA (1,2)
603	593	602	$v_4PO_4^{3-}$ O-P-O bending CA, HA (1,2,4,6); water molecule (7)
896	892	908	
958	958	958	$V_1PO_4^{3-}$ strong symmetrical stretch (1,2,3,5); carbonated apatite (5)
1024	1032	1024	$v_3PO_4^{3-}$ OCP (1,4,6)
1115	1107	1094	$v_3PO_4^{3-}$ HA (1,5)
1280	1280	1301	
1416	1416	1416	V_3CO_3 HA (2,6)
-	1474	1474	V_3CO_3 CA (2)
1643	1643	1643	V_3CO_3 CA + HA (2); v_2H_2O bending (7)
-	-	1982	
2469	2477	2456	
>2600	>2600	>2600	OH- stretching (1,2,3,7)

C.3.3 pH 9

Spy – pH 9			
Day 1	**Day 2**	**Day 3**	**Peak type**
553	558	566	$v_2PO_4^{3-}$ CA + HA/OCP (1,6)
607	599	603	$v_4PO_4^{3-}$ O-P-O bending CA + HA (1,2,6), water molecule (7)
896	875	875	HPO_4^{2-} mode (2)
942	952	954	$V_1PO_4^{3-}$ strong symmetrical stretch (1,2,3,5); carbonated apatite (5)
-	1016	1016	$v_3PO_4^{3-}$ P-O stretching HA (1,4,6)
1057	-	-	$v_3PO_4^{3-}$ P-O stretching (1,4)
-	1111	1090	$v_3PO_4^{3-}$ P-O stretching HA (1,4,5)
-	1305	-	
1428	1412	1412	V_3CO_3 HA (2,6)
1495	1457	1457	V_3CO_3 CA (2)
1651	1635	1643	V_3CO_3 CA + HA (2), v_2H_2O bending (7)
-	1982	2002	
2279	-	-	
>2600	>2500	>2600	OH^- stretching (1,2,3,7)
-	2976	-	OH^- stretching of HPO_4^{2-} species (4)

C.4 S_{cit}

C.4.1 pH 7 – 5.88 g

Scit– pH 7 – 5.88 g citrate			
Day 1	**Day 2**	**Day 3**	**Peak type**
436	-	-	
-	-	529	$v_4PO_4^{3-}$ (1,2)
541	541	558	$v_4PO_4^{3-}$ CA (1)
-	562	-	$v_4PO_4^{3-}$ O-P-O bending CA + HA (1,2,4,6)
-	603	609	$v_4PO_4^{3-}$ O-P-O bending CA + HA (1,2,4,6), water molecule (7)
669	665	669	
-	743	739	
846	842	838	
-	884	880	
908	917	908	P-O(H) stretching (4)
-	941	941	
-	970	-	
1020	1024	-	$v_3PO_4^{3-}$ HA (1,4)
1040	1050	1045	$v_3PO_4^{3-}$ P-O stretching HA (1,2,4)
1082	1078	1078	$v_3PO_4^{3-}$ P-O stretching HA (1,4)
-	-	1107	$v_3PO_4^{3-}$ HA (1,5)
-	1148	1148	$v_3PO_4^{3-}$ (1)
-	1181	1181	
1263	1268	1272	
1305	1296	1301	
1412	1387	1383	
-	1428	1428	Calcium citrate asymmetrical vibrations of COO^- (3)
-	1466	1466	Calcium citrate asymmetrical vibrations of COO^- (3)
-	1540	1540	Calcium citrate asymmetrical vibrations of COO^- (3)
1581	1565	1566	Calcium citrate asymmetrical vibrations of COO^- (3)
-	1610	1610	V_2H_2O bending (7)
>2000	-	2159	
-	-	2320	
-	2419	2411	
-	-	2502	
-	2832	2832	
2914	2914	2914	OH^- stretching of HPO_4^{2-} species (4)
-	2939	2947	
-	2981	2974	
-	3439	3484	OH^- stretching (1,2,3,7)

C.4.2 pH 7 – 0.01 g

Scit– pH 7 – 0.001 g citrate			
Day 1	**Day 2**	**Day 3**	**Peak type**
463	463	458	
562	558	558	$v_4PO_4^{3-}$ O-P-O bending CA + HA (1,2,6)
599	595	603	$v_4PO_4^{3-}$ O-P-O bending CA + HA (1,2,6); water molecule (7)
871	875	875	HPO_4 bearing apatite P-OH stretching CA (2)
954	958	954	OCP (6)
1024	1024	1024	$v_3PO_4^{3-}$ OCP (1,4,6)
1107	1102	1098	$v_3PO_4^{3-}$ HA (1)
1296	1280	1296	P-OH in plane bending (4)
1412	1412	1420	OCP (6)
1482	1492	1474	Calcium citrate asymmetrical vibrations of COO^- (3)
1635	1635	1639	V_2H_2O bending (7)
1986	1990	1990	
2240	2460	2415	
>2500	>2500	>2500	OH^- stretching (1,2,3,7)

C.4.3 pH 8

Scit – pH 8			
Day 1	**Day 2**	**Day 3**	**Peak type**
463	463	463	
545	558	553	$V_4PO_4^{3-}$ CA + HA (1,2,6)
603	595	595	$V_4PO_4^{3-}$ O-P-O bending CA + HA (1,2,6); water molecule (7)
838	842	846	
892	904	896	HA (6)
941	954	958	OCP (6)
-	1036	1036	$V_3PO_4^{3-}$ P-O stretching OCP (1,4,6)
1078	1107	1102	$V_3PO_4^{3-}$ HA (1)
1276	1255	1251	
-	1296	1292	
1416	1412	1391	
1585	1578	1585	Calcium citrate asymmetrical vibrations due to COO^- (3)
2485	2526	-	
>2600	>2600	>2600	OH^- stretching (1,2,3,7)

C.4.4 pH 9

Scit – pH 9			
Day 1	**Day 2**	**Day 3**	**Peak type**
	471	471	$V_2PO_4^{3-}$ O-P-O bending (1,2)
545	553	553	$V_4PO_4^{3-}$ CA + HA (1,2,6)
-	607	607	$V_4PO_4^{3-}$ CA (1); water molecule (7)
835	843	838	
896	-	896	
908	904	-	
950	958	950	$V_1PO_4^{3-}$ P-O stretching CA + OCP (1,2,4,6)
-	1028	1032	$V_3PO_4^{3-}$ OCP (1,4,5,6)
1069	1098	1090	$V_3PO_4^{3-}$ P-O stretching HA (1,2,4)
1263	1255	1263	
-	1305	1296	
1404	1395	1404	
1581	1594	1589	Calcium citrate asymmetrical vibrations of COO^- (3)
-	1998	1990	
2493	2506	-	
>2600	>2600	>2500	OH^- stretching (1,2,3,7)

Appendix D: Raman data

D.1 $S_{no\ add}$ pH 8

D.1.1 Days 1 to 3 separated

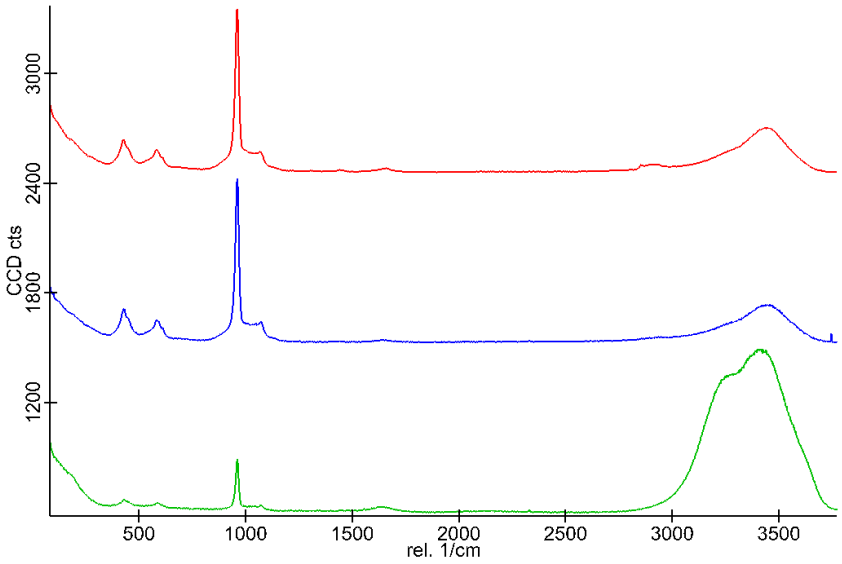

Buffered experiment, red – day 1, blue – day 2 and green – day 3

D.1.2 Days 1 to 3 overlay

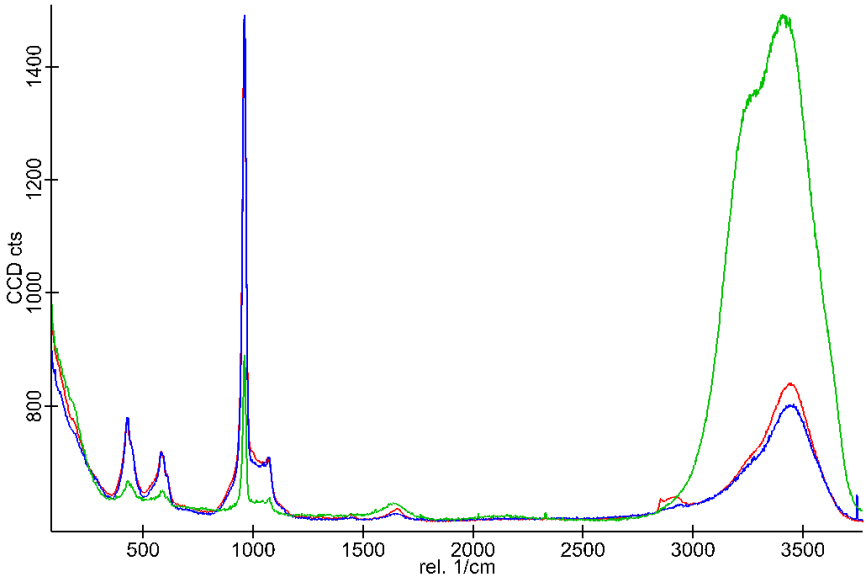

Buffered experiment, red – day 1, blue – day 2 and green – day 3

D.2 S_{py} pH 8

D.2.1 Days 1 to 3 separated

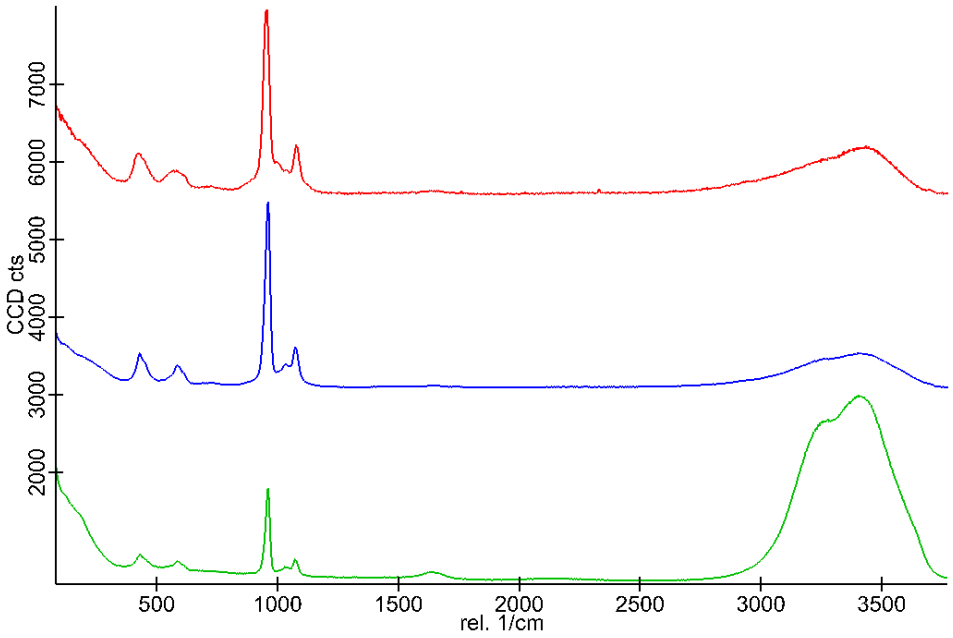

Buffered experiment, red – day 1, blue – day 2 and green – day 3

D.2.2 Days 1 to 3 overlay

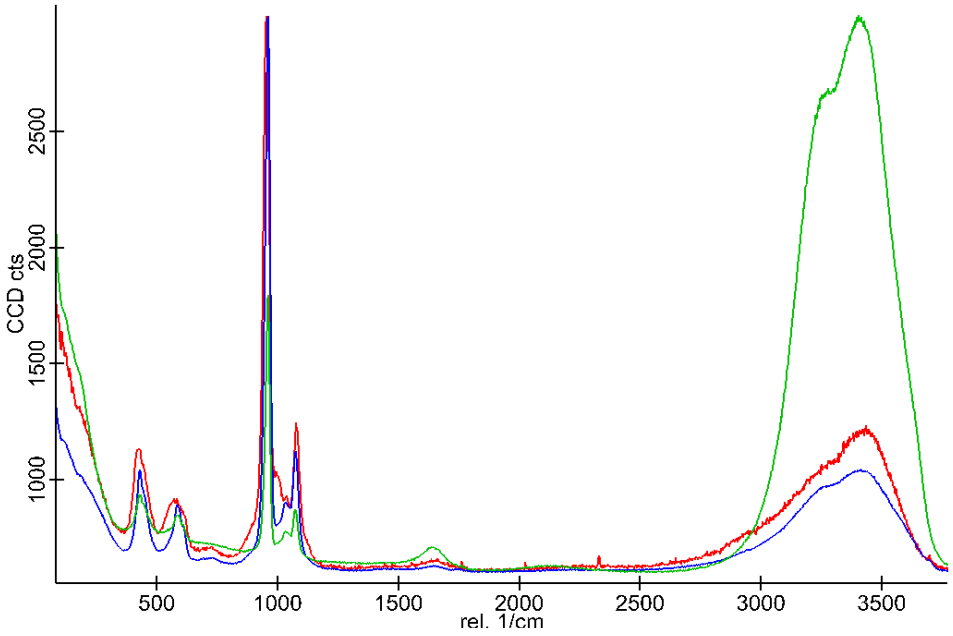

Buffered experiment, red – day 1, blue – day 2 and green – day 3

D.3 S_{py} pH 9

D.3.1 Days 1 to 3 separated

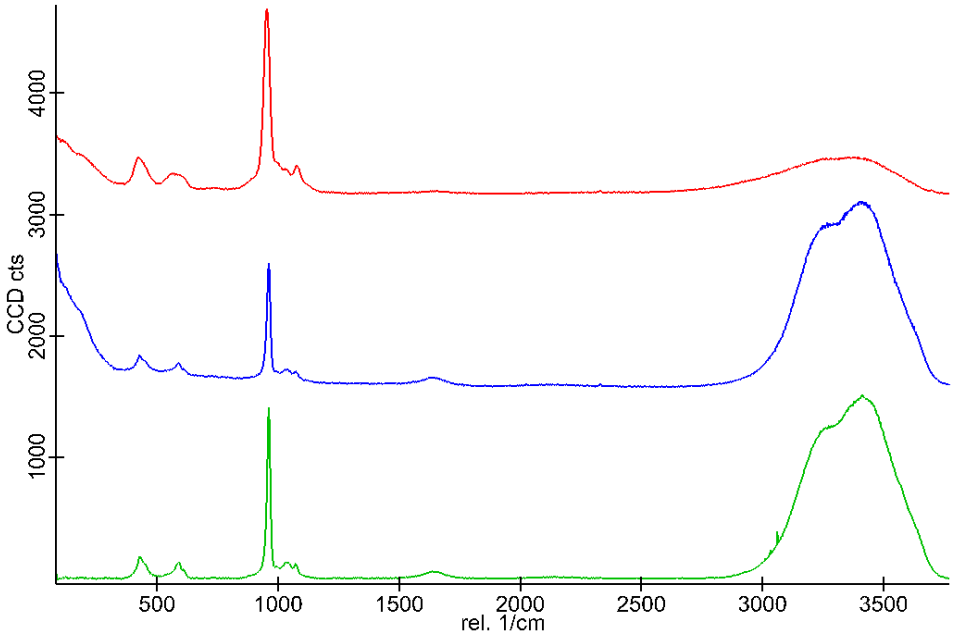

Buffered experiment, red – day 1, blue – day 2 and green – day 3

D.3.2 Days 1 to 3 overlay

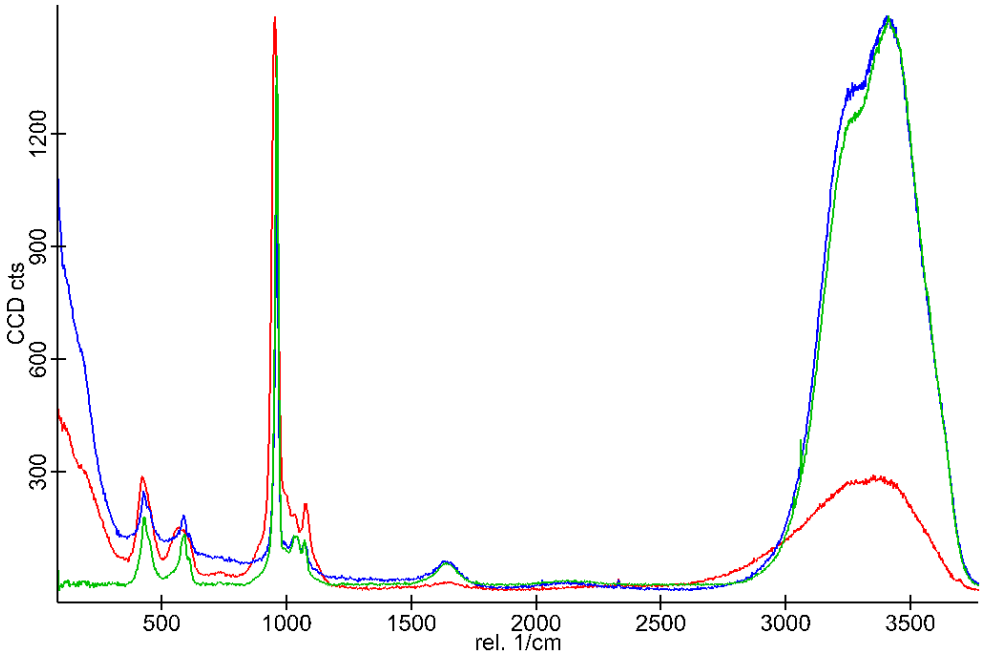

Buffered experiment, red – day 1, blue – day 2 and green – day 3

D.4 S_{cit} pH 7

D.4.1 Days 1 to 3 separated – 0.001 g citrate

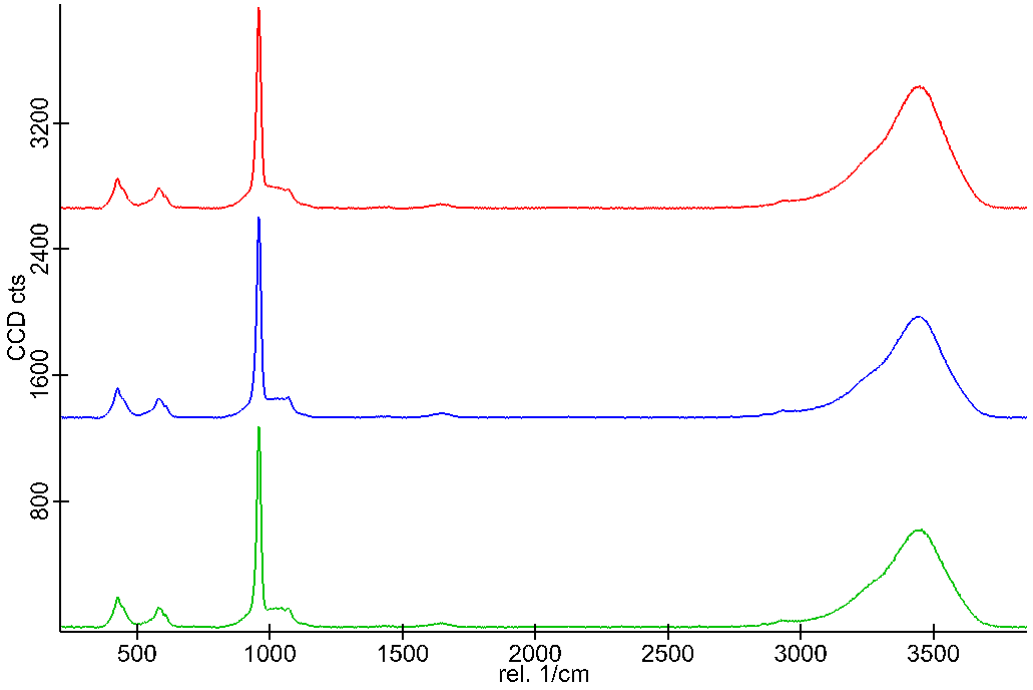

Buffered experiment, red – day 1, blue – day 2 and green – day 3

D. 4.2 Days 1 to 3 overlay – 0.001 g citrate

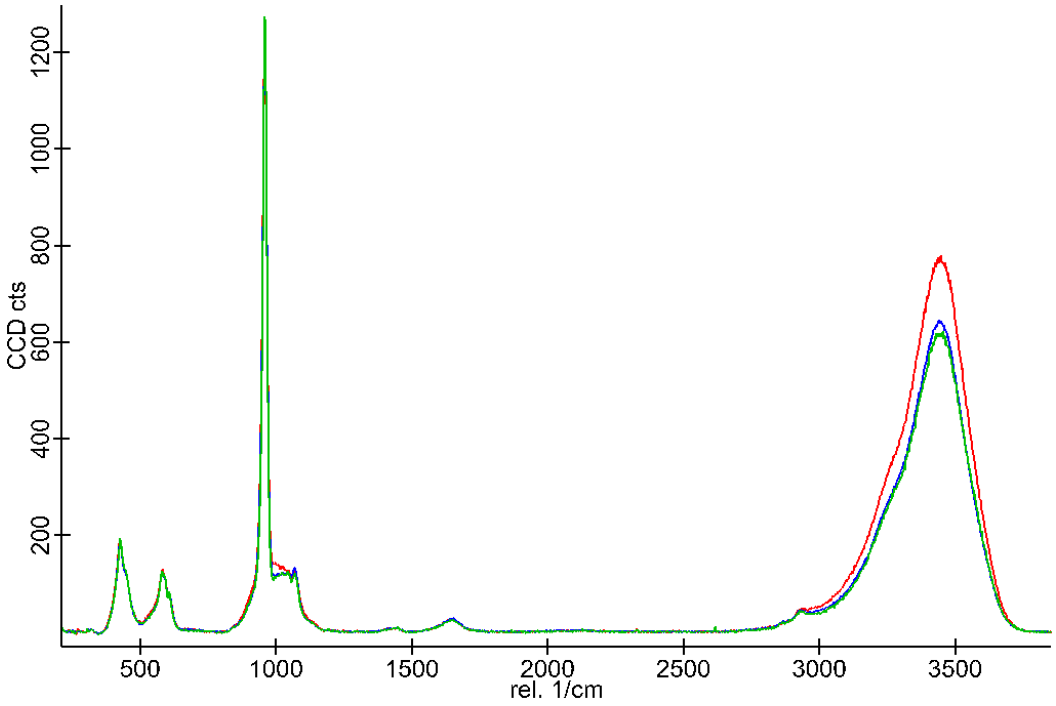

Buffered experiment, red – day 1, blue – day 2 and green – day 3

D.4.3 Days 1 to 3 separated – 5.88 g citrate

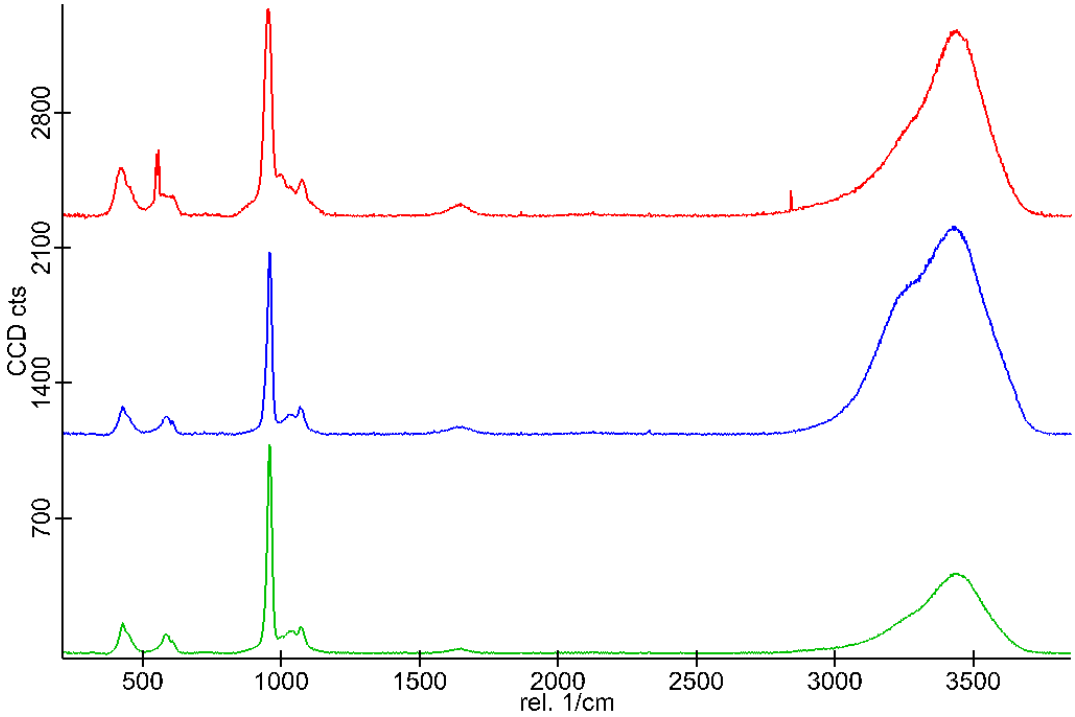

Buffered experiment, red – day 1, blue – day 2 and green – day 3

D.4.4 Days 1 to 3 overlay – 5.88 g citrate

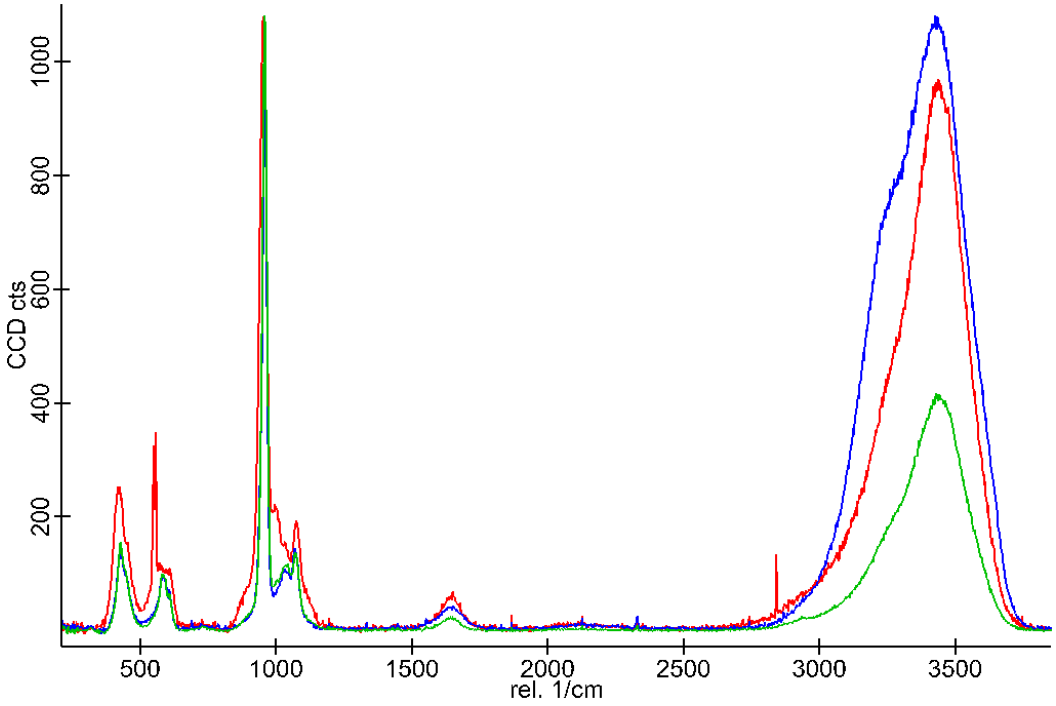

Buffered experiment, red – day 1, blue – day 2 and green – day 3

D.5 S_{cit} pH 8

D.4.1 Days 1 to 3 separated – 5.88 g citrate

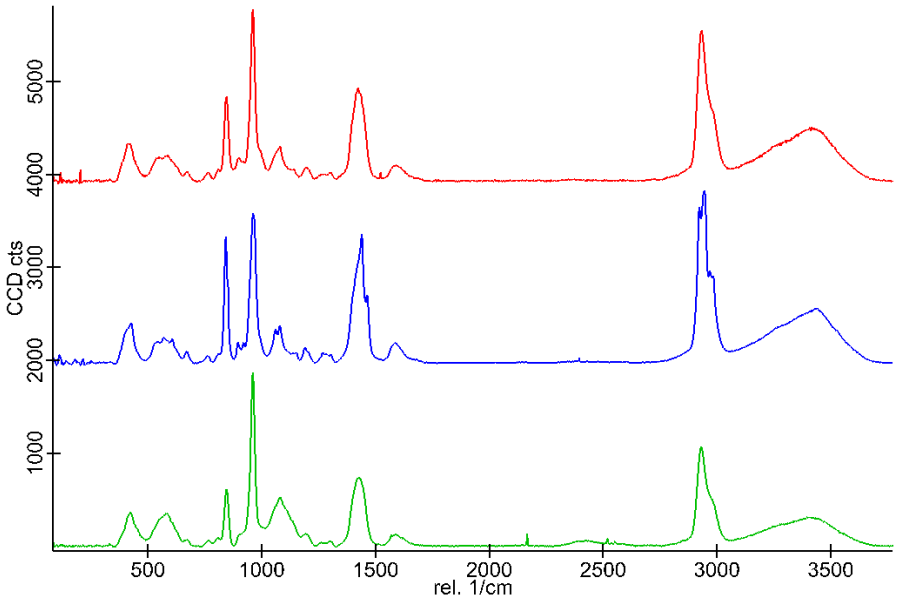

Buffered experiment, red – day 1, blue – day 2 and green – day 3

D.4.2 Days 1 to 3 overlay – 5.88 g citrate

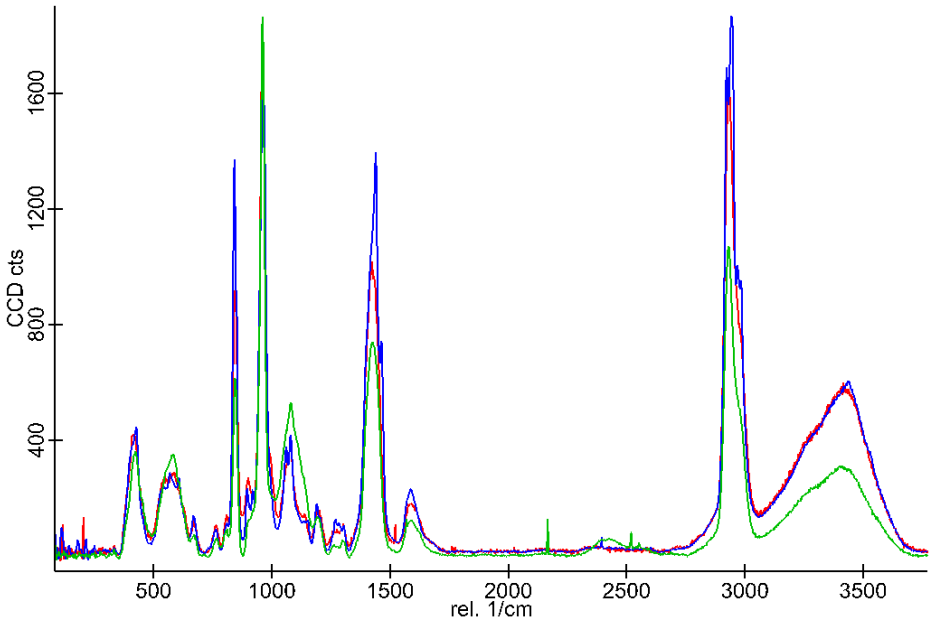

Buffered experiment, red – day 1, blue – day 2 and green – day 3

D.6 Scarb pH 7

D.5.1 Days 1 to 3 separated

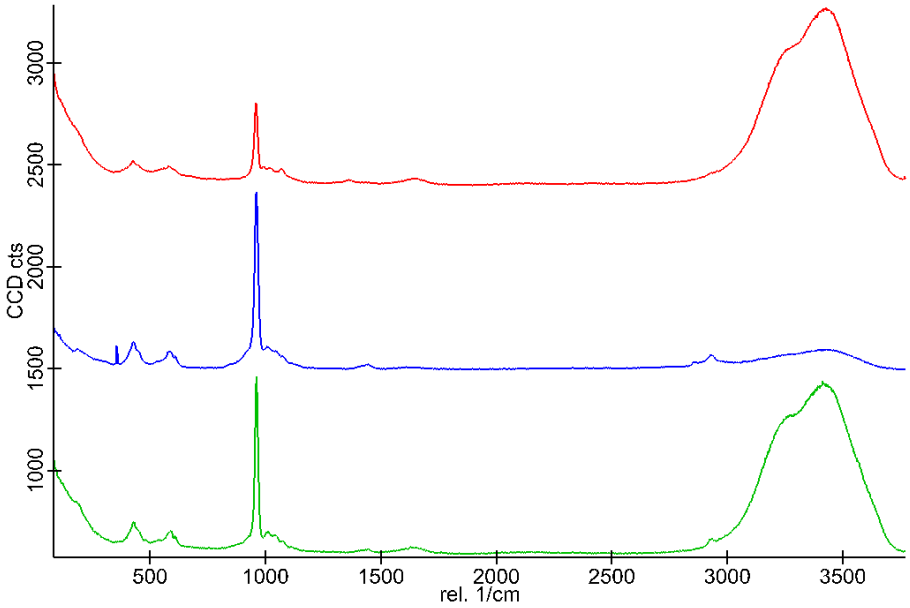

Buffered experiment, red – day 1, blue – day 2 and green – day 3

D.5.2 Days 1 to 3 overlay

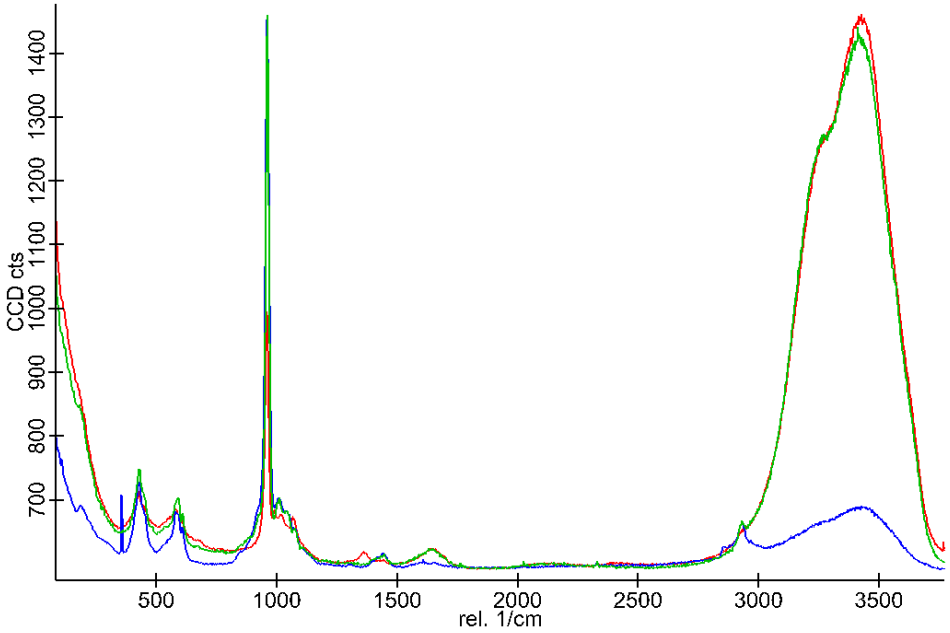

Buffered experiment, red – day 1, blue – day 2 and green – day 3

Appendix E: Raman band identification tables

Table 3: Peak types assigned to Raman peak positions (cm^{-1}) where PO_4^{3-} = Phosphate, CO_3^{2-} =carbonate and OH = hydroxide. Types based on finds from studies by (1) Litasov, 2017; (2) Li et al, 2016; (3) Falcke et al, 1990; (4) Frost et al, 2013; (5) Crane, 2016; (6) Penel et al., 1998

E.1 $S_{no\ add}$ pH 8

S no add– pH 8			
Day 1	**Day 2**	**Day 3**	**Peak type**
429	429	429	$V_2PO_4^{3-}$ bending (1,4,6)
447	453	-	$V_2PO_4^{3-}$ bending (1,4)
586	586	595	$V_4PO_4^{3-}$ bending (1,4,6)
613	613	-	$V_4PO_4^{3-}$ bending (1,4)
963	963	963	$V_1PO_4^{3-}$ strong symmetrical stretch (1,2,3,4)
1001	-	-	$V_3PO_4^{3-}$ asymmetrical stretch (1)
-	1043	1048	$V_3PO_4^{3-}$ asymmetrical stretch (1,4)
1069	1078	1075	$V_3PO_4^{3-}$ asymmetrical stretch (1,4); $v_3CO_3^{2-}$ symmetrical stretch (6)
1442	-	-	$V_3CO_3^{2-}$ (2)
1662	1653	1638	$V_3CO_3^{2-}$ CA + HA (2)
2855	-	-	
2923	-	-	
-	-	3255	OH stretching (4)
3445	3445	3412	

E.2 S_{carb} pH 7

Scarb – pH 7			
Day 1	**Day 2**	**Day 3**	**Peak type**
429	429	429	$V_2PO_4^{3-}$ bending (1,4)
450	453	453	$V_4PO_4^{3-}$ bending (1,4)
583	583	583	$V_4PO_4^{3-}$ bending (1,4)
-	613	613	$V_4PO_4^{3-}$ bending (1)
672	-	-	$V_4PO_4^{3-}$ bending (4)
960	963	963	$V_1PO_4^{3-}$ strong symmetrical stretch (1,2,3)
998	1012	1012	
1026	1051	1051	$V_3PO_4^{3-}$ asymmetrical stretch (1,4)
1072	1079	1079	$V_3PO_4^{3-}$ asymmetrical stretch (1,4) B-type $v_1CO_3^{2-}$ symmetrical stretch (1, 3)
1359	-	-	
-	1442	1442	$V_3CO_3^{2-}$ (2)
1647	-	1647	$V_3CO_3^{2-}$ CA + HA (2)
-	2864	-	
2935	2935	2935	
3261	-	3261	OH stretching (4)
3430	3439	3409	

E.3 S_{py}

E.3.1. pH 8

Spy – pH 8			
Day 1	**Day 2**	**Day 3**	**Peak type**
429	429	429	$V_2PO_4^{3-}$ bending (1,4)
577	583	583	$V_4PO_4^{3-}$ bending (1,4)
-	616	616	$V_4PO_4^{3-}$ bending (1)
-	729	-	
957	963	963	$V_1PO_4^{3-}$ strong symmetrical stretch (1,2,3,5); carbonated apatite (5)
998	-	-	$V_1PO_4^{3-}$ strong symmetrical stretch (1)
1040	1034	1034	$V_3PO_4^{3-}$ asymmetrical stretch (1,4)
1078	1075	1075	$V_3PO_4^{3-}$ asymmetrical stretch (1,3,4)
1638	1662	1662	$V_3CO_3^{2-}$ (2)
2923	2923	-	
-	3249	3295	OH stretching (4)
3439	3418	3403	

E.3.2. pH 9

Spy – pH 9			
Day 1	**Day 2**	**Day 3**	**Peak type**
426	426	426	$V_2PO_4^{3-}$ bending (1,4)
575	586	589	$V_4PO_4^{3-}$ bending (1,4)
-	613	613	$V_4PO_4^{3-}$ bending (1)
957	963	963	$V_1PO_4^{3-}$ strong symmetrical stretch (1,2,3,5): carbonated apatite (5)
1001	995	998	
1034	1040	1034	$V_3PO_4^{3-}$ asymmetrical stretch (1,4)
1081	1075	1075	$V_3PO_4^{3-}$ asymmetrical stretch (1,3,4)
1656	1638	1644	$V_3CO_3^{2-}$ (2)
-	3249	3255	OH^- stretching (4)
3374	3412	3421	OH^- stretching (4)

E.4 S_{cit}

E.4.1. pH 7 – 5.88 g

Scit– pH 7 – 5.88g citrate			
Day 1	**Day 2**	**Day 3**	**Peak type**
418	433	433	$V_2PO_4^{3-}$ bending (1,4)
454	454	454	$V_4PO_4^{3-}$ bending (1,4)
551	-	-	$V_4PO_4^{3-}$ bending (4)
559	585	585	$V_4PO_4^{3-}$ bending (4)
608	608	608	
956	962	962	$V_1PO_4^{3-}$ strong symmetrical stretch (1,2,3,5)
1000	-	-	
1035	1044	1044	$V_3PO_3^{3-}$ asymmetrical stretch (1,4)
1076	1068	1068	$V_3PO_3^{3-}$ asymmetrical stretch (1,3,4)
1646	1646	1646	$V_3CO_3^{2-}$ (2)
3247	3247	3247	OH^- stretching (4)
3434	3434	3434	OH^- stretching (4)

E.4.2. pH 7 – 0.01 g

Scit– pH 7 – 0.001g citrate			
Day 1	**Day 2**	**Day 3**	**Peak type**
450	450	450	$V_2PO_4^{3-}$ bending (1,4)
582	582	582	$V_4PO_4^{3-}$ bending (1,4)
611	611	611	
960	960	960	$V_1PO_4^{3-}$ strong symmetrical stretch (1,2,3,5)
1068	1068	1068	$V_3PO_3^{3-}$ asymmetrical stretch (1,3,4)
1649	1649	1649	$V_3CO_3^{2-}$ (2)
2933	2933	2933	
3448	3448	3448	OH^- stretching (4)

E.4.3. pH 8

Scit – pH 8			
Day 1	**Day 2**	**Day 3**	**Peak type**
418	429	432	$V_2PO_4^{3-}$ bending (1,4)
554	542	539	$V_4PO_4^{3-}$ bending (1,4)
583	572	586	$V_4PO_4^{3-}$ bending (1,4)
-	610	613	$V_4PO_4^{3-}$ bending (1)
672	672	672	$V_4PO_4^{3-}$ bending (4)
-	734	-	
767	767	761	
806	805	809	Calcium citrate (2)
850	843	850	
903	903	903	
-	921	-	
960	968	963	$V_1PO_4^{3-}$ strong symmetrical stretch (1,2,3)
998	-	-	$V_1PO_4^{3-}$ strong symmetrical stretch (1)
-	1065	1046	$V_3PO_4^{3-}$ asymmetrical stretch (1)
1086	1079	1086	$V_3PO_4^{3-}$ asymmetrical stretch (1)
1140	1155	1140	$V_3PO_4^{3-}$ asymmetrical stretch (1); citrate (2)
-	1191	1200	Citrate (2)
1265	1271	1259	Citrate (2)
1306	1306	1303	Citrate (2)
1434	1441	1440	Citrate (2)
-	1463	-	
1583	1585	1585	
-	-	2858	
2936	2926	2936	
-	2947	-	
-	2968	-	
2989	2989	2989	
3434	3439	3436	

Appendix E Five-day peak fitting for Scarb

F.1 Day 1

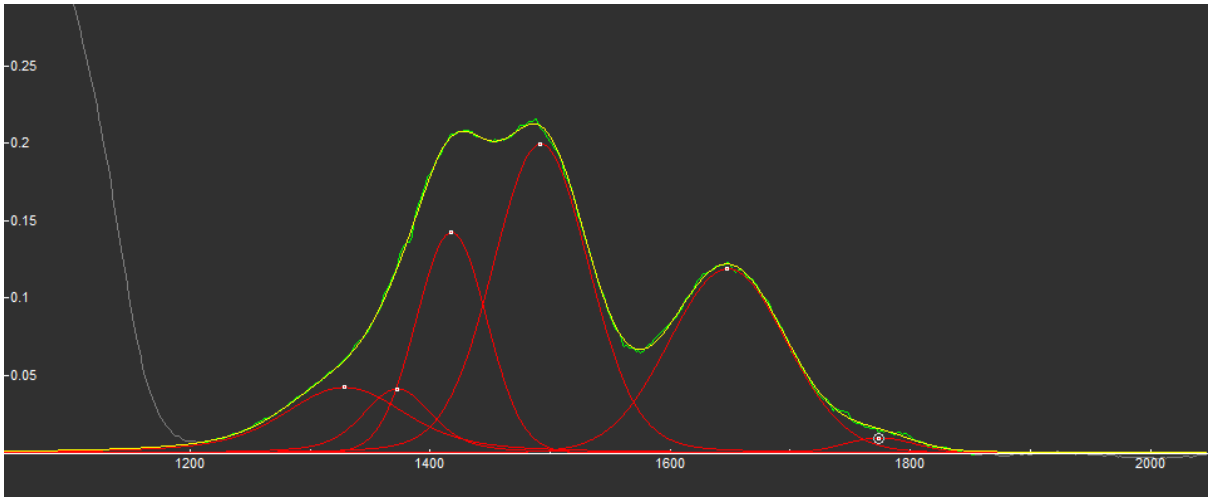

F.2 Day 2

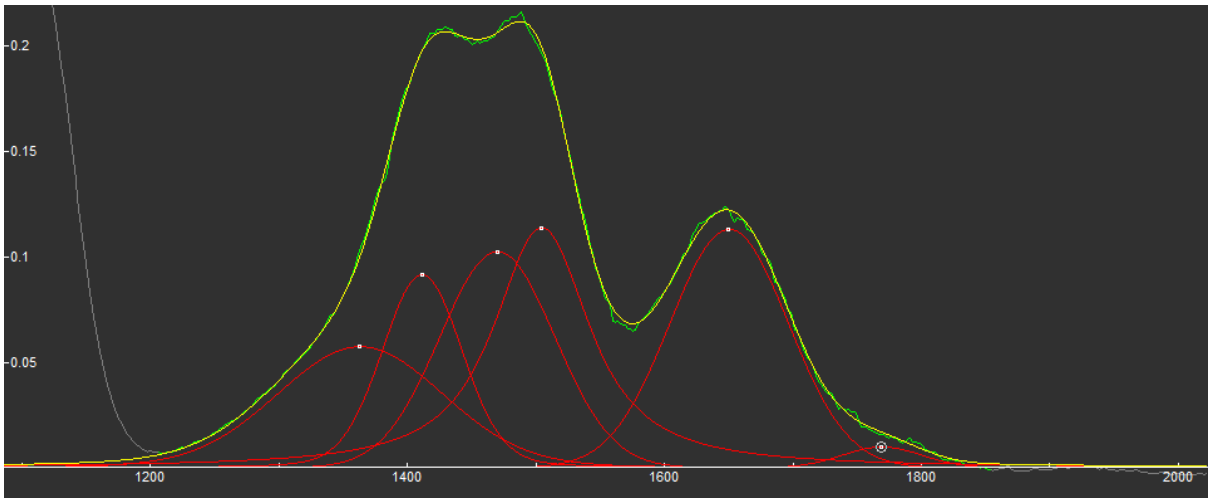

F.3 Day 3

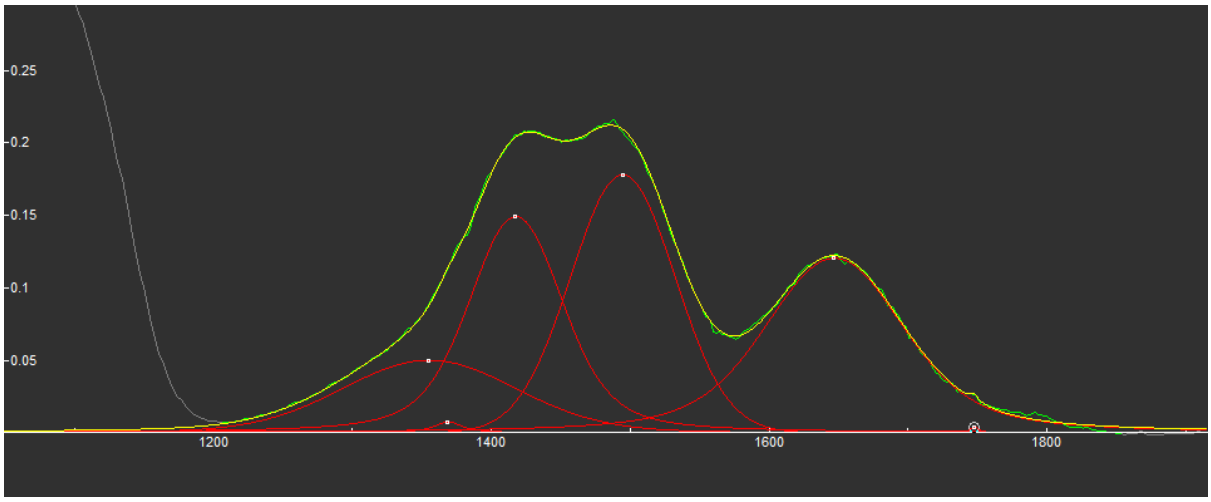

F.4 Day 4

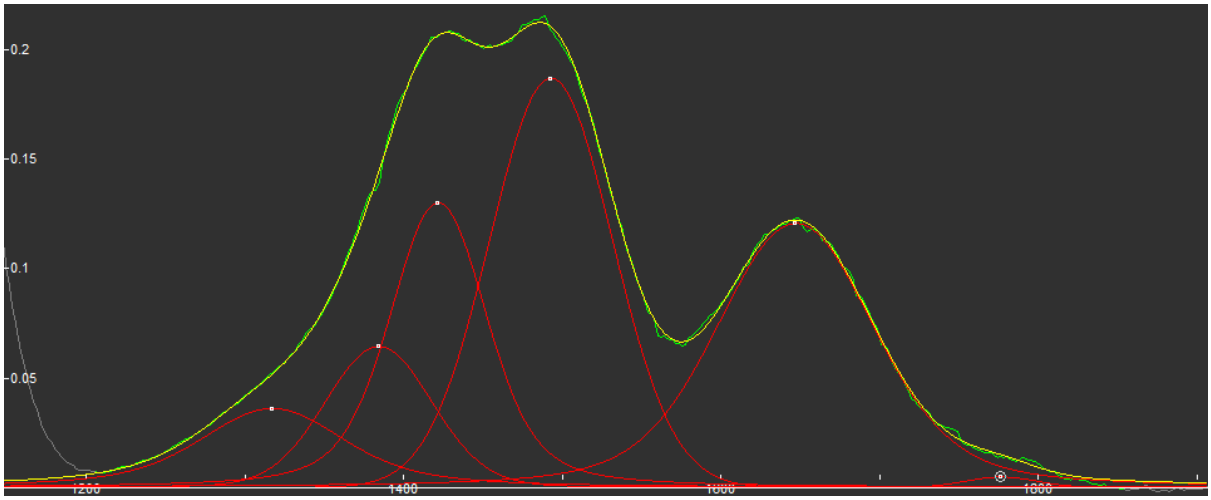

F.5 Day 5

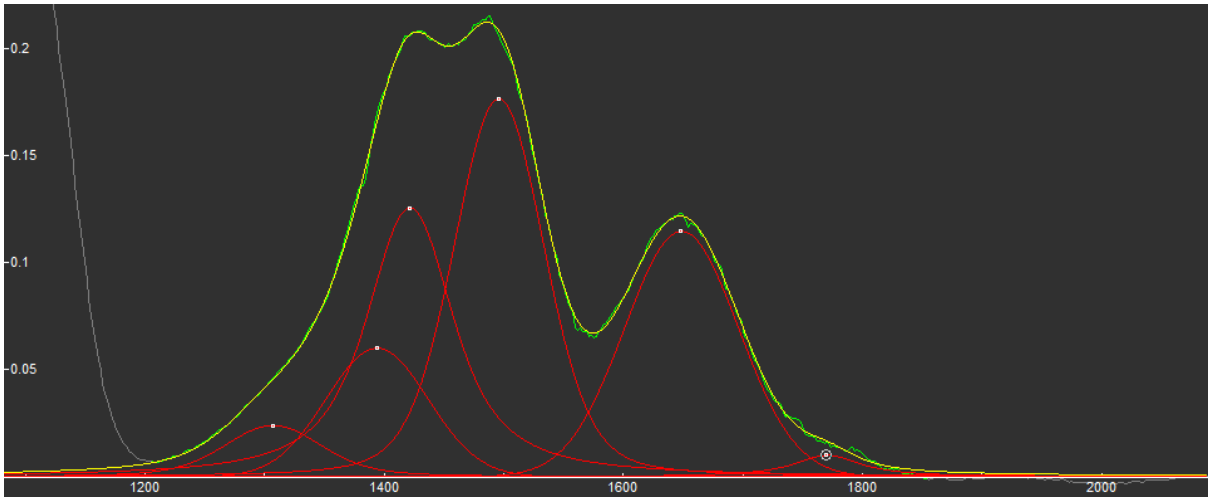

Appendix G: Crystallinity Index graphs

G.1 $S_{no\ add}$

G.1.1 Crystallinity of $v_1PO_4^{3-}$

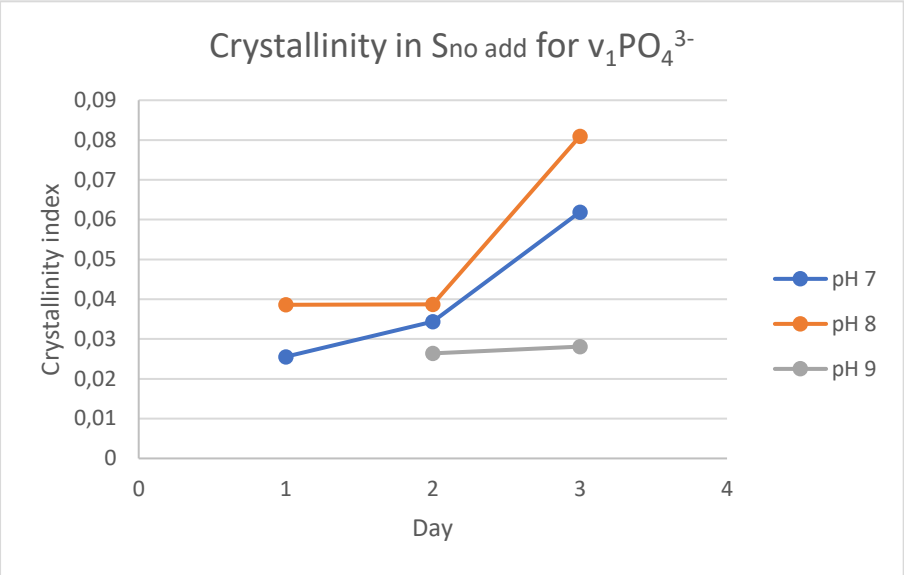

G.1.2 Crystallinity of $v_3PO_4^{3-}$

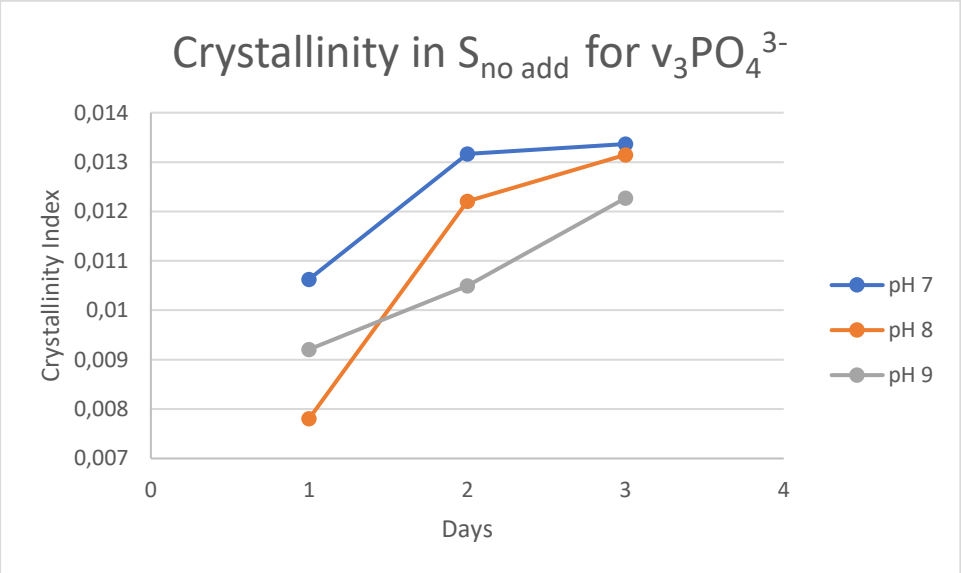

G.1 S_{py}

G.1.1 Crystallinity of $v_1PO_4^{3-}$

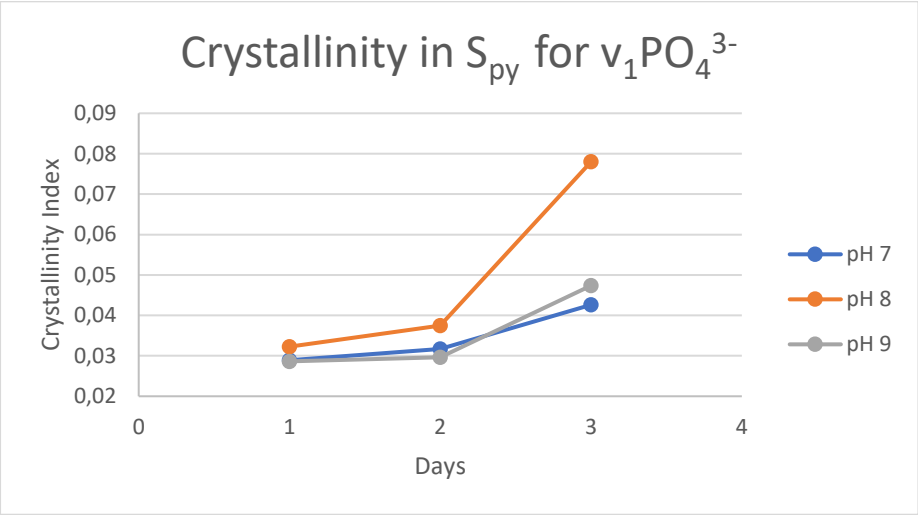

G.1.2 Crystallinity of $v_3PO_4^{3-}$

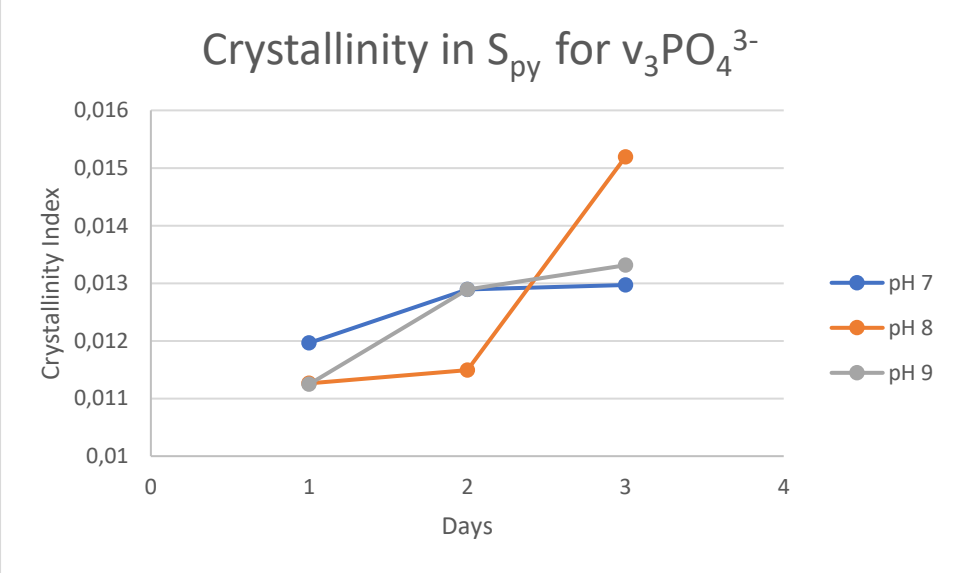

G.1 S_{carb}

G.1.1 Crystallinity of $v_1PO_4^{3-}$

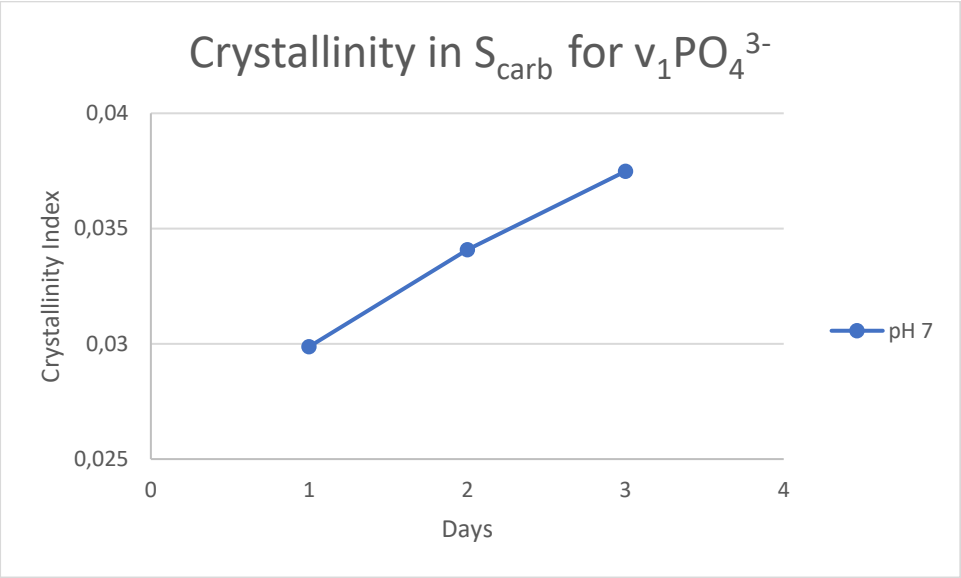

G.1.2 Crystallinity of $v_3PO_4^{3-}$

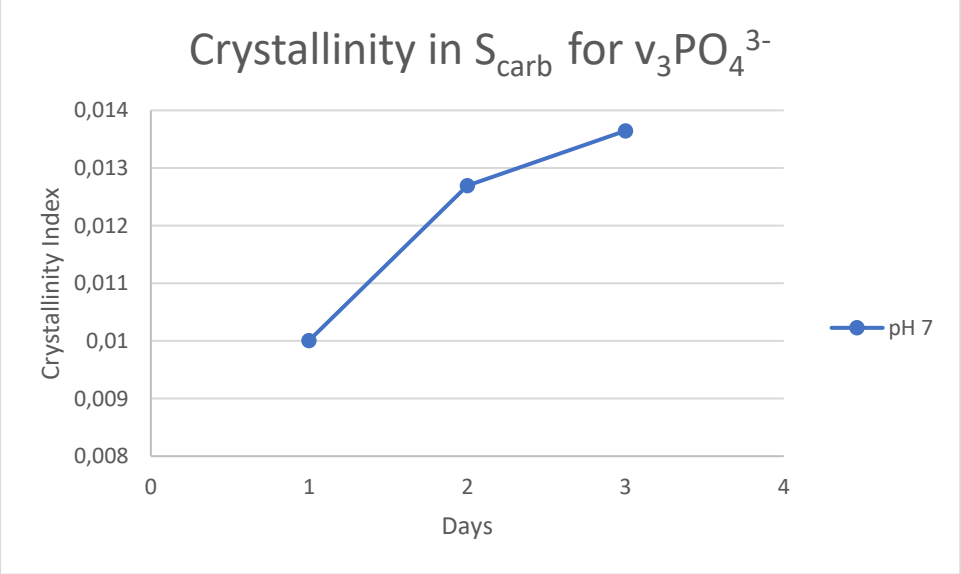

G.1 S_{cit} – 0.001g citrate

G.1.1 Crystallinity of $v_1PO_4^{3-}$

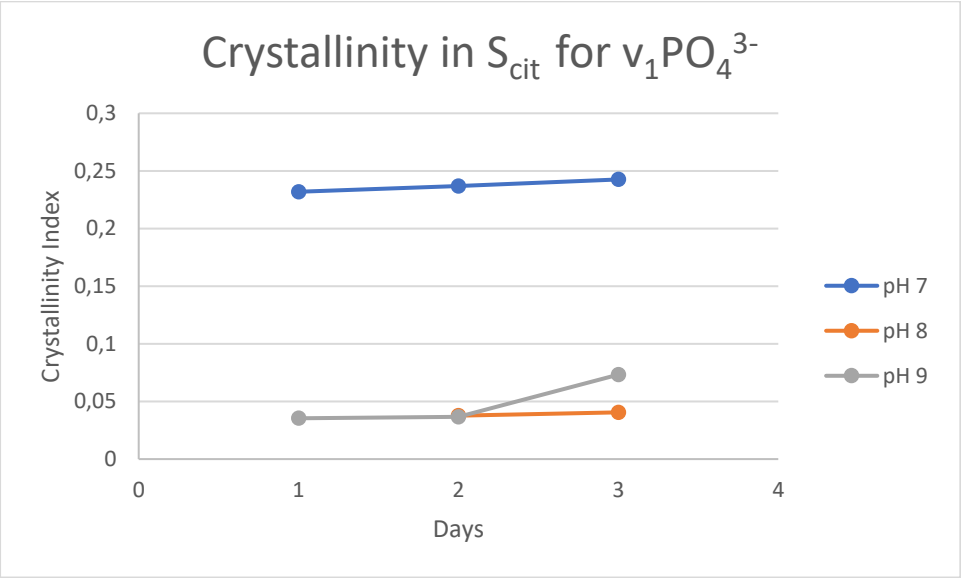

G.1.2 Crystallinity of $v_3PO_4^{3-}$

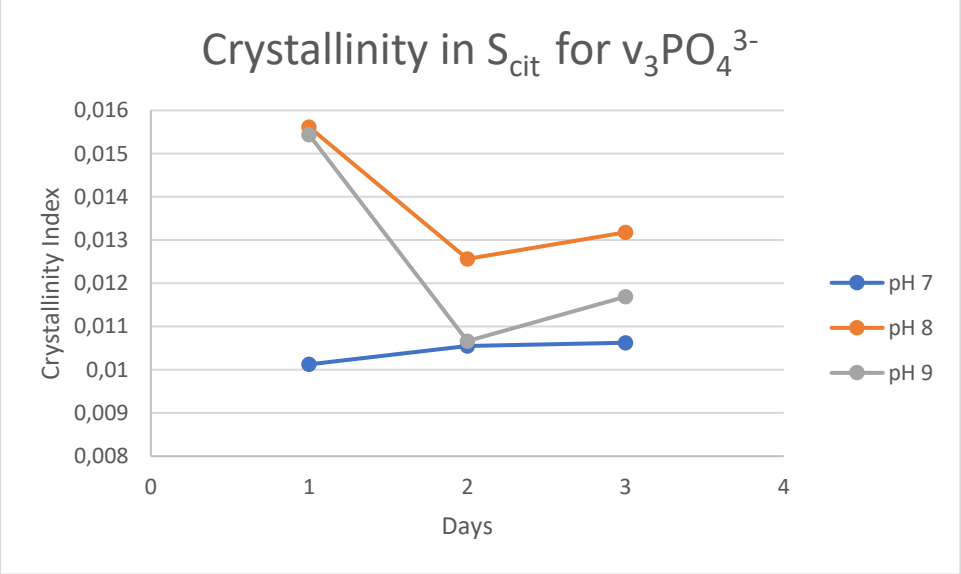

Appendix H: Error Margin

One spectrum from the S_{carb} experiments was fit once every day for five days to estimate the human errors associated with manual band fitting. The spectral region between 1200 and 1800 cm^{-1} was chosen for this purpose. Bands were fitted assuming that their shape was similar to a Voigt function, the most commonly chosen function for vibrational band fitting. Each day, the six bands in this spectral region were fitted and grouped into two band envelopes: A (bands 1 to 4), and B (bands 5 and 6). The fitting regime highlighted that this procedure is associated with an error as the calculated band centers after minimization in the band fitting software Fityk, showed a minor shift in wavelength across the different days.

Similarly, the fitted peak areas differed slightly on each day (Appendix E). Therefore, a standard deviation of the center and area parameter was calculated using the five different fits. This error was then used in error propagations when calculating the areas of band envelopes. Area per peak per day fitted is shown in Table 7 below, along with the mean area of each peak over the five days.

Table 7: Areas for peak A and B for five days and the mean area calculated over the five days per peak

Days	Peak area A	Peak area B
1	41.8408	15.5541
2	43.9255	13.8137
3	40.0423	17.9532
4	40.4897	17.4620
5	43.3403	14.7660
Mean area	41.9277	15.9098
Sum of all values	209.6386	79.5491

N = number of values
Σx = sum of all values
μ = mean
σ = standard deviation
σ^2 = variance

Use of: $\sigma = \sqrt{\frac{1}{N}\sum_{i=1}^{N}(x_i - \mu)^2}$
So: $\sigma^2 = \frac{\sum(x_i-\mu)^2}{N}$

Peak A
N = 5
Σx = 209.6386
μ = 41.9277

$\sigma^2 = \frac{(41.8408-41.92772)^2+..+(43.3403-41.92772)^2}{5} = \frac{11.616772368}{5}$ = 43.239976455

$= \sqrt{43.239976455}$ = 2.3233544736

σ^2 = 2.32
$\sigma = \pm$ **1. 52 cm^{-1}**

For peak B the σ is $\pm$ **1. 58 cm^{-1}**

The lower the standard deviation is, the more the values are closer to the mean value; therefore, the results are more reliable, while with increasing standard deviation, the values spread out more. As seen for the standard deviation for peaks A and B, the values are very similar and small. Therefore, shifts in spectra banding of 10 cm^{-1} is a significant shift as the standard deviation is small, and would not be related to the error. The error propagation shows us what the error is when using the information from the fitting as those measurements have their own error, and is calculated below:

Error propagation = $\frac{\sigma_A}{\sigma_B} = \sqrt{\left(\frac{\delta\sigma_A}{A}\right)^2 + \left(\frac{\delta\sigma_B}{B}\right)^2} = \sqrt{\left(\frac{1.52}{41.9277}\right)^2 + \left(\frac{1.58}{15.9098}\right)^2}$ = 0.106 cm^{-1}

Appendix I: Molarity of the experiments

The tables below (Table I.1 and I.2), show data for the initial solution molarity (M) (S_0) and the added 0.1 M NaOH and/ or 0.1 M HCl (mL) to the solution over three days as the experiment was run and the chemical reaction took place. The chemical reaction was set up by pumping 50 mL of the 0.12 M (with additive) phosphate solution into 50 mL of 0.1 M calcium chloride solution. Every day, a sample of 10 mL was taken.

Table I.1: S_0 = Initial solution molarity (M/L) and the amount of acid or base added to the solution over three days per test for all pH levels

Experiments run										
Sample	**Scarb**	**S no add**			**Spy**			**Scit**		
pH	7	7	8	9	7	8	9	7	8	9
S_o moles (M)	0,24	0,5			0,001			0,4		
0.1M NaOH (ml)	18	65,4627	37,853	41,109	35,5205	31,698	32,614	30,166	28,691	57,6825
0.1M HCl (ml)	91,6715									

Table I.2: A second run for some samples where S_0 = Initial solution molarity (M/L) and the amount of acid or base added to the solution over three days per test for all pH levels

Sample	**Scarb**	**S no add**	**Spy**		
Ph	7	8	7	8	9
S_o moles (M)	0,24	0,5	0,001		
0.1M NaOH (ml)	15	65,4627			
0.1M HCl (ml)	101,8112	55,6411	50,0201	51,328	37,355

To calculate the molarity of the solution each day, several calculations were done. For example: calculating the molarity for S no add pH 7:

Table I.3: Steps used to calculate the molarity of the solution for all three days. The S no add pH 7 sample is used as an example

	S no add 7
Amount of 0.1M NaOH added per day (ml/day)	65.4627/ 3 = *21.8209*
Initial volume (ml)	50 + 50 = *100*
Initial molarity (M)	0.5
Moles in initial volume	(100/1000) *0.5 = ***0.05***
Day 1 volume	100 + 21.8209 = *121.8209*
Day 1 volume post sample 1	121.8209 – 10 = *111.8209*
Percentage that has above moles	100/ 121.8209 = *0.8208772*
Number of moles in Day 1 volume of 121 mL	0.05*0.8208772 = ***0.0410439***
	0.0410439/121.8209 = *0.0003369*
Number of moles taken out during sample 1	0.0003369 * 10 = *0.0033692*
Number of moles in Day 2 volume of 111 mL (Post sample 1)	0.0410439 – 0.0033692 = *0.0376747*
Day 2 volume	111.8209 + 21.8209 = *133.6418*
Day 2 volume post sample 1	133.6418 – 10 = *123.6418*
Percentage that has above moles	111.8209/ 133.6418 = *0.836721*
Number of moles in Day 2 of 133 mL	0.836721*0.0376747 = ***0.0315232***
	0.0315232/ 133.6418 = *0.0002359*
Number of moles taken out during sample 2	0.0002359*10 = *0.0023588*
Number of moles In Day 2 volume of 123 mL (post sample 2)	0.0315231 – 0.0023588 = *0.0291644*
Day 3 volume	123.6418 + 21.8209 = *145.4627*
Day 3 volume post sample 3	145.4627 – 10 = *135.4627*
Percentage that has above moles	123.6418/ 145.4627 = *0.8499897*
Number of moles In Day 3 volume of 145 mL	0.8499897* 0.021644 = ***0.0247894***
	0.0247894/ 145.4627 = *0.0001704*
Number of moles taken out during sample 3	0.0001704*10 = *0.0017042*
Number of moles in Day 3 volume of 135 mL (Post sample3)	0.0247894 – 0.0017042 = *0.0230853*

Note: for the S_{carb} sample, the initial volume includes the 0.1 M NaOH added manually at the beginning of the chemical reaction. For example, S_{carb} sample run 1: the initial volume is 50 + 50 + 18 = 118 mL instead of 100 mL.

Table I.4 below shows the molarities of the solution before and after the sample was taken. As seen in the table, all experiments show a decrease in their molarity with every sample taken.

Table I.4 All molarities of the solutions tested, before and after the sample was taken

Sample	Scarb		S no add				Spy				Scit		
pH	7		7	8		9	7	8		9	7	8	9
Run	1	2	1	1	2	1	1	1	2	1	1	1	1
Initial molarity	0.00283	0.00276	0.05	0.05	0.05	0.05	0.0001	0.0001	0.0001	0.0001	0.04	0.04	0.04
Day 1	0.00225	0.002131	0.0410	0.0487	0.0461	0.0482	9.819E-05	9.943E-05	9.336E-05	9.913E-05	0.0399	0.0395	0.0366
Day 1 post sample	0.00210	0.00199	0.0377	0.0444	0.0422	0.0440	8.941E-05	9.044E-05	8.539E-05	9.019E-05	0.0363	0.0359	0.0335
Day 2	0.00172	0.00160	0.0315	0.0395	0.0360	0.0388	8.010E-05	8.184E-05	7.362E-05	8.141E-05	0.0330	0.0323	0.0285
Day 2 post sample	0.00162	0.00151	0.0296	0.0361	0.0332	0.0355	7.305E-05	7.448E-05	6.770E-05	7.413E-05	0.0300	0.0294	0.0263
Day 3	0.00136	0.001245	0.0248	0.0322	0.0287	0.0315	6.556E-05	6.743E-05	5.888E-05	6.697E-05	0.0272	0.0265	0.0226
Day 3 post sample	0.00129	0.001182	0.0231	0.0295	0.0265	0.0289	5.989E-05	6.139E-05	5.439E-05	6.102E-05	0.0248	0.0242	0.0209